

University of Louisville

## ThinkIR: The University of Louisville's Institutional Repository

---

Electronic Theses and Dissertations

---

12-2012

### Incorporating nanomaterials with MEMS devices.

Evgeniya V. Moiseeva 1980-  
*University of Louisville*

Follow this and additional works at: <https://ir.library.louisville.edu/etd>

---

#### Recommended Citation

Moiseeva, Evgeniya V. 1980-, "Incorporating nanomaterials with MEMS devices." (2012). *Electronic Theses and Dissertations*. Paper 998.

<https://doi.org/10.18297/etd/998>

This Doctoral Dissertation is brought to you for free and open access by ThinkIR: The University of Louisville's Institutional Repository. It has been accepted for inclusion in Electronic Theses and Dissertations by an authorized administrator of ThinkIR: The University of Louisville's Institutional Repository. This title appears here courtesy of the author, who has retained all other copyrights. For more information, please contact [thinkir@louisville.edu](mailto:thinkir@louisville.edu).

# **INCORPORATING NANOMATERIALS WITH MEMS DEVICES**

By

Evgeniya V. Moiseeva

B.S., Physics, Perm State University, 2001

M.S., Physics, Perm State University, 2003

M.S., Physics, University of Louisville, Louisville, 2006

A Dissertation

Submitted to the Faculty of the  
Speed School of Engineering of the University of Louisville  
in Partial Fulfillment of the Requirements  
for the Degree of

Doctor of Philosophy

Electrical and Computer Engineering Department  
University of Louisville  
Louisville, Kentucky

December 2012

Copyright 2012 by Evgeniya V. Moiseeva

All rights reserved

# INCORPORATING NANOMATERIALS WITH MEMS DEVICES

By

Evgeniya V. Moiseeva

B.S., Physics, Perm State University, 2001

M.S., Physics, Perm State University, 2003

M.S., Physics, University of Louisville, Louisville, 2006

A Dissertation Approved on

November 26, 2012

by the following Dissertation Committee:

---

Cindy Harnett, PhD,  
Dissertation Director

---

Shamus McNamara, PhD

---

John Naber, PhD

---

Palaniappan Sethu, PhD

---

## **DEDICATION**

To my Mom and Dad

## ACKNOWLEDGEMENTS

I would like to thank my professor, Dr. Cindy Harnett, for her guidance, endless support and patience. I am grateful to her for being a continuous source of motivation and inspiration. I would also like to thank my lab members: Yehya Senousy, Tom Lucas, Silpa Kona, and Jasmin Beharic who put their efforts in making the lab very exciting place to work.

I am very grateful to Professor J. Naber, Professor S. McNamara and Professor P. Sethu for being on my committee and giving me feedback on the project and manuscript. I would like to express my thanks to Dr. A. M Gobin and Dr. G. Zhang for their help and guidance with nanoparticle synthesis and polymers preparation. I would also like to thank the Cleanroom staff of the University of Louisville for their invaluable help and great teaching experience and for providing me with equipment.

But above all, I am grateful to my family and friends, who provided unconditional love and support throughout my studies.

## **ABSTRACT**

### **INCORPORATING NANOMATERIALS WITH MEMS DEVICES**

Evgeniya Moiseeva

November 26, 2012

This dissertation demonstrates an elegant method, known as ‘micro-origami’ or strain architecture to design and fabricate three-dimensional MEMS structures which are assembled using actuation of a metal-oxide bilayer with conventional planar lithography. Folding allows creating complex, robust, three-dimensional shapes from two-dimensional material simply by choosing folds in the right order and orientation, small disturbances of the initial shape may also be used to produce different final shapes. These are referred to as “pop-up structures” in this work.

The scope of this work presented the deposition of colloidal gold nanoparticles (GNPs) into conformal thin films using a microstenciling technique. Results illustrated that the gold nanoparticle deposition process can easily be integrated into current MEMS microfabrication processes. Thin films of GNPs deposited onto the surfaces of silicon-based bistable MEMS and test devices were shown to have a significant effect on the heating up of microstructures that cause them to fold.

The dissertation consists of four chapters, covering details of fabrication methods, theoretical simulations, experimental work, and existing and potential applications. Chapter II illustrates how control of the folding order can generate complex three-

dimensional objects from metal-oxide bilayers using this approach. By relying on the fact that narrower structures are released from the substrate first, it is possible to create multi-axis loops and interlinked objects with several sequential release steps, using a single photomask. The structures remain planar until released by dry silicon etching, making it possible to integrate them with other MEMS and microelectronic devices early in the process.

Chapter III depicts the fabrication process of different types of bistable structures. It describes the principle of functioning of such structures, and simulations using CoventorWare are used to support the concept. We talk over about advantages and disadvantages of bistable structures, and discuss possible applications.

Chapter IV describes fabrication procedure of nanoparticle-MEMS hybrid device. We introduce a convenient synthesis of GNPs with precisely controlled optical absorption in the NIR region by a single step reaction of  $\text{HAuCl}_4$  and  $\text{Na}_2\text{S}_2\text{O}_3$ . We take a look at different techniques to pattern gold nanoparticles on the surface of MEMS structures, and also provide a study of their thermal properties under near IR stimulation. We demonstrate the first approach of laser-driven bistable MEMS actuators for bioapplications.

Finally, in Conclusion discuss the contributions of this dissertation, existent limitations and plans of the future work.



## TABLE OF CONTENTS

	PAGE
DEDICATION	iii
ACKNOWLEDGEMENTS	iv
ABSTRACT	v
LIST OF TABLES	x
LIST OF FIGURES	xi
CHAPTER	
I. INTRODUCTION	1
1.1 Self-assembly	4
1.2 Bilayer structure	4
1.3 Microactuators and different types of actuation	5
1.4 Nanostructures: nanoparticles and nanotubes	7
1.5 Nanoparticle-MEMS hybrid device	8
II. ORIGAMI FABRICATION OF MICROSTRUCTURED 3D DEVICES BASED ON STRESS-MISMATCHED LAYERS	10
2.1 Theory of thermal bending	14
2.2 Fabrication process	19
2.2.1 Cr/Ni/Cr structure	19
2.2.2 Ti/TiNi structure	20

2.2.3 Ti/Pt structure	20
2.3 Discussion of material properties and predicted curvature	23
2.4 Simple structures with two characteristic release times	27
2.5 Structures with randomly determined release times	29
2.6 Structures with engineered incremental release times	31
2.7 Structure with carefully controlled release sequence	34
2.8 Released structures as thermal actuators	35
2.9 Possible application and conclusions	36
III. BISTABLE MEMS STRUCTURE	39
3.1 Definition of bistability and bistable mechanism	39
3.2 Finite element analysis using CoventorWare	42
3.3 Symmetrical bistable structure	44
3.4 Asymmetrical bistable structure	48
3.5 Serpentine asymmetrical structure	50
3.6 Conclusion	54
IV. LIGHT-POWERED HYBRID MICROACTUATORS FOR BIOENGINEERING APPLICATIONS	56
4.1 Light driven microsystems/microdevices	56
4.2 Nanomaterials preparation methods	59
4.3 Deposition of nanostructures by chemical vapor deposition	61
4.4 Deposition of nanostructures by Dimatix inkjet printer	66
4.5 Deposition of nanostructures by microstenciling technique	69
4.6 Gold nanoparticles	76

4.6.1 Properties of nanoparticles	76
4.6.2 Synthesis of nanoparticles	78
4.7 Thermal efficiency of gold nanoparticles	81
4.7.1 Thermal efficiency measurement setup	82
4.7.2 Thermal efficiency analysis	89
4.7.3 Discussion and possible application	92
4.8 Hybrid nanoparticle-MEMS actuator	94
4.8.1 Fabrication and principle of operation	96
V. CONCLUSION	101
REFERENCES	103
APPENDIX	124
CURRICULUM VITAE	130

## LIST OF TABLES

TABLE	PAGE
1. Actuators: their actuation principle and characteristics	5
2. Material properties, layer thickness, stress and calculated curvature radius for Cr/Ni/Cr/SiO <sub>2</sub> and Ti–NiTi/SiO <sub>2</sub> bimorph structures	26
3. Summary of the polymer solutions and their properties	75
4. Calculated thermal factors for the bare and coated devices	91
5. Conditions of the polymer solution prepared and tested for the study	129

## LIST OF FIGURES

FIGURE	PAGE
1. Examples of micro- and nanostructures created with origami technique	13
2. Schematic of a metal–insulator bimorph bending because of strain mismatch induced curvature upon release from the substrate	16
3. Fabrication process flow	22
4. Stress results summary window and stress measurement results. The white trace indicates compressive stresses are present in SiO <sub>2</sub> film	24
5. Stress results summary window and stress measurement results. The white trace indicates compressive stresses are present in SMA film	25
6. Stress results summary window and stress measurement results. The white trace indicates compressive stresses are present in SiO <sub>2</sub> film	25
7. Layout and SEM image of released toroid structure, (b), and (c) Layouts and SEM images for tilted radial structure with arms off-axis from the center	28
8. Layout for symmetric zigzag structure while long bars are 7 μm wide, SEM image shows arrangement of bimorphs during the release process, (c) SEM image of a side view of released zigzag structure	30
9. Layout of untangled V-structure. Line widths range from 10 μm to 5 μm in 1 μm increments, with 5 μm spacing. (b) Partially released untangled V - structure, showing independent 5, 6 and 7 μm wide	

structures. Oxide thickness is 475 nm, Ti – TiNi thicknesses are 50 and 220 nm respectively. (c) Layout for tangled-V structure, with linewidth order reversed from untangled-V structure. (d) Partially released tangled V-structure, showing 5, 6 and 7 $\mu\text{m}$ structures wrapped around each other due to release sequence	32
10. Side view of a fully released tangled-V structure with 15 $\mu\text{m}$ spacing between lines. Oxide thickness is 400 nm and Cr/Ni/Cr thicknesses are 50–60–50 nm	33
11. Three-step fabrication sequence for a three-axis loop structure from a single photomask. Loop 1 forms and is lifted up by formation of loop 2, after which loop 3 wraps around the previously formed loops. (b) The finished structure showing coils in x–y, x–z and y–z planes	34
12. Layout of microcage, (b)-(e) SEM of 250 micron diameter microgrippers as temperature increases from 30°C to approximately 200°C. Differential thermal expansion unfolds the actuators	35
13. Strain energy and (b) force-displacement diagram for bistable system. Any local minima represent stable positions	40
14. Meshed model of bilayer structure	43
15. Layout of symmetrical bistable structure	44
16. CoventorWare simulation of “windowpane” shape symmetrical bistable structure	45
17. CoventorWare simulation of “windowpane” shape symmetrical bistable structure	46

18. Calculated average Mises stress in the entire volume	47
19. SEM image of fabricated structures, according to process discussed in Chapter II (Figure 3), released in both possible bistable states	48
20. Layout of asymmetrical bistable structure	48
21. CoventorWare simulation of asymmetrical bistable structure	49
22. SEM image of three different designs of released asymmetrical bistable structures	50
23. Layout of bistable device showing two U-shaped cantilevers with their contact pads and joined by a cross-bar at the tips	51
24. CoventorWare simulation of asymmetrical bistable structures (a) rear actuator at 280K, front actuator at 300K, (b) side view, (c) both actuators at 300K, (d) side view, (e) rear actuator at 340K, front actuator at 300K, (f) side view	52
25. Electron micrographs of a wide field of Cr/Ni/Cr asymmetric released devices having different initial orientations	53
26. Diagram represents mechanisms of light energy conversion, actuation methods and applications for light-driven microstructures	58
27. Schematic diagram of CVD reactor	62
28. CVD-grown single-walled carbon nanotubes on Cr/Ni/Cr bistable structure	63
29. CVD-grown single-walled carbon nanotubes on Ti/Pt bistable structure	64
30. Raman spectra of synthesized SCNTs	64
31. Optical image of ink jet-deposited nanoparticle (solution A) in a dot	

array pattern on the glass slide	68
32. Optical image of printed array patterns using (a) solution B, (b) solution C on the glass slide	68
33. Scanning electron microscopy of microstencils	72
34. Optical images of (a) individual microstencil, (b) 25 $\mu\text{m}$ wide microstencil stripes, (c) array of microstencils, (d) set of microstencils from 5 to 300 $\mu\text{m}$	73
35. Small (b) and large (a), (c) and (d) scale features generated applying microstencil technique for different aqueous biocompatible solution.	74
36. Diagram represents the key properties of gold nanoparticles [158]	76
37. UV–vis-NIR spectra of the nine GNPs samples measured after mixing $\text{Na}_2\text{S}_2\text{O}_3$ with $\text{HAuCl}_4$ solution [162]	79
38. STEM and HRTEM images of gold nanoparticle of different shapes and properties [162]	80
39. Schematic of the thin-film resistor used to characterize the absorbance of deposited gold nanoparticles	82
40. Optical absorption spectrum of synthesized gold nanoparticles, (b) TEM image of synthesized nanoparticles	84
41. Optical image of fabricated resistive temperature sensor, (b) and SEM images of gold NPs in PVP polymer matrix, (c) and (e) gold NPs in chitosan matrix after spin-coating on the platinum test surface	85
42. Thermal efficiency measurement setup: a LabVIEW console operates the 808 nm laser, and resistance-induced temperature changes are calculated from voltages measured by an amplifier circuit	86



43. Distribution of maximum temperatures for bare and nanoparticle coated samples	88
44. The box plot of the data demonstrates the difference in optical absorption when nanoparticles are applied to the surface	89
45. Diagram of light-powered actuator as potential tool for bioresearch	95
46. Fabrication process flow for hybrid actuator: (a) Silicon wafer with 400–500 nm thermal oxide, (b) - (e) A 200–300 nm thick metal pattern is applied using photoresist liftoff, (f) The metal acts as an etch mask to pattern the oxide in a CF <sub>4</sub> /H <sub>2</sub> plasma etch, (g) Vapor deposition of Parylene C conformal film, (h) Patterning of polymer film using soft lithography and plasma etching, (i) Deposition on nanoparticle, (j) The metal-oxide bimorph is released by etching the silicon in XeF <sub>2</sub> gas	97
47. SEM images of fabricated light-powered hybrid with patterned gold nanoparticles	99
48. An optical image of light-powered actuator when (a) laser is ON, (b) laser is OFF (c) side view of hybrid actuator	100

## **CHAPTER I**

### **INTRODUCTION**

This dissertation describes a “hybrid” microactuator design that combines light-absorbing nanomaterials with a thermally-driven microelectromechanical (MEMS) actuator. The core topic investigated in this study is the integration and alignment of photothermal nanomaterials with a MEMS device in a manner that does not interfere with MEMS fabrication or the thermal functionality of the nanomaterials. Chapter I reviews MEMS actuators and relevant nanomaterials. Chapter II reviews the origami fabrication technique in detail, and Chapter III investigates bistability as a way to achieve sudden actuation from a gradual thermal process. Chapter IV evaluates the thermal performance of the nanomaterials on MEMS substrates.

A wide variety of MEMS devices have found commercial success. These devices include electrical and optical switches, pumps, valves, motors, scanning mirrors, displays, gyroscopes, accelerometers, and pressure sensors [1]. MEMS technology has enabled a reduction of size and power by orders of magnitude, while increasing the consistent performance of devices and systems by employing batch fabrication techniques. Meanwhile, integration of MEMS technologies with the semiconductor industry allows the development of new micromachining processes for MEMS side-by-side with electronic circuits, at the cost of longer development time, higher price, and greater complexity. The clear advantage of integrating MEMS components is their ability to

provide a transduction mechanism from analog physical signals into digital electrical signals and vice versa. Common transduction mechanisms used by MEMS sensors and actuators are presented in [1].

Some physical phenomena (inertia, magnetostatics) decrease in strength at the microscale relative to other forces that dominate or are more efficient when miniaturized to the micro- and nanometer scale. That is why it is essential to be mindful of scaling when creating microfabricated devices. The effect of scaling on material properties is important, for example, in thin-film materials where properties are often considerably altered from their bulk or macro scale form. Important material properties to characterize include elastic modulus, Poisson's ratio, compressive, tensional and shear stresses, conductivity, etc. Due to the flexibility of microfabrication, it is typically convenient to integrate microstructures that can be used to provide in situ measurements of material properties.

However, thin films are often not the ideal form factor for sensing and actuation. Origami-like techniques have been commonly used to build complex three-dimensional (3D) micro- and nanoscale structures, devices and advanced materials, both for artistic and technological purposes, from patterned thin films. A variety of such structures have been made using conventional nano- and microfabrication processes for patterning 2D elements and following sequential strain based folds into the final three dimensional configuration. The folding sequence has a large and sometimes irreversible effect on the ultimate shape of the micro-objects. Planar 2D elements used in micro-origami could be anything from standard integrated circuit (IC) and MEMS components to novel microfluidics and photonics systems.

Nowadays, out-of-plane micro- and nanostructures are desired mainly in applications where MEMS must interface with the external environment. For example, micro-origami has produced mirrors [2], [3], [4] stages [5], shutters [6] and corner-cube reflectors [7] to handle optical signals, out-of-plane directed cantilevers to act as field emitters [8] and nanopipelines to handle fluids [9]. A significant fraction of micro-origami research concerns actuators, including thermal actuator [10], [11], [12], [13], electrostatic actuators [6], [14] and chemical actuators [10], [12]. While these actuators' typical purpose is to manipulate cells and other small objects, a very practical application is one-time-use integrated levers [15] to assemble complex MEMS systems without human involvement.

However, while macroscale folding can be completed by hand or by using probes and automated machines, manual or mechanized folding becomes increasingly difficult at the smaller scales. There are a few methods or phenomena that used to produce 3D micro- or nanoscale objects. For example, capillary forces and surface tension usually do not have evident effects on solids at macro scales, but they become dominant at the sub-centimeter scale as the surface effects start overcome bulk effects. Both phenomena have been especially significant mechanisms in MEMS and nanotechnologies, but might bring undesirable difficulties at the same time (for instance capillary forces damaging thin MEMS cantilevers at the liquid-gas interface). [16] Meanwhile, capillary forces have been suggested as methods to assemble, orient, or deflect rigid objects in 2D at the water surface, and cause the spontaneous folding of an elastic sheet around a liquid droplet leads to a prearranged 3D shape. [17]. Self-folding due to magnetic [18] and surface forces [19], pneumatics [20], swelling of polymers [21], photosensitive polymers [22],

stressed thin films [23], [24], [25] thermal and shape memory alloy actuation [11], [26], [27], and muscular actuation [28], are other ways to manipulate micro- and nano-objects to create new objects of various shapes, sizes, and complexities.

### **1.1 SELF-ASSEMBLY**

Self-assembly is the fundamental principle that generates structural organization on all scales from molecules to galaxies. It is defined as a reversible process of unassisted arrangement of elements into structures or patterns that involve no human interference. As was mentioned earlier, strain and surface tension based self-assembly are potentially a very attractive method to form or reconfigure 3-D micro and nanostructures, and a variety of final shapes and structures might be achieved by altering the initial planar geometries.

### **1.2 BILAYER STRUCTURE**

The bilayer structure is widely found in plants and in animals. Several plants have bilayer structures which are able to alter of form or accumulate mechanical energy (due to strain) via changes in the environmental medium (temperature or humidity). For example, the wild geranium uses a sort of shoot using bilayer structures to spread out its seed [29]. The bilayer or bimorph structures can be used to amplify the small amplitude of the displacement, a similar principle used for the movement of cilia in lungs or in the eye of mammals and birds for the focusing of lens by changing their shapes [29].

The bilayer structures can be either actuators or sensors, using physical, thermal, electrical, chemical, or piezoeffects. It is commonly known that layered sheets of materials with mismatched strain will roll up with a well-defined radius of curvature, a

principle which has long been used in macroscopic systems such as bimetallic thermometer coils. Recently, however, researchers have applied this strained-bimorph principle to thin film bilayers at much smaller scales, using epitaxially grown semiconductor films to produce coiled cantilevers and tubes with internal radii down to 2 nm [30], [31], [2]. Metal/semiconductor systems have been used to produce nanoscrolls with radii less than 500 nm [32].

### 1.3 MICROACTUATORS AND DIFFERENT TYPES OF ACTUATION

As previously mentioned, microactuators allow microelectromechanical systems to implement physical functions (e.g., to convert an electrical signal into a mechanical signal). The actuation principle of MEMS actuator is dependent on the structural dimensions, technology, response time, maximum power consumption, force and torque as a function of displacement. Table 1 shows the most common classification of MEMS actuators and sensors by their actuation principle [33].

<b>Type of actuation</b>	<b>Force Range</b>	<b>Displacement</b>
Electrostatic	1 $\mu\text{N}$ – 1 mN	Up to 200 $\mu\text{m}$
Magnetic	0.1 $\mu\text{N}$ – 0.1 mN	10 $\mu\text{m}$ – 1 mm
Piezoelectric	10 $\mu\text{N}$ - mN	0.1 $\mu\text{m}$ – 1 mm
Thermal	~10 mN	Up to 250 $\mu\text{m}$

Table 1. Actuators: their actuation principle and characteristics.

Electrostatic actuation is the most frequently applied principle--combining simple technology, compatibility with electrical energy sources that are likely to be already available in other parts of the system for running logic circuits, and versatility. Perhaps the most commonly used type of electrostatic microactuator is the comb-drive one [34], [35]. Electrostatic actuators are faster, usually are not strongly affected by temperature changes and can function at high efficiency, but they have smaller stroke and do not generate large forces when compared to other types of MEMS actuators.

Piezoelectric actuators can offer large actuation forces with fast switching action, but cannot produce large strokes, require high voltage to function and yield highly temperature-dependent results. Piezoelectric bimorphs made of more than one material can exhibit larger displacement output at the expense of lower force output. MEMS piezoelectric actuators do not significantly exceed the performance of MEMS electrostatic actuators.

Electromagnetic actuators provide a relatively large stroke and force, but they need a solenoid with a magnetic core to generate a practical electromagnetic field. This requires a large power input, most of which is converted into heat.

Thermal expansion actuators can send a wide spectrum of displacements and forces that depends on the selection of expansion materials. Where large displacement actuators are needed, the material's thermal expansion coefficient is maximized, typically requiring the use of polymers [36]. However the power consumption is high and there is restriction by the speed of heating and cooling the microactuator for frequency of operation, and, thermal actuation can display much higher forces than electrostatic actuation. Thermal actuation could also enable movements away from the substrate and

towards the substrate; there is no pull-in voltage collapse of the structure as occurs in electrostatic actuation.

#### **1.4 NANOSTRUCTURES: NANOPARTICLES AND NANOTUBES**

Nanotechnology is expected to provide a route around physical limitations in miniaturizing current electronics fabrication techniques. Reducing each device in size obviously allows one to fit many more devices in a certain area. That isn't the only benefit of nanotechnology. As was pointed out earlier, basic properties and characteristics of materials can turn into completely different properties at the nanoscale. For instance, nanowires and nanotubes of common materials like carbon, silicon and oxides demonstrate outstanding electrical, mechanical, chemical and optical properties [37], [38] [39], [40], [41], [42], [43] and nanoparticles (NPs) hugely increase the surface area of a material to enhance its catalytic ability. Advancements in nanotechnology enable innovative applications in the biomedical field: sensing and imaging [44], [45], [46], drug and gene delivery [47], [48], [49], therapeutic and diagnostic applications [50], energy conversion [51], and many others [52], [53], [54].

Metal nanoparticles are being widely used in numerous applications due to the possibility of large batch fabrication and their useful geometries, including small size and correspondingly large surface-to-volume ratio, various shapes (e.g., nanoprisms, nanorods, or nanoshells), and adjustable photothermal and optical properties. Noble metal nanoparticles, gold nanoparticles (GNPs) in particular, are attractive due to their flexibility of synthesis and biofunctionalization, low toxicity and good biocompatibility, ease of detection, and strong and tunable surface plasmon resonance (SPR). Plasmon



resonance caused by the free electrons of the metal nanoparticle experience a collective resonant oscillation with respect to the positive metallic lattice in the presence of light which enhance the optical and photothermal properties of noble metal nanoparticles. The SPR can either radiates light (scattering), or be rapidly converted to heat (absorption). Alteration in size, shape, composition, and the surrounding environment of metal nanoparticles brings out exceptional control over the plasmon resonance properties and allows the design of nanostructures for specific biomedical applications. For instance, gold nanoparticles and nanoshells can be designed to either strongly absorb or scatter inside the near-infrared (NIR) wavelength region (650-950 nm). Gold nanoparticles (10-50 nm) present five or more orders of magnitude larger absorption coefficients compared with conventional dyes. They work as light-triggered “heaters” for selective localized photothermal therapy at the nanoscale, especially for selective heating and killing of cancer cells at much lower laser powers than would damage healthy tissue. Immunochemical coatings prevent significant binding to healthy cells, allowing differential heating of tumor and healthy cells when illuminated with infrared light in the biological transmission window. Nanorods or nanoshells can be tuned to the near-infrared (NIR) region of the spectrum, especially 650-900 nm, due to the high transmission of tissue, blood, and water in this window, through SPR to make in vivo imaging and therapy possible.

## **1.5 NANOPARTICLE-MEMS HYBRID DEVICE**

Inserting high quality nanoparticles into a standard semiconductor fabrication process will enable placement of nanoparticles on precisely defined areas of a bistable

MEMS “skeleton” to fabricate a hybrid device that folds rapidly in response to illumination. Two mechanisms contribute to this composite hybrid effect: (1) the effect of thermal mismatch of metal/silicon oxide bilayer film, and (2) tunable optical properties of gold nanoparticles. These inorganic MEMS structures reversibly store strain energy that can be triggered to release within less than a second. Noble NIR-responsive metal nanoparticles have high absorption and low scattering of light in this wavelength region that leads to heating and thermal expansion of the medium surrounding the nanoparticle. Beyond basic heating, the tunability of the absorption wavelength can enable the hybrid micro-nano devices to be addressed wirelessly by wavelength multiplexing instead of the direct current that is usually required to drive MEMS actuator.

The ability to integrate metal nanoparticles-MEMS hybrid into biological systems has greatest impact in bioapplications. Biocompatibility will make it possible to create cellular-scale mechanical actuators that can be distributed throughout a tissue sample and driven remotely using infrared light.

## CHAPTER II

### ORIGAMI FABRICATION OF MICROSTRUCTURED 3D DEVICES BASED ON STRESS-MISMATCHED LAYERS

The ancient Japanese art of paper folding known as origami allows generating complex three-dimensional objects from planar two-dimensional (2D) plates. A similar approach can be utilized to create 3D micro- and nanostructures including electronic, optical or mechanical devices using conventional layer-by-layer lithographic methods [55]. Standard planar microfabrication tools and techniques are used to make 2D structures or patterns, creating a predetermined pattern of folds on a thin substrate that is the equivalent of “paper” used in conventional origami. The folding actuation mechanism--whether based on intrinsic stress, thermal, electric, magnetic, or photoactuation, as well as the creases or hinges along which the segments fold, are patterned into these devices in one fabrication process. At the end of the process, actuation is triggered for automatic rapid folding of the structures out of the plane. These built-in actuation methods must be controllable and compatible with the fabrication technology.

The Nanostructured Origami™ process [56] allows fabricating out-of-plane micro- and nanostructures that would not be possible with conventional planar lithography and offers a few extra advantages. For example, complications related to multilayer fabrication are avoided by patterning and repeatedly folding only one layer.

Alignment and positioning of the folded layers can be improved through the use of pyramid-shaped alignment features.

Stacked sheets of materials with mismatched strain roll up with a well-defined radius of curvature that depends on their thickness, modulus, and the amount of strain mismatch. Recent research efforts demonstrate applications of this strained-bimorph construction technique to thin film bilayers at much smaller scales than ever before, using epitaxially grown semiconductor films (Si/SiGe, InGaAs or GaAs/InGaAs) to produce coiled cantilevers, nanocoils and tubes with internal radii varying from some nanometers to several microns [24], [57], [32], [58]. Free-standing strained heteroepitaxial layers automatically bend when the layers are released from the substrate (Figure 1(e)). This process requires heteroepitaxial layers with precisely controlled thicknesses and compositions, and a suitable sacrificial layer built in under the heteroepitaxial layer.

Ion implantation of silicon nitride membranes with  $\text{Ga}^+$  ions is well suited for folding membranes into three-dimensional micro-structures for device fabrication [59]. Localized ion irradiation into a silicon nitride cantilever creates great stress gradients and folds the cantilever at the irradiated area. Cantilever thickness, the ion dose and the sputter depth into the silicon nitride are all factors that define the fold angle and radius of the cantilever.

The well-known phenomenon that nanoscale grains can produce extremely high intrinsic stress through grain coalescence during a film deposition process is another method to curl up nanostructures (Figure 2.1(d)). Due to the grain coalescence of Sn, the stress within the Sn film is large enough to cause Sn/Ni and Sn/ $\text{Al}_2\text{O}_3$  bilayers to curl up with nanoscale radii of curvature [60].

The laser origami technique presents a possible alternative for generating 3D self-folding designs [55]. This method generates the pop-up features through laser microfabrication, followed by selective laser cutting, and, finally, uses laser ablation to achieve out-of-plane actuation (Figure 1(a)). This was accomplished by back-irradiating an indium-tin oxide (ITO)/copper multilayer film stack on a fused silica substrate with a 355nm UV laser pulse. Instead of vacuum-deposited thin metal films, it is also possible to use metallic nanoinks (a highly viscous, organic solutions with suspended metallic nanoparticles), with the same laser fabrication method to generate the desired 3D microstructures. The inks that function as the activation layer are transferred by laser printing, and then tailored by selective laser curing of the inks which causes significant volume shrinkage across the hinges to create folding 3D assemblies.

Metal bilayer films are not the only materials that work as tensile-stressed layers to achieve folding. The SU-8 polymer is used often to define structural layers for fabrication of MEMS structures with pre-programmed three-dimensional shapes (Figure 1(c)). Stress mismatch introduced between the two layers during the cross-linking of a second SU-8 film produces a variety of self-folding stress-inducing structures [61].

The novel discipline of origami engineering extends to the nanoscale in biomedical applications, such as strategically folding molecules including DNA into prescribed shapes to tailor their properties (Figure 1(b)) [62], [63] and to the macroscale with flexible medical stent grafts [64]. New origami stent grafts are made from a Ni-rich titanium/nickel (TiNi) shape memory alloy (SMA) single foldable foil with hill and valley folds. The expansion or folding of the stent graft is accomplished either by the

shape memory effect at body temperature or by making use of the property of superelasticity.

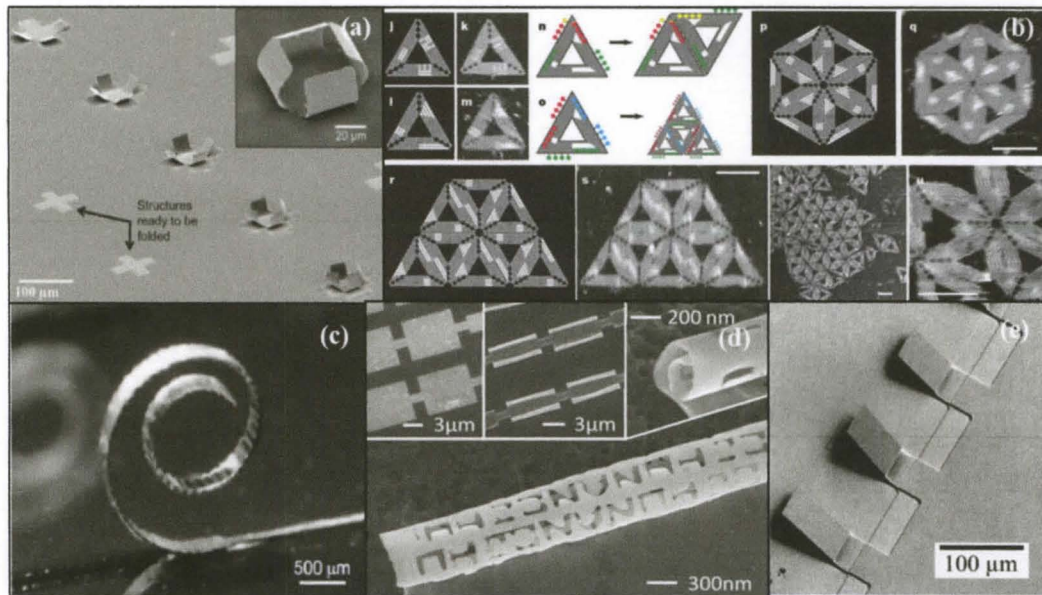


Figure 1. Examples of micro- and nanostructures created with origami technique. (a) Laser-bent microenclosures at various stages of closure generated by laser origami [55], (b) Patterning and combining DNA origami into desired shapes [62], (c) spiral structure based on the multi-user SU8 polymer MEMS process [61], (d) Curved nanostructure created with a coalescing Sn film atop a relatively neutral stressed Ni film [8], (e) Row of AlGaAs/GaAs dielectric mirror and an InGaAs strained layer grown by molecular-beam epitaxy on a GaAs substrate with different lengths after release from the substrate [2].

The method of producing 3D cell-laden microstructures by exploiting the cell traction force to drive the self-folding of microfabricated flat plates is called cell origami [65]. This technique does not require the conventional need for external actuation forces, such as thermal actuation or electromagnetic forces to produce 3D microstructures.

In this chapter, the intrinsic-stress method was employed to achieve three-dimensional microstructures. The distinctive features of this work over previous literature are that we investigate the effect of folding order on the final shape of these three-dimensional micro-objects, and explore the ability of the structures to actuate between their fabricated final shape and other shapes that are local minima in the strain energy landscape.

The strain mismatch was created by patterning a metal-on-SiO<sub>2</sub> layer on a silicon substrate. Thermally grown SiO<sub>2</sub> generally has compressive stress, while the metal films used in this work have tensile stress. The silicon is isotropically etched to undercut and release the metal-oxide bimorphs. The width of features in a single photomask determines the folding sequence; because the silicon etch process will undercut the narrowest lines first, enabling those structures to curl up from the substrate before other features are released. It was demonstrated that folding sequence has a large and sometimes irreversible effect on the ultimate shape of the micro-objects.

## **2.1 THEORY OF THERMAL BENDING**

Bimorph structures are composed of active layers (two materials) with different properties. Usually, these structures take the form of thin strips, beams or cantilevers. Every bimorph structure bends due to imbalanced strains in those two layers, and the

amount of bending is sensitive to temperature, electric fields, and other variables that affect the stress in either of the two materials. Strain-mismatched bimorphs attain a radius of curvature that minimizes the potential energy of the entire structure. Like a spring with stored elastic energy, a thin film that is compressively stressed while constrained to the substrate will expand when released. A single released layer will bend only at the release point, and expand volumetrically elsewhere, resulting in a folded over flap [9]. However, if the layer is coated with another film having less compressive stress or tensile stress, the upper film will constrain the expansion at the top of the lower film, causing the released bilayer to curl uniformly upward from the substrate (Figure 2). Beam equations developed for much larger structures can account for most of the features seen in microscale strain architecture devices, although the approximations become less accurate as the curvature radius becomes small relative to beam thickness [14]. For a released beam of uniform width, with no applied moments, the reciprocal of the radius of curvature is given by Equation (1)–(4). Those formulas for deflection of a bimorph beam was first analyzed by Timoshenko in 1925 who applied the analysis to bi-metal thermostats [66]

$$\frac{1}{\rho} = \frac{6\varepsilon(1+m)^2}{d[3(1+m)^2 + (1+mn)\{m^2 + \frac{1}{mn}\}]} \quad (1)$$

$$d = d_1 + d_2 \quad (2)$$

$$m = \frac{d_1}{d_2} \quad (3)$$

$$n = \frac{E_1}{E_2} \quad (4)$$



$$\varepsilon = \frac{l_2 - l_1}{l_1} \quad (5)$$

In these equations above,  $\rho$  is the radius of curvature,  $d$  is the combined thickness of the two layers  $d_1$  and  $d_2$ ,  $\varepsilon$  is the in-plane biaxial strain or fractional difference in the between the two films unconstrained relaxed lengths of the two layers,  $n$  is the ratio of the Young's moduli of the layers and  $m$  is the ratio of their thicknesses ( $d_1/d_2$ ).

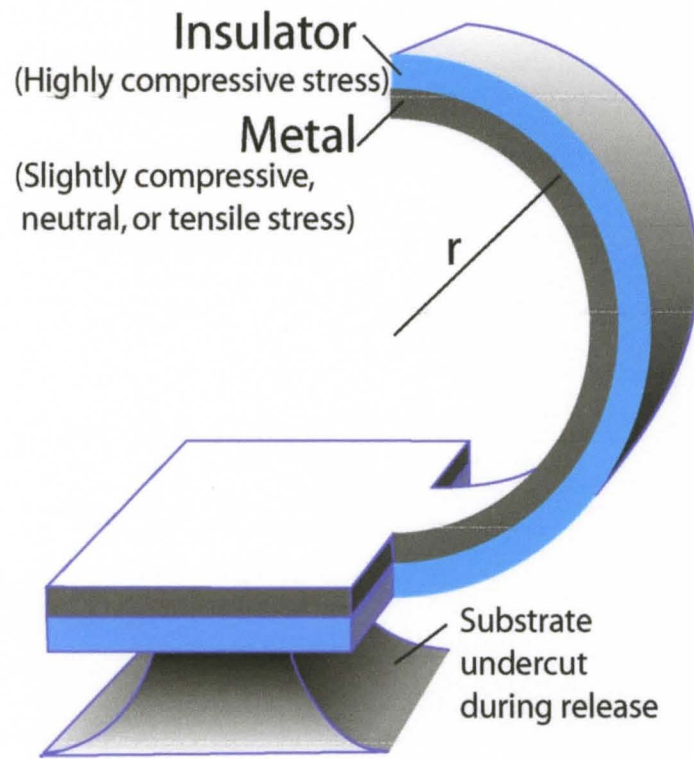


Figure 2. Schematic of a metal–insulator bimorph bending because of strain mismatch induced curvature upon release from the substrate.

In case of bi-directional curvature for the narrow beams typical of MEMS structures, transverse bending moment is important and should be included in consideration by replacing the elastic modulus with the biaxial modulus,  $\nu$ , of each

material. Neglecting the role of Poisson's ratio has been documented to result in errors as large as 50% for representative MEMS structures [67]

$$E' = \frac{E}{(1 - \nu)} \quad (6)$$

where  $\nu$  is Poisson's ratio and  $E$  is the elastic modulus.

For many choices of materials, the biaxial moduli are similar ( $\nu=0.5-2$ ), making this parameter's effect on the radius of curvature small compared to the effects of strain mismatch and film thickness. Considerable insight can be gained by assuming that both layers have the same biaxial moduli ( $\nu=1$ ). Equation (1) then becomes

$$\frac{1}{\rho} = \frac{6\varepsilon d_1 d_2}{d^3} \quad (7)$$

Notably, the inverse radius is directly proportional to the strain mismatch  $\varepsilon$ , which depends upon the choice of materials and deposition conditions.

Often, the strain mismatch between two layers is an unwanted effect. For instance, bimorph cantilevers occur in atomic force microscopy with current-measuring probe tips that have a metal trace on a silicon bulk micromachined structure. The problem is non-zero tip deflection (or curvature) at room temperature due to residual stress in the layers. Deposition conditions and crystal-growth conditions put nearly all films in a state of residual internal stress [60]. The stress may be compressive or tensile. Residual stress is consisted of two components: intrinsic stress that reflects the internal structure of a material and develops during the film nucleation, and thermal stress that outcome from deposition temperature conditions and often dominates. In general, the intrinsic stress in a film depends on thickness, deposition rate and temperature, ambient pressure, method of

film preparation, type of substrate used, type of machine used for fabrication, and a number of other parameters. Intrinsic stress is less clearly understood, but a number of stress-causing phenomena have been suggested to explain it: lattice mismatch between the substrate and the film, rapid film growth, recrystallization processes, grain boundaries, phase transformations, incorporation of impurities or doping into the film, atomic peening, microvoids, and gas entrapment [68], [69].

Since the minimum radius determines the lower size limit of objects that can be fabricated by this method, it is useful to extract further design rules by minimizing the reciprocal of Equations (1) and (2). For two layers with equal biaxial modulus ( $n = 1$ ) and a fixed total thickness  $d$ , the minimum radius occurs when the top and bottom layers have equal thicknesses, ( $d_1 = d_2$ ).

However, from a practical standpoint, oxidized wafers are typically purchased in a large batch, or oxide is grown on several wafers in one run, so the bottom layer often has a fixed lower layer thickness,  $d_2$ , while the upper metal layer thickness  $d_{21}$  is varied in subsequent processing. In this case, when both materials have equal modulus, the radius is minimized when the top layer's thickness is half that of the lower layer. Adding more material to the top layer only increases the total thickness  $d$  in the denominator, producing a larger radius of curvature. In general, to minimize the radius if the biaxial moduli are unequal, the layer with the larger modulus must be thinner than the limits set by the aforementioned design rules.

## **2.2 FABRICATION PROCESS**

Figure 3 illustrates the fabrication steps used to produce metal-oxide bimorphs on silicon wafers. To create a compressively stressed lower layer impervious to silicon etching, thermal oxide ( $\text{SiO}_2$ ) was grown at  $1000^\circ\text{C}$  on silicon wafers (Figure 3(a)). Thermally grown 400 nm oxide on silicon has a very high compressive stress due to the differential thermal expansion of the coating and substrate as the wafers cool.

The oxidized wafers were treated with hexamethyldisilazane (HMDS) adhesion promoter by spinning at 4000 RPM for 10 seconds, followed by coating with Shipley 1827 positive photoresist (MicroChem) at the same spinner parameters. The wafer should then be soft baked on hot plate at  $115^\circ\text{C}$  for 90 seconds for partial evaporation of photoresist solvents (Figure 3(b)). After UV light exposure in a Karl Suss contact aligner (SUSS MicroTec) through a photomask, resist was developed in Microposit MF319 developer (MicroChem) for one minute to clear any exposed areas followed by rinsing and drying (Figure 3(c)). Metal layers were then coated onto the wafer in a sputtering system (Technics Inc) as shown in Figure 3(d). Three types of metal layers: chromium–nickel–chromium (Cr/Ni/Cr), Ti/NiTi (shape memory alloy) and Ti/Pt layers were used in this study.

### **2.2.1 Cr/Ni/Cr STRUCTURE**

For the chromium (Cr) adhesion layer, sputter conditions were 120 W DC power, 30 mTorr argon chamber pressure, for three minutes. For nickel (Ni), 350 W RF power, 30 mTorr argon pressure and five minutes. The Ni was topped by a second Cr deposition similar to the adhesion layer to protect it from subsequent etching if needed. Combined

layer thickness was measured at 160 nm using a Dektak profilometer (Veeco Instruments Inc.).

### **2.2.2 Ti/NiTi STRUCTURES**

For the titanium (Ti) adhesion layer, sputter conditions were the same as for Cr. For the NiTi, conditions were the same as Ni, except an equiatomic NiTi target was used. Three minutes nickel deposition followed by 10 minutes NiTi deposition resulted in a total layer thickness of 270 nm.

### **2.2.3 Ti/Pt STRUCTURES**

A titanium adhesion layer of ~60 nm followed by a platinum layer of 180 nm. Sputtering was performed at 300 W RF power for Ti, and 120 W DC power for Pt, with an Ar sputtering gas pressure of 40 mTorr.

After metallization process, excess metal was removed by liftoff in acetone followed by water leaving a metal pattern. The wafer was baked at 115°C for five minutes for dehydration and the same photolithography steps were performed as above. The resist was UV exposed through the photomask that opens certain areas to etch through the oxide in alignment with the metal pattern, then developed in MF319 and baked two minutes at 115°C (Figure 3(e)).

While the exposed oxide was removed using plasma etching (Figure 3(f)), with 240 mTorr pressure of CF<sub>4</sub>:H<sub>2</sub> at a partial pressure ratio of 60:40 and a RF power of 260 W. The patterned metal was used as a self-mask to transfer the design into the

underlying oxide. After 10 minutes of etching, the 400 nm oxide was completely removed from any areas unprotected by metal.

Bimorphs were released from the wafer by undercutting in a  $\text{XeF}_2$  dry silicon etcher, Xactix Inc (Figure 3(g)). This isotropic etch process completely removed silicon from the underside of the oxide layer, and left a silicon cusp on the substrate at the centerline of the released structure. The etch rate depends on the area of exposed silicon and will vary from pattern to pattern. However, wider lines always require more etch cycles for complete release, providing a mechanism to control the folding sequence of micro-objects based on  $\text{XeF}_2$  etch time. The  $\text{XeF}_2$  etch process is highly selective to silicon, enabling a wide range of metals and other materials to be used in the process.

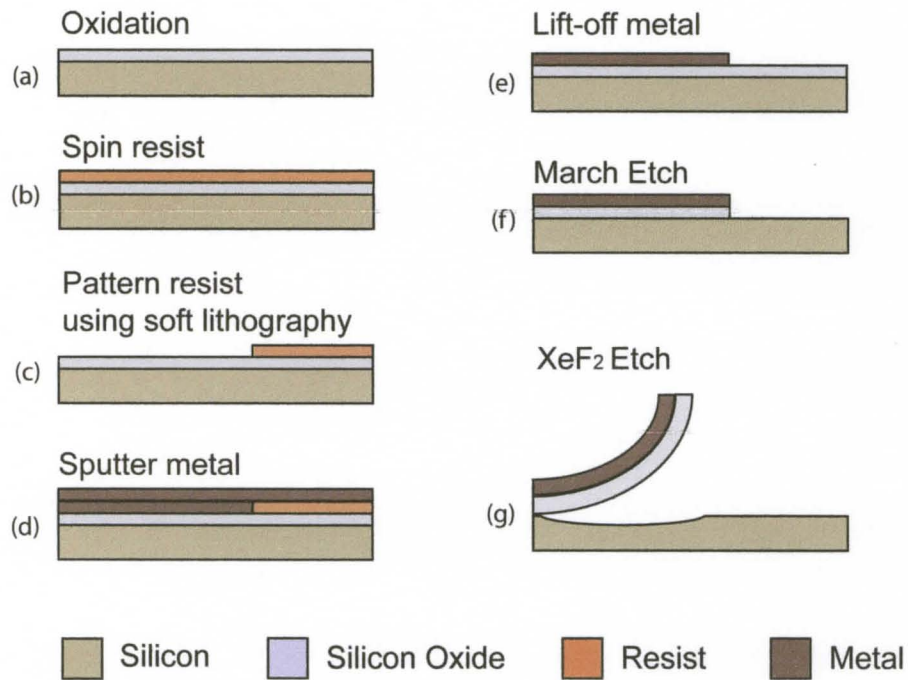


Figure 3. Fabrication process flow. (a) Silicon wafer with 400–500 nm thermal oxide, (b) - (e) A 200–300 nm thick metal pattern is applied using photoresist liftoff, (f) The metal acts as an etch mask to pattern the oxide in a  $\text{CF}_4/\text{H}_2$  plasma etch, (g) The metal-oxide bimorph is released by etching the silicon in  $\text{XeF}_2$  gas.

## 2.3 DISCUSSION OF MATERIAL PROPERTIES AND PREDICTED CURVATURE

The properties of materials used in this work are listed in Table 2 together with calculated curvature radii from Equation (1) for both Cr/Ni/Cr devices and Ti/NiTi devices. Note that these calculations do not account for the Cr or Ti adhesion layers, instead using the Ni or NiTi biaxial elastic modulus for the entire metal film.

Strain mismatch and film thickness are far more important than elastic modulus in determining the curvature [66]. The strain mismatch required in Equation (1) was then computed as

$$\varepsilon = \frac{\sigma_{metal}(1 - \nu_{metal})}{E_{metal}} - \frac{\sigma_{oxide}(1 - \nu_{oxide})}{E_{oxide}} \quad (9)$$

Values for the elastic modulus and Poisson's ratio were obtained from the literature as noted, using values reported for thin films instead of bulk materials wherever possible. Where two values appear, these were averaged for use in the calculation.

Since residual film stress is highly dependent upon processing conditions, the biaxial stress  $\sigma$  of oxide and metal films were measured by profilometry. Veeco's Stress Measurement Analysis for Dektak® stylus profilers was used to calculate tensile and compressive stresses and displays the results [70]. The standard stress measurement technique is direct: one measures the curvature of the substrate of a substrate before and after film deposition along the same trace. The stress measurement analysis uses the bending plate method (or Disk method) to calculate stress in a deposited thin film layer, based upon the change in curvature and material properties of the film and substrate [71]. Stress in thin films affects substrate curvature as described in the Stoney equation [72]



$$\sigma = \frac{1}{R} \frac{E}{6(1-\nu)} \frac{T^2}{t} \quad (10)$$

where  $R$  represents the measured radius of curvature of the bent substrate,  $E/(1-\nu)$  the biaxial modulus of the substrate,  $T$  the thickness of the substrate, and  $t$  the thickness of the applied film.

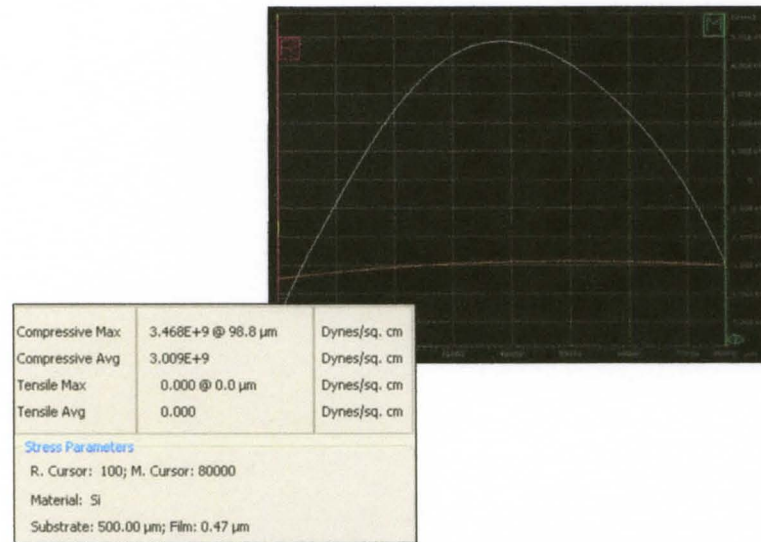


Figure 4. Stress results summary window and stress measurement results.

The white trace indicates compressive stresses are present in  $\text{SiO}_2$  film.

Figures 4-6 represent a few examples of thermal stress measurement results for  $\text{SiO}_2$ , Cr/Ni/Cr and Ti/NiTi (SMA) deposited thin film on Si substrate. Negative values of stress are compressive and have convex profile of surface; positive values are tensile with concave profile of substrate surface. The units of stress are dynes/cm<sup>2</sup>, where 1 dyne is 10<sup>-5</sup> Newton.

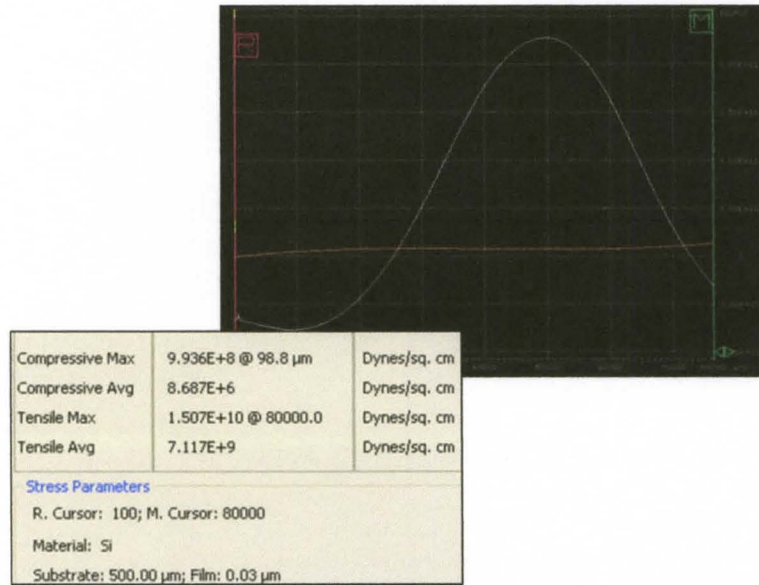


Figure 5. Stress results summary window and stress measurement results. The white trace indicates tensile stresses are present in SMA film.

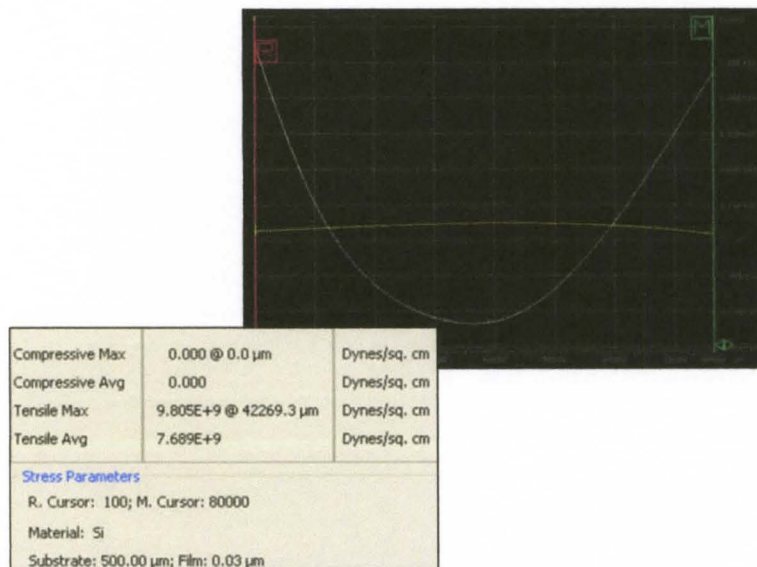


Figure 6. Stress results summary window and stress measurement results. The white trace indicates tensile stresses are present in Cr/Ni/Cr film.

Typical values of the elastic modulus, Poisson's ratio, average values of measured stresses for oxide and used metals represent in Table 2.

Device composition	Material	Elastic modulus (GPa)	Poisson's ratio	Measured thickness (nm)	Measured residual stress (MPa)	Calculated radius ( $\mu\text{m}$ )
Cr/Ni/Cr on oxide	Thermal oxide	71 [73] 83 [74]	0.20 [77]	400 $\pm$ 20	-300 $\pm$ 25	64 $\pm$ 7
	Cr	140 [14]	0.21 [78]	Combined metal film	Combined	
	Ni	210 [75]	0.24 [76]	160 $\pm$ 20	775 $\pm$ 50	
		190 [76]			(tensile)	
Ti/TiNi on oxide	Thermal oxide	Same as above	Same as above	475 $\pm$ 20	Same as above	40 $\pm$ 12
	Ti	90 [79]	0.33 [82]	Combined metal film	Combined	
		60 [80]	0.33 [81]		750 $\pm$ 100	
	TiNi	29 [81]		270 $\pm$ 20	(tensile)	

Table 2. Material properties, layer thickness, stress and calculated curvature radius for Cr/Ni/Cr/SiO<sub>2</sub> and Ti-TiNi/SiO<sub>2</sub> bimorph structures.

## 2.4 SIMPLE STRUCTURES WITH TWO CHARACTERISTIC RELEASE TIMES

The simplest structures described in this chapter have two characteristic line widths: one narrow width for released structures and one relatively large width to anchor the structures to the surface. Making the anchor width much greater than that of the released structures means that exact etch timing is not critical for achieving reproducible results. SEM images indicate that features roll up along their longest dimension, as shown for the radial design in Figure 7(a) photomask layout and SEM image of the resulting toroid with 400 nm oxide, 50–60–50 nm Cr/Ni/Cr film. In all SEM images, a ridge of silicon appears on the substrate at the centerline of the original two-dimensional pattern. When the lines are angled off-axis from the center of the circle, the slats of the toroid become tilted with respect to the surface, Figure 7(b) and Figure 7(c).

The observed 64  $\mu\text{m}$  curvature radius in Figure 7(a) is very close to the calculated radius of  $64 \pm 7 \mu\text{m}$ . While neighboring structures were nearly identical to each other, the observed radius varied from 60 to 100  $\mu\text{m}$  across the 4 inch wafer, due to local thickness or stress variations in the sputtered metal film.

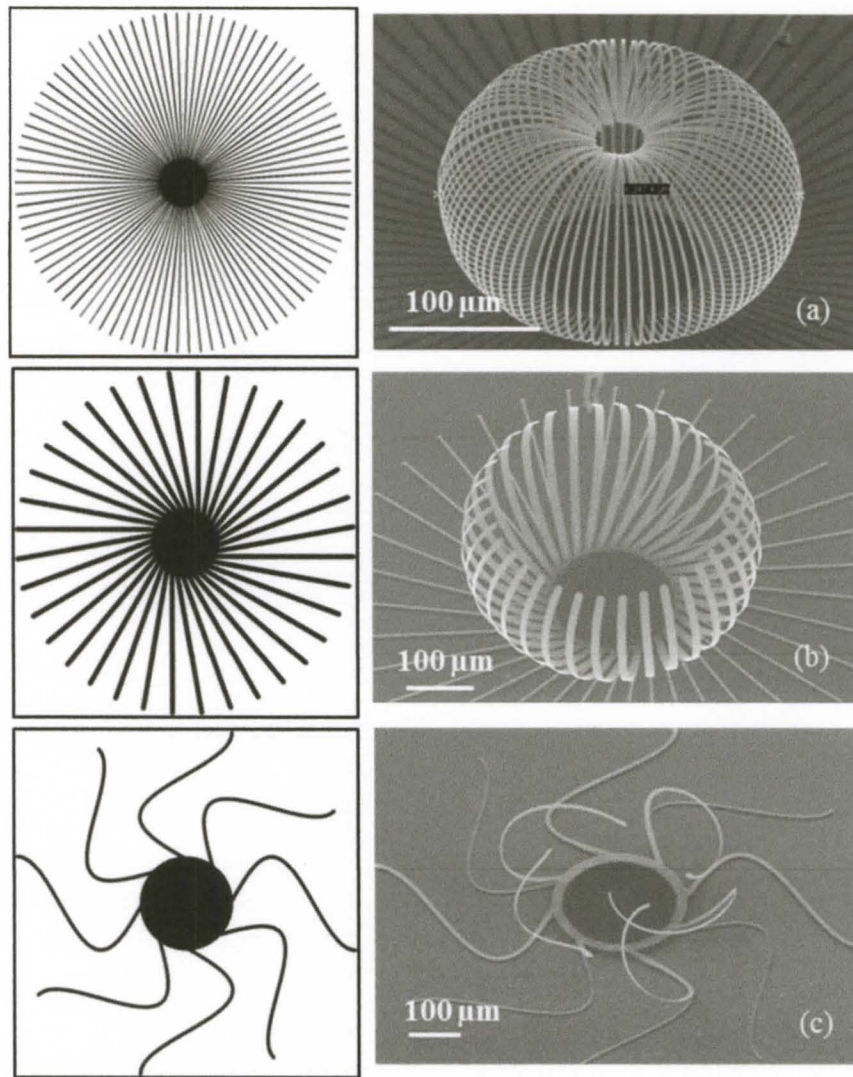


Figure 7. (a) Layout and SEM image of released toroid structure, (b), and (c) Layouts and SEM images for tilted radial structure with arms off-axis from the center.

## 2.5 STRUCTURES WITH RANDOMLY DETERMINED RELEASE

### TIMES

The seemingly unpredictable folding of a 'zigzag' structure points to the importance of the release sequence in determining the final three-dimensional shape. Figure 8(a) shows the layout of a repeating, symmetric zigzag with anchor pads  $30\ \mu\text{m} \times 30\ \mu\text{m}$  on each side, short central bar of zigzag is  $5\ \mu\text{m}$  wide.

Due to random imperfections in the photolithography process, either the left or right bend in the zigzag is released from the surface first, as shown in the partially released structures in Figure 8(b). After initial release, the rest of the zigzag is undercut, and the fully released structure takes on a left- or right-oriented conformation that produces a local minimum for the stored elastic energy. Continued silicon etching after this point, until only a  $10\ \mu\text{m}$  diameter attachment point remains at the center of the square anchor pads, does not change the left or right orientation of the structures. Although the initial pattern is symmetric, the two possible release sequences produce a set of mirror-image final structures.

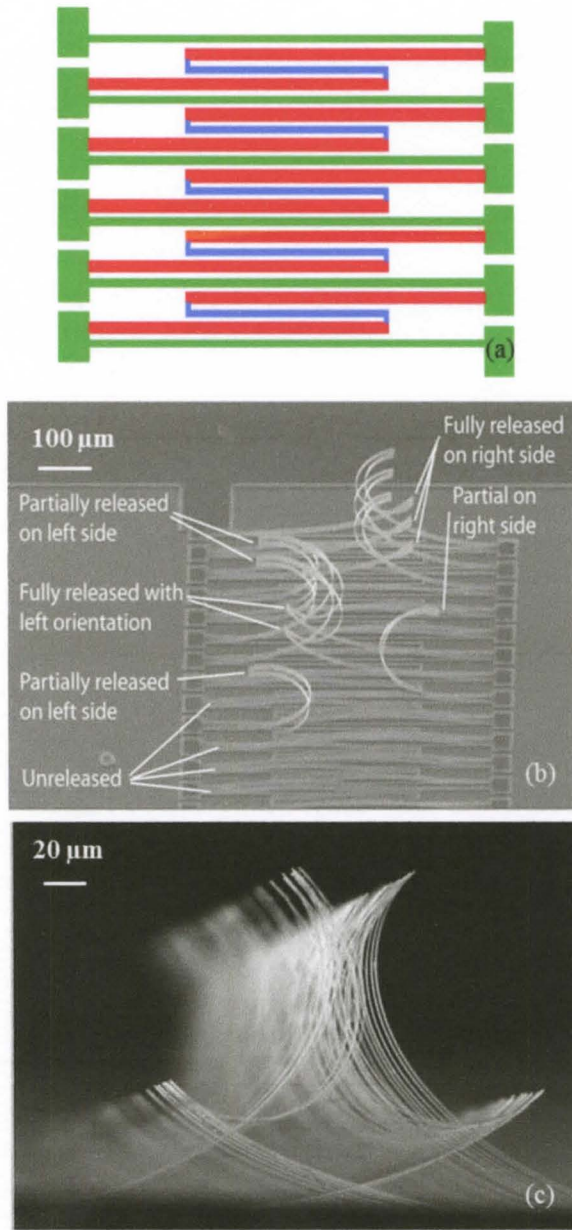


Figure 8. (a) Layout for symmetric zigzag structure while long bars are 7 μm wide, (b) SEM image shows arrangement of bimorphs during the release process, (c) SEM image of a side view of released zigzag structure.

## 2.6 STRUCTURES WITH ENGINEERED INCREMENTAL RELEASE

### TIMES

To study the interaction of structures having several incremental release steps, we created a series of nested 'V' structures with 1  $\mu\text{m}$  differences in their line widths. One type of structure had the widest line on the outside, and was expected to produce independent structures. The other type had the widest line on the inside, and was expected to tangle as the narrowest V released first and curled over the still unreleased lines. Figure 9(a) shows the layout for the untangled V shape, and Figure 9(b) is a scanning electron micrograph above this structure after the three narrowest lines have released. Figure 9(c) shows the 'tangled-V' layout and Figure 9(d) a top view after the first three lines have released. In the untangled structure, the lines remain independent, while in the tangled version, the lines have wrapped around one another. Figures 9(b) and (d) use Ti-NiTi rather than the previous Cr/Ni/Cr metal films. The Ti - NiTi devices are expected to have a smaller radius of curvature ( $40 \pm 12 \mu\text{m}$  versus  $64 \pm 7$  for Cr/Ni/Cr), but the curvature Equation (1) does not apply directly to these constrained structures.

Figure 10 is a side view of another tangled structure made from Cr/Ni/Cr, with 15 instead of 5  $\mu\text{m}$  spacing between the lines, showing the nature of the overlap that is initiated by narrow lines curling over wider lines before the wider lines are released, as well as a qualitatively larger radius of curvature than similar Ti-NiTi structures. Simply reversing the order of the line widths has created dramatically different final structures.



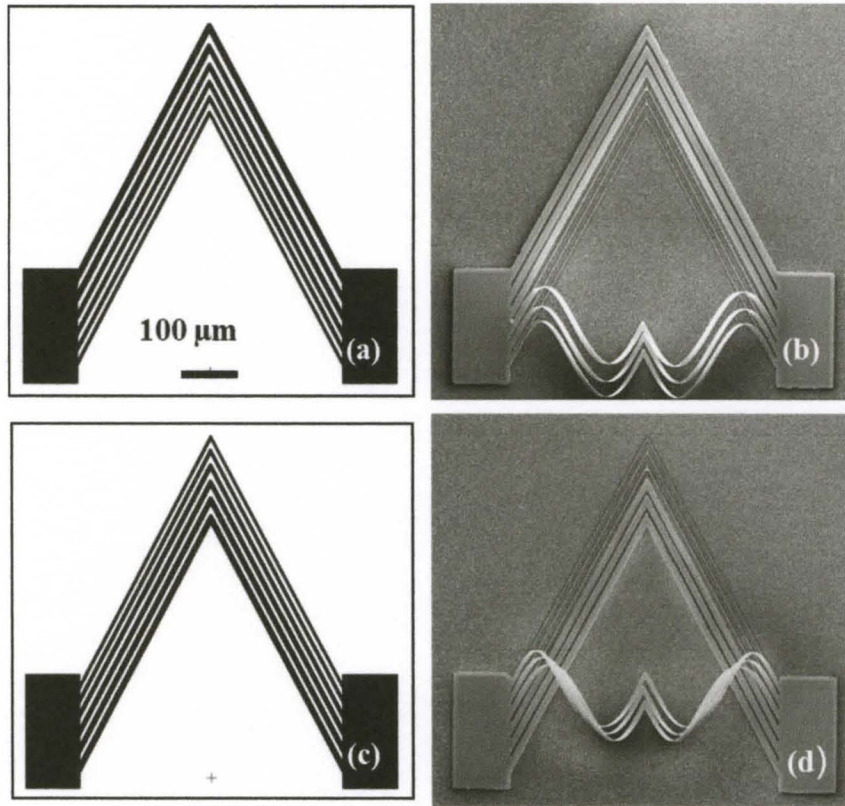


Figure 9. (a) Layout of untangled V-structure. Line widths range from 10  $\mu\text{m}$  to 5  $\mu\text{m}$  in 1  $\mu\text{m}$  increments, with 5  $\mu\text{m}$  spacing. (b) Partially released untangled V-structure, showing independent 5, 6 and 7  $\mu\text{m}$  wide structures. Oxide thickness is 475 nm, Ti-TiNi thicknesses are 50 and 220 nm respectively. (c) Layout for tangled-V structure, with linewidth order reversed from untangled-V structure. (d) Partially released tangled V-structure, showing 5, 6 and 7  $\mu\text{m}$  structures wrapped around each other due to release sequence. Materials and thicknesses the same as (b).

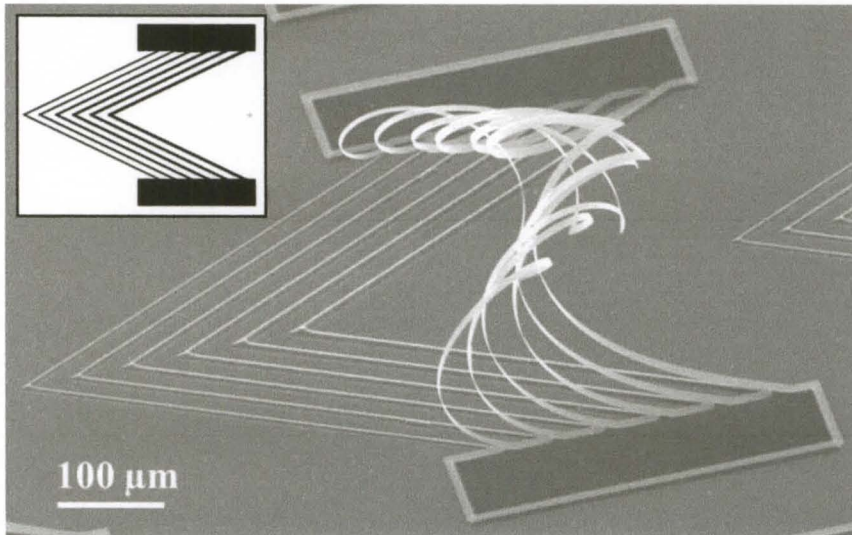


Figure 10. Side view of a fully released tangled-V structure with 15  $\mu\text{m}$  spacing between lines. Oxide thickness is 400 nm and Cr/Ni/Cr thicknesses are 50–60–50 nm.

## 2.7 STRUCTURE WITH CAREFULLY CONTROLLED RELEASE

### SEQUENCE

The layout for a three-step sequence for fabricating a multiaxis loop structure is illustrated in Figure 11(a), where the expected 100  $\mu\text{m}$  coil radius has been used to design three single-turn loops which will orient themselves along three orthogonal planes when released. The 5  $\mu\text{m}$  wide coil releases first (red line), followed by the 6 (blue line) and 7  $\mu\text{m}$  coils (green line). Figure 11(b) shows the resulting structure, with overlaps at the ends of the three loops. The resulting coil radius is 90  $\mu\text{m}$ , used oxide thickness is 400 nm and Cr/Ni/Cr thicknesses are 50–60–50 nm.

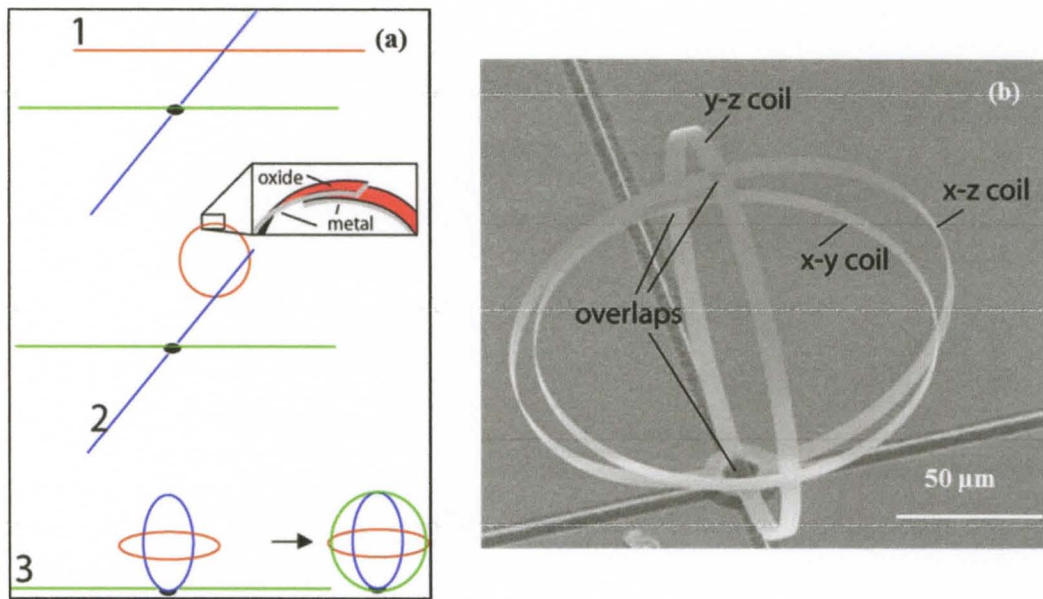


Figure 11. (a) Three-step fabrication sequence for a three-axis loop structure from a single photomask. Loop 1 forms and is lifted up by formation of loop 2, after which loop 3 wraps around the previously formed loops. (b) The finished structure showing coils in x-y, x-z and y-z planes.

## 2.8 RELEASED STRUCTURES AS THERMAL ACTUATORS

Thermal actuation in our metal/oxide material system by heating of metal through a pulsed current applied at bonding pads connected to the structure. Although it is likely that the metal and insulator layers are nearly the same temperature, the top metal surface expands relative to the underlying insulator because its coefficient of thermal expansion is approximately 200 times larger than that of the insulator. Scanning electron microscopy was used to capture the actuation of fabricated bilayer structure, and nanomanipulator was employed to supply a voltage to the actuator inside of SEM chamber.

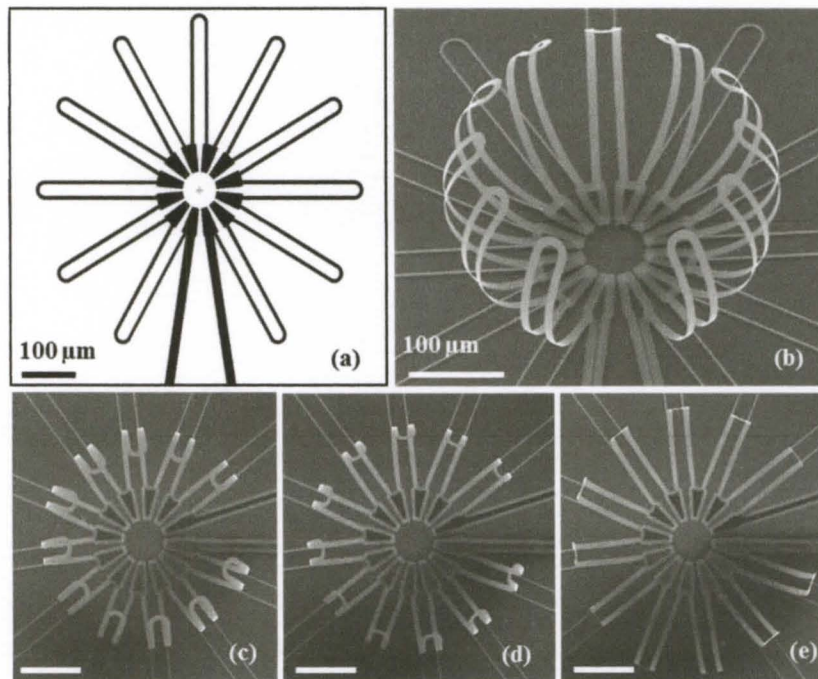


Figure 12. (a) Layout of microcage, (b)-(e) SEM of 250 micron diameter microgrippers as temperature increases from 30°C to approximately 200°C. Differential thermal expansion unfolds the actuators.

Estimated voltage to heat the metal by approximately 200°C is less than 40 V, which should open the cage fingertips by 90 degrees (Figure 12). Power consumption is estimated at 0.2 mW during the open state. At the 100 micron radius and 560 nm bilayer thickness, the prototype devices have applications as microgrippers. However, by comparison to strain architecture results in the literature, the overall cage diameter can potentially be reduced to below 1  $\mu\text{m}$ . Detailed exploration of similar structures in metal/diamond is presented in [75], [11].

## **2.9 POSSIBLE APPLICATION AND CONCLUSIONS**

The metal-oxide bimorph release process detailed here can produce highly uniform and predictable structures, as long as there is good control over film stress and thickness, and the effects of the folding sequence are considered during the design phase. Careful control of the folding sequence adds the ability to make sophisticated multi-axis structures from a single photomask [25]. Width differences of 1  $\mu\text{m}$ , readily accessible by contact photolithography, have been used to control the release order. This may be considered an upper limit for the linewidth difference needed for reproducible folding order. Higher resolution patterning will enable investigations into the lower limit of this sequential assembly technique.

The randomly released zigzag structures observed in Figure 8 may suggest a path to bistable structures with applications as latching mechanical actuators, since these have found two mirror-image energy-minimizing configurations. In this application, the dimensions and materials must be optimized to avoid permanent deformation in the initial configuration.

Tangled V-structures in Figures 9 and 10 may find applications as temporary or permanent clips to join micro- or nanostructures together on a substrate. Since these structures have contact pads at each end, they may be thermally actuated to open and close by Joule heating.

The multi-axis coils illustrated in Figure 11 have potential applications as isotropic electromagnetic resonators and antenna elements, and will retain their shape even if detached completely from the wafer as separate particles. Such particles, if designed to have a narrow electrical resonance, may function as microtaggants for electromagnetic identification, or polarization-insensitive antenna array elements. When designing such multi-step folding structures, it becomes clear that several different patterns may lead to a similar final shape; for instance, in Figure 11 the narrow 5  $\mu\text{m}$  crossbar could have been placed near the other end of the 6  $\mu\text{m}$  line to produce a horizontal coil. In this case, the optimal 2D pattern might be the one that maximizes packing density on the wafer, since neighboring structures must not touch or cross in the original layout. If routing problems become difficult, it is also possible to integrate additional metallization and low-temperature oxide/silicon coating steps before the structures are released. Doing so can enable structures that cross, and structures with different curvature radii on a single wafer, moving beyond the single photomask process described earlier.

Possible applications for electrically-controlled microactuators (Figure 12) include microgrippers, which is useful in bioapplications where it can manipulate or separate individual cells and particles, or perform localized cell measurement. Another application is microfabricated containers that keep small amounts of environmental or

biomedical samples for analysis. These structures remain connected to electrodes for thermal actuation, electrochemical sample collection, and gas generation through electrolysis. Results are shown for collection of dissolved metals by electroplating using small voltages and currents that are compatible with the power resources of wireless sensor networks. Such containers will be useful for rapid in-situ analysis of concentrated samples, for maintaining a sample archive that can corroborate the results of an in-situ biochemical sensor or for time-stamped collection of samples for offsite analysis using equipment that is unavailable in the field such as mass spectrometry or electron-beam based analysis methods [83].

## **CHAPTER III**

### **BISTABLE MEMS STRUCTURE**

#### **3.1 DEFINITION OF BISTABILITY AND BISTABLE MECHANISM**

The concept of stability is used in many different scientific fields such as economic models, numerical algorithms, quantum mechanics, nuclear physics, and control theory as effectively applied in the fields of mechanical and electrical engineering [84]. The Lagrange-Dirichlet theorem, a fundamental tool for the study of the stability of nonlinear dynamical systems, says that an object is in a stable equilibrium when its potential energy is at its local minimum.

A bistable mechanism is a mechanism with two stable equilibrium states/positions accessible within its range of motion. If the mechanism returns to its equilibrium position after it experiences a small forces or disturbance, the mechanism is considered to be in stable equilibrium. In other cases, when small external disturbances cause the mechanism to diverge from its equilibrium state, then the equilibrium position is unstable. The bistability theory can be illustrated with using the well-known “ball-on-the hill” analogy [85], shown in Figure 13(a). A small input applied on to the ball in position 2 or 3, shifting it from the original position by a small amount, will cause the ball to oscillate around, and eventually return to, its original position. Positions 2 and 3 are considered as stable equilibrium positions, locations where the ball has lowest potential energy.



Position 1 is an unstable equilibrium position, because if any disturbance occurs the ball is going to go to either the 2 or 3 states.

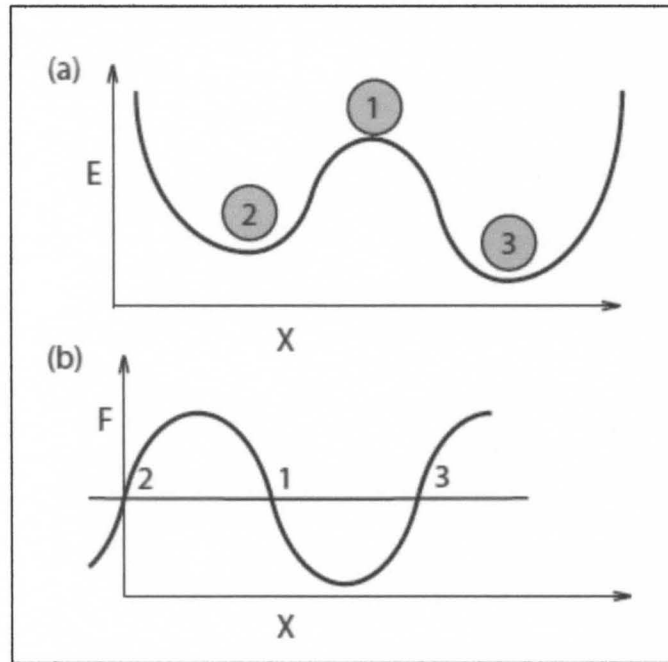


Figure 13. (a) Strain energy and (b) force-displacement diagram for bistable system. Any local minima represent stable positions.

As the ball travels from position 2 toward position 1, the force required to move the ball will increase directly as the slope of the hill increases, and force has a maximum value where its slope is greatest. Then the required force decreases until the ball is in equilibrium at position 1 (Figure 13(b)). A very small disturbance towards the direction of position 3 will then cause the ball to move rapidly or snap into stable position 3. Thus, bistable switching from one configuration to the next requires the addition of sufficient energy to jump over the small maximum and over into the other minimum (Figure 13(a)). In the absence of external energy, the switching system will be in one of the two energy

minima indicated as states 2 and 3. The shape of the strain energy curve around these points gives quantitative characteristics to the bistability.

The key advantage of a bistable mechanism is that it requires power only when changing state is needed. Input energy is not essential to sustain the mechanism in either of the stable equilibrium positions. Thus bistable MEMS are perfect for non-volatile low-power sensing or actuation applications. For these applications, small mechanical actuators are wanted to respond to energy inputs. Switching between two discrete stable states could be achieved by application of an external stimulus, such as heat [86], vibration [87], pressure [88], electrostatic or magnetic fields [89].

The shape of MEMS actuator, built using a bilayer with a stress mismatch, is determined by minimal strain energy. The top layer has tensile stress relative to the lower layer so that when the bilayer is released from the silicon substrate, it curls upward to minimize the energy stored in the strained materials.

$$\int \frac{1}{2} \varepsilon^2 E dV \quad (11)$$

Equation (11) describes the total strain energy, where  $\varepsilon$  is the local strain in the material,  $E$  is the Young's modulus, and  $dV$  is a volume increment. When the two layers have different coefficients of thermal expansion, the strain  $\varepsilon$  is affected by thermal expansion relative to the surrounding material, so it is a function of local temperature. A simple bilayer beam minimizes (11) by forming a coil of a uniform radius at a given temperature. However, a more complex structure will have several local minima in (11), each corresponding to a different folded shape. The final shape is determined by the order of folding as well as the geometric relationships between parts of the structure.

### 3.2 FINITE ELEMENT ANALYSIS USING COVENTORWARE

Finite element analysis software CoventorWare is preferred as the simulation instrument in our study due to its known unique capabilities in MEMS design, simulation, and modeling. The main design objectives in any device proposal, is to meet the prerequisite functional parameters and the reliability of the device. The functional parameters depend on the geometry, process parameters and material properties of the structure. The main difficulty that rises during analysis is the dimensions and properties used in fabrication, such as the timed release of different features from the substrate by XeF<sub>2</sub> etching, cannot be easily followed in simulation. That is why the fabrication sequence in CoventorWare is modified from the actual process to build the correct structure; in CoventorWare a temperature evolution process is applied to an already released structure that is flat at a high starting temperature.

All models were made with the same step process, starting with a blank Si wafer. SiO<sub>2</sub> is then deposited at 450 nm, followed by 200 nm of metal in a typical case. The first mask was then used to pattern both the metal and oxide to form the desire structure. Finally, a second mask was used on the Si layer to simulate the XeF<sub>2</sub> etch to detach bilayer film from Si substrate.

Once a model was defined, devices required that the thermal coefficient of expansion (TCE) is manually defined through the CoventorWare material database. The TCE of the Pt metal and silicon oxide in the simulation were set to  $9 * 10^{-6} K^{-1}$  and  $5 * 10^{-7} K^{-1}$ , respectively, with an equilibrium temperature of 1273 K. Because the metal has a higher TCE, it will change size with temperature at a faster rate than the oxide layer.

The next step is to create a mesh of the needed regions. A mesh defines the finite elements of the structure that will be used in the simulations. A Manhattan brick mesh was chosen for all devices. This kept all of the element sizes small and uniform over different geometry to give more accurate bending simulation.

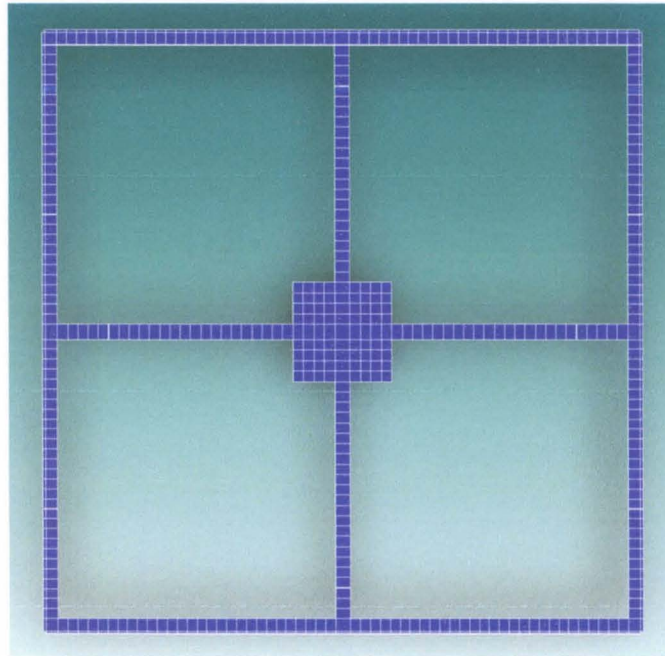


Figure 14. Meshed model of bilayer structure.

The MemMech solver, including mechanical, thermomechanical, and piezoelectric components, is used for this simulation. Non-linear, steady-state analysis options were applied. For the anchor point, the center oxide face attached to the substrate, will not be deforming and set as a reference point to work from. The parameter study analysis using CoventorWare is employed to determine the change of the displacement of a bistable structure and its shape under different thermal conditions.

### 3.3 SYMMETRICAL BISTABLE STRUCTURE

The bistable sheet structure is a strained square “windowpane” frame (Figure 15). Dimensions of the simulated bistable structure are  $600\ \mu\text{m} \times 600\ \mu\text{m}$  with metal traces of width  $15\ \mu\text{m}$ . The bilayer is thermally grown silicon oxide layer and Ti/Pt metal film.

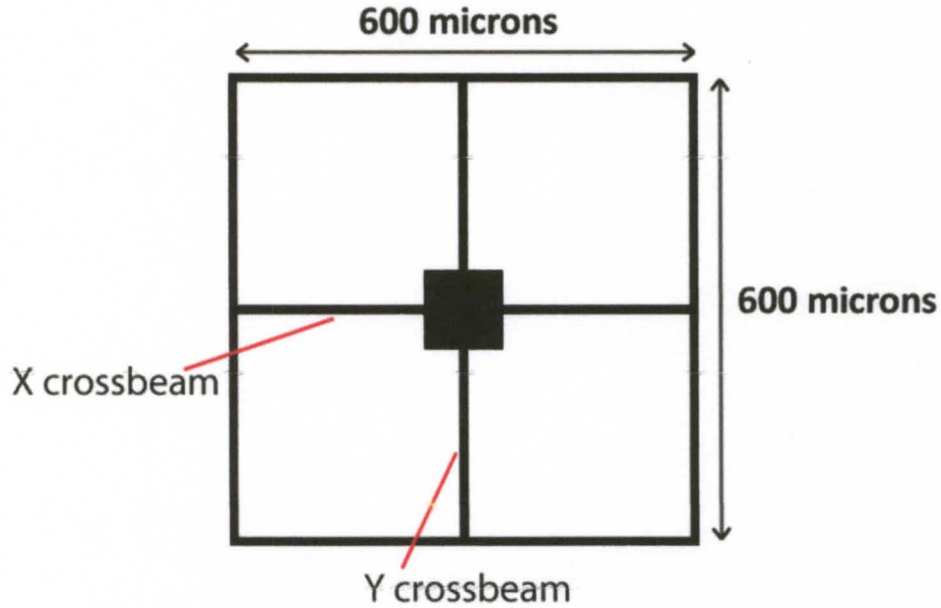


Figure 15. Layout of symmetrical bistable structure.

Simulations demonstrate that the “windowpane” has two stable states achieved by applying a targeted thermal stress to the structure. Volume boundary conditions for temperature were evolved from 250 K to 450 K along the X crossbeam, and 450 K to 250 K along Y crossbeam, that cause a simulated structure to experience shape deformation. Its stored strain energy can be minimized by curling along one of axis - X crossbeam (Figure 16(a)). Another local energy minimum state is accessible by curling along the other axis –Y crossbeam (Figure 16(c)). It takes some energy to switch from either of these local minima, through the short-lived transition state (Figure 16(b)),

to the other. As shown in Figure 16(a)-(c), the center of the MEMS device need not move during operation, so devices, attached to the substrate at the center, are capable of bistable actuation and both bistable states are equivalent.

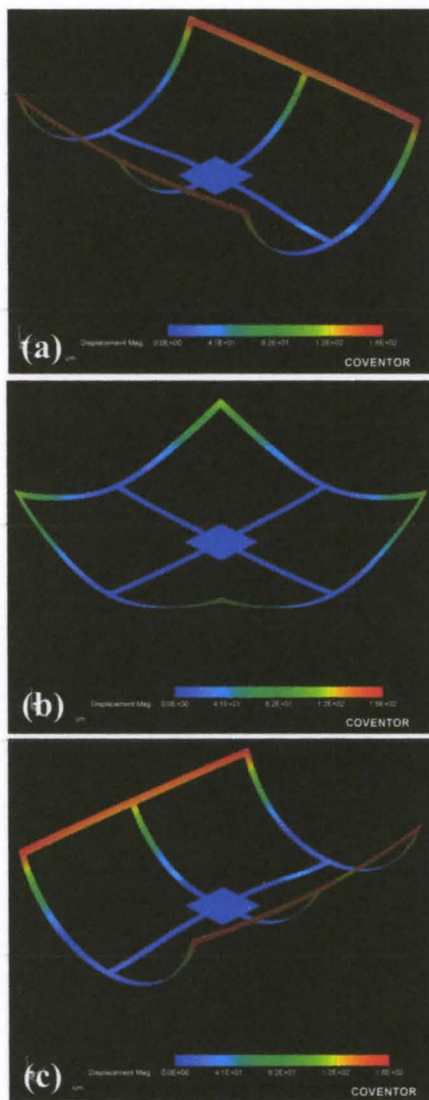


Figure 16. CoventorWare simulation of “windowpane” shape symmetrical bistable structure by controlling the temperature of the crossbeams.

When temperature conditions along two side beams were evolved from 250 K to 450 K, and 450 K to 250 K along the opposite side beams, it as well caused a simulated structure to experience shape deformation. However, the short - lived transition state during switching from one of these local minima states to another was not observe (Figure 17).

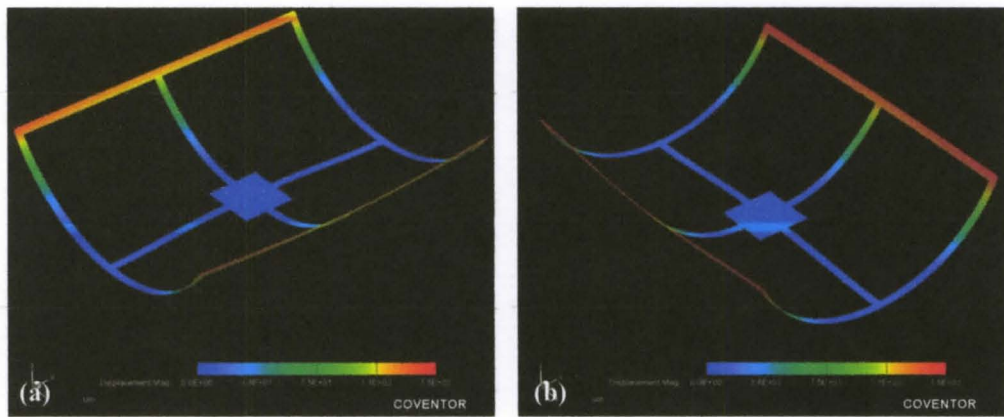


Figure 17. CoventorWare simulation of “windowpane” shape symmetrical bistable structure by controlling the temperature of the sidebeams

Finite element analysis also gives information about Mises stress - measure of the shear, or distortional, stress in the material [90]. This type of stress is used to predict yielding of materials under any loading condition from results of simple uniaxial tensile tests. The Mises stress comply with the property that two stress states with equal distortion energy have equal von Mises stress (Figure 18).

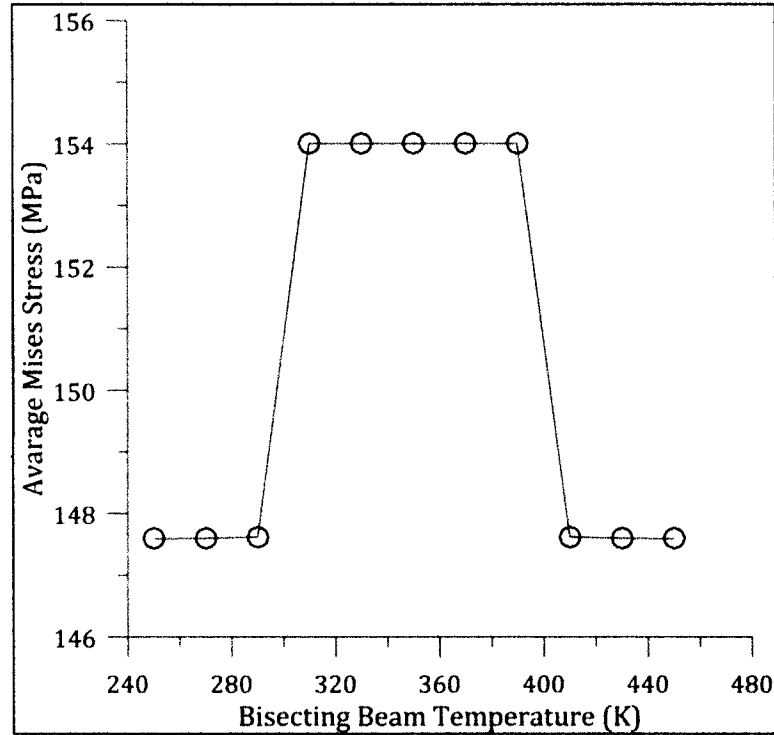


Figure 18. Calculated average Mises stress in the entire volume.

Evaluation using electron microscopy show bistable behavior as predicted with finite element analysis. Two local minima are observed that correspond to two mirror image stable states when structure is released. The center unstable state does not occur in fabricated devices because of random imperfections that bias it toward one of the two stable states. The device has an arbitrary initial state and as expected will fold into one of the stable states after releasing. It has been observed that about 70-75% of devices will come to in one state, while the others are opposite due to random fluctuations in feature widths and local etch rates (Figure 19). Due to manual state switching by probe station, the structures remain in the state in which they were retained.



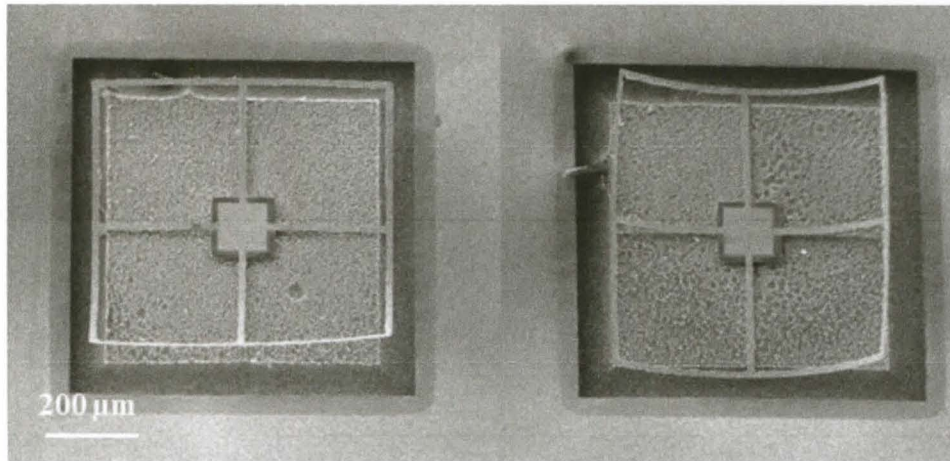


Figure 19. SEM image of fabricated structures, according to process discussed in Chapter II (Figure 3), released in both possible bistable states.

### 3.4 ASYMMETRICAL BISTABLE STRUCTURE

Similar simulations were performed for asymmetrical bistable structures with dimensions of  $400 \mu\text{m} \times 600 \mu\text{m}$  and metal traces of width  $15 \mu\text{m}$ . (Figure 20). Asymmetrical geometry of devices assumes bistability with one prevailing stable state.

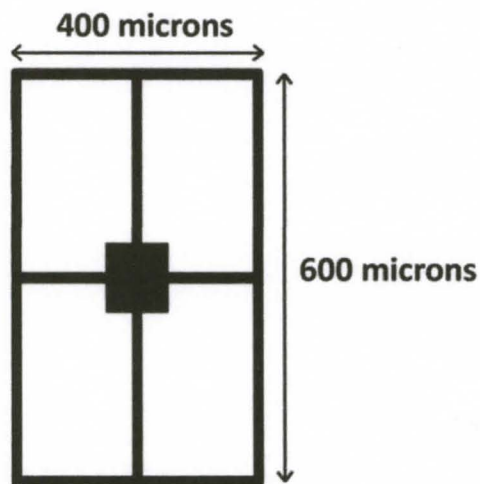


Figure 20. Layout of ssymmetrical bistable structure.

CoventorWare simulations show that the rectangular “windowpane” will curl along its longest predominant axis based on the principle of minimizing stored strain energy (Figure 21(a)). Another local energy minimum state, having higher energy than the long-axis state, is accessible by curling along the shorter axis (Figure 21(c)). The short-lived transition state is not symmetrical along a central beam (Figure 21(b)).

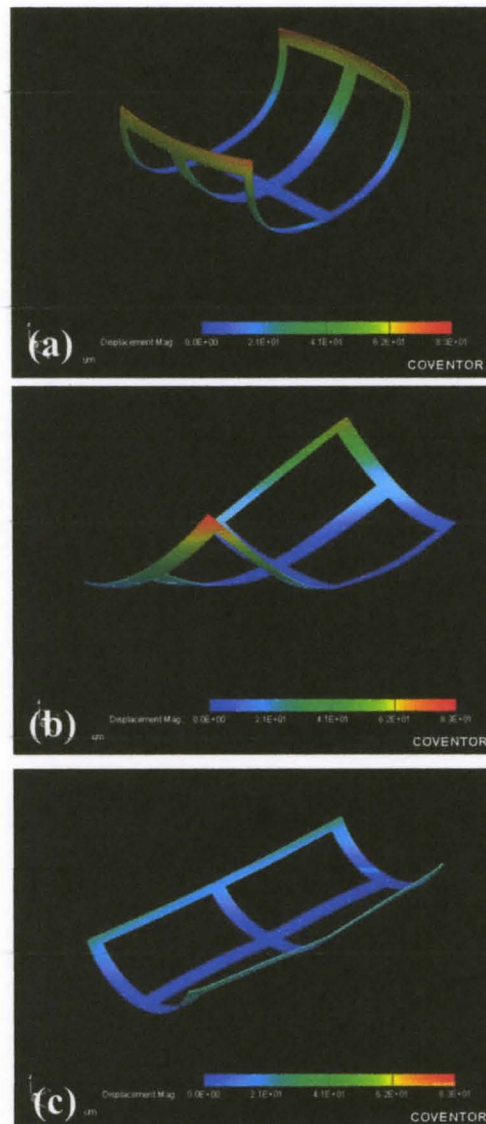


Figure 21. CoventorWare simulation of asymmetrical bistable structure.

Scanning electron microscopy shows different designs of released asymmetrical bistable structures at principal initial orientations (Figure 22).

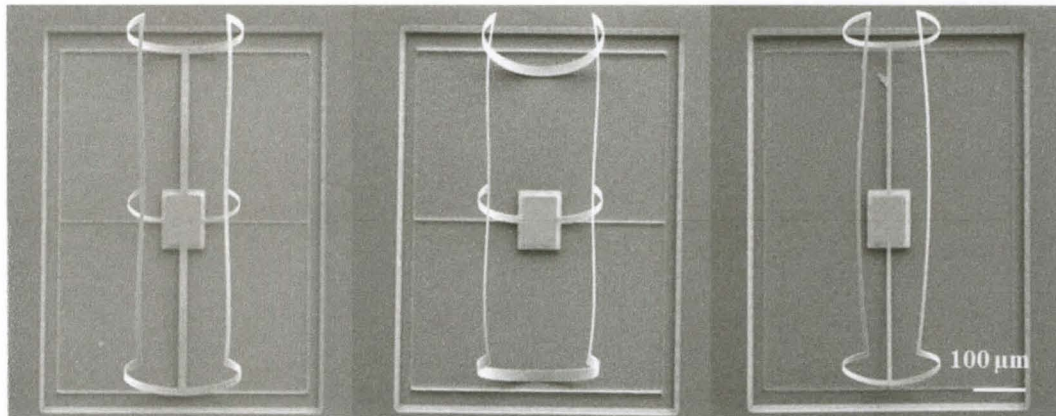


Figure 22. SEM image of three different designs of released asymmetrical bistable structures at predominant initial orientations.

### 3.5 SERPENTINE ASYMMETRICAL STRUCTURE

Another type of asymmetric bistable structure, based on a serpentine design where two cantilevers are coupled at the tips by a thin-film bar, has been discussed. Even though the planar layout is symmetric (Figure 23), a symmetric released shape is not the state with the lowest total strain energy. Due to the balancing of tensions between the strained cantilevers, there are two mirror image stable states after it released. The devices have a random initial state of left or right arrangement defined by accidental fluctuations during fabrication process [86].

A numerical model was developed in CoventorWare to calculate the configuration of the coupled actuators as a function of temperature. The metal and oxide material properties and dimensions were incorporated into a Manhattan brick mesh having

rectangular elements. Deflection was observed as temperature was varied for elements in the right or left actuator, with a temperature gradient calculated along the coupling bar.

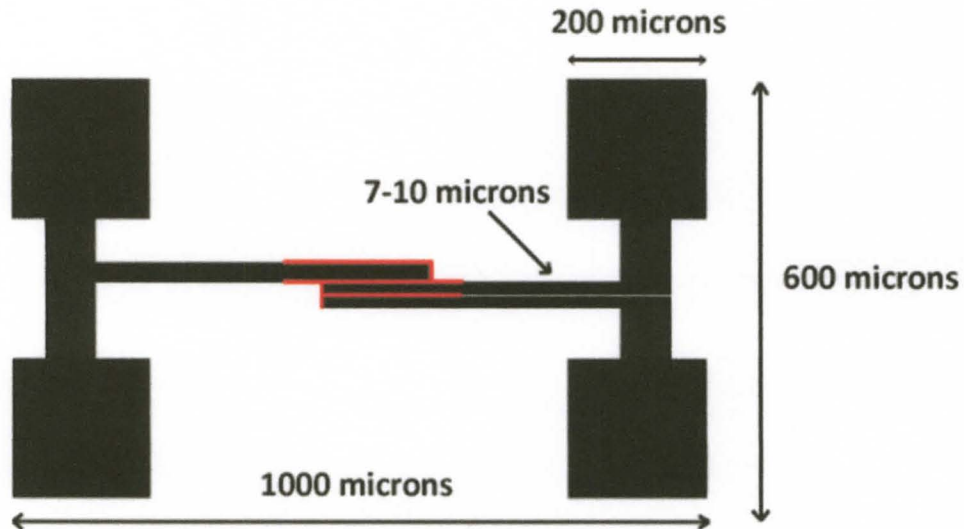


Figure 23. Layout of bistable device showing two U-shaped cantilevers with their contact pads and joined by a cross-bar at the tips.

The resulting model captured the bistable nature of serpentine structure illustrated in Figure 24. For the bistable devices, there is no configuration that allows all parts of the released device to attain the lowest energy radius of curvature given in Equation (1), which applies only to unconstrained cantilevers. In this case, some parts of the structure contain strain energy that can flip the device suddenly from one state to the other when pushed close to the threshold by thermal or external actuation.

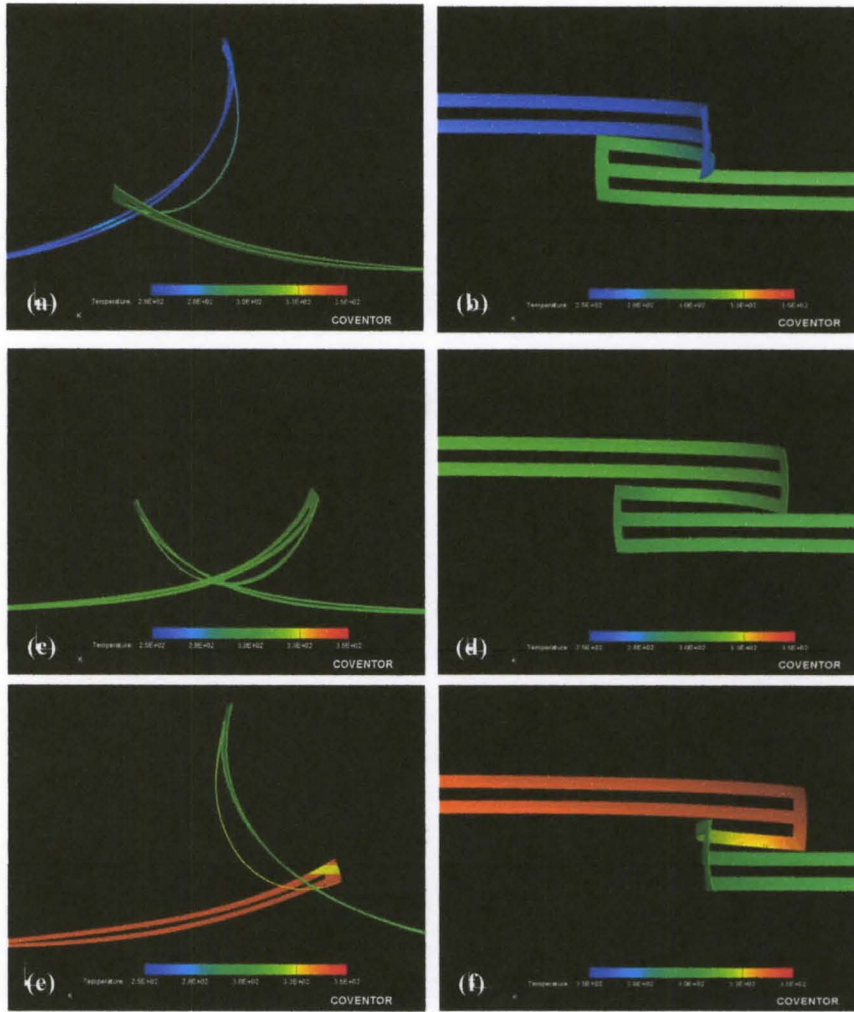


Figure 24. CoventorWare simulation of asymmetrical bistable structures (a) rear actuator at 280K, front actuator at 300K, (b) side view, (c) both actuators at 300K, (d) side view, (e) rear actuator at 340K, front actuator at 300K, (f) side view.

The higher of the two cantilevers can be thermally actuated to tip the balance past its threshold and into the opposite configuration. Thermal actuation of the left actuator would flatten the left side while allowing the right side to curl. The change from the left to the right orientation occurs when the balance of forces shifts the configuration past a higher energy intermediate state. It is important to mention that fabricated structures did stay put on the left or right after actuation for at least 1000 cycles (Figure 25).

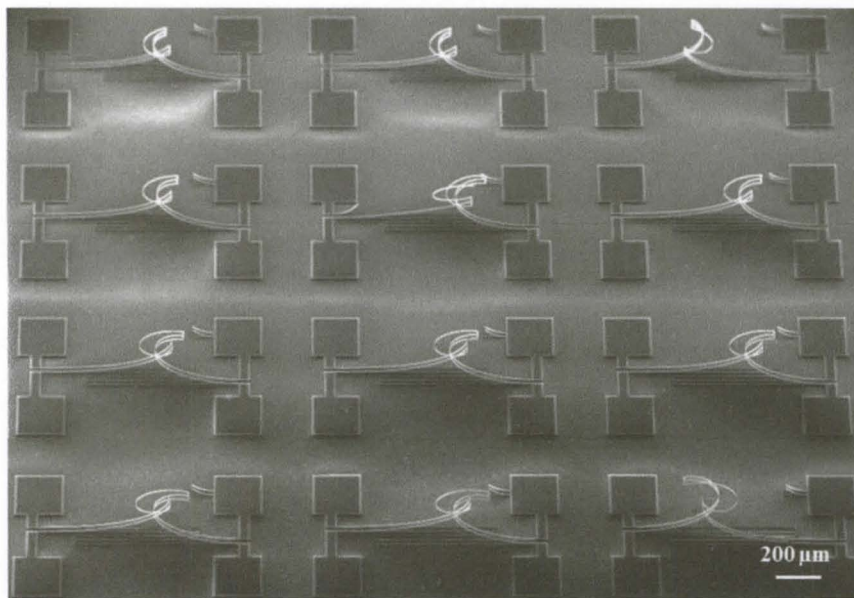


Figure 25. Electron micrographs of a wide field of Cr/Ni/Cr asymmetric released devices having different initial orientations.

### 3.6 CONCLUSION

A numerical model was developed in CoventorWare to analyze the configuration of the windowpane as a function of temperature. The steps in the simulation were to describe a fabrication sequence that would create the desired material structure, set the material properties needed to produce the stress mismatch, and to choose the simulation parameters to get an applicable result that matches the experimental result. Simulation has shown that both symmetrical and asymmetrical devices display bistability and have two stable states, which can be changed by selectively applying heating to critical regions of the structure. The transformation from the one orientation to other occurs when the balance of forces shifts the configuration past a higher energy intermediate state.

It been shown experimentally that devices, fabricated from bilayer films with a non-uniform stress, have two stable states when released due to the balance of tensions in strained bilayer and they an arbitrary initial state defined by random fluctuations. Devices are unable to remain in an unstable state, so switching speed is rapid once the energy threshold is reached.

Applications in biological research are under development to make use of this structure. Future simulations will allow adjusting the dimensions of the MEMS devices so the energy barrier can be crossed at temperatures compatible with physiological conditions.

Serpentine asymmetric structures are most likely to apply to small-current programmable electrical interconnects, optical switches, and smart antenna elements. For example, the device could be used as an actuator mechanism for a reconfigurable terahertz frequency range metamaterial that has been previously shown using passive

bimaterial out-of plane pivots made with similar dimensions and materials [22]. These applications have the common features of low required actuation force, limited available power for reconfigurable devices that must compete with existing passive devices, little space available for new circuitry beyond the actuator itself, and the need for large deflections.



## CHAPTER IV

### LIGHT-POWERED HYBRID MICROACTUATORS

#### 4.1 LIGHT DRIVEN MICROSYSTEMS/MICRODEVICES

The phenomenon in which light energy is converted into mechanical deformation to generate displacements at the micro- and nanometer scale has brought an increased interest in optical actuation effects in MEMS devices, microfluidics and biotechnology, polymeric materials and composite application. Energy and signal transmission using light also permits researchers to design wirelessly and avoid some of the problems associated with electrical noise and/or thermal conduction related to wires. The driving method can be controlled remotely by manipulating the wavelength and other radiation conditions. Research and development into photomechanical effects will offer a new potential foundation for smart structures and advanced technologies.

A large variety of effects can happen when light interacts with an absorption surface. Depending on the nature of these interactions, there are a few types of mechanisms for optical actuation: photoelectric, photothermal, photochemical and photoacoustic (Figure 26).

Photoelectric actuation translates a range of wavelengths and radiation intensities into electrical power. The photoelectric effect generates the photoelectrons in semiconductor (silicon *p-i-n*, photovoltaic *p-n* junction) and organic materials to fabricate

solar cells [91], [92], [93], photodetectors [94], and is widely used to create photocurrent in piezoelectric material [95], [96].

The photoacoustic effect is a conversion between photonic energy to acoustic energy due to absorption and localized thermal excitation. Applying rapid pulses of light to polymer film causes a rapid thermal expansion which generates ultrasonic thermoelastic waves due to pressure variation in the surrounding medium. This effect allows implementing electrically passive, miniature flexible optical fiber photoacoustic–photothermal probes for biomedical applications [97], as well as MEMS scale photoacoustic sensors for the detection of trace gases [98].

The photochemical mechanism is most typically used with polymeric materials and composites. Light-driven actuation in liquid-crystal polymers and polymeric materials can be gained through the adding the photochromic (azobenzene or spiropyran) molecules. Those molecules are able to go through a reversible photochemical reaction in response to light irradiation that causes the polymeric matrix to bend along any chosen direction, and allows creation of light-driven microstructures: actuators [99], plastic motors [100], and photoswitches [101].

Another important optical actuation technique is an optical trapping and manipulation of particles that provide unique control the dynamics of small particles when a tightly focused beam of light capable of holding microscopic particles stable in three dimensions [102], [103].

The primary universal mechanism for optical actuation is achieved by the photothermal effect (or absorptive heating) which employs the conversion of the light energy into the thermal energy. Using light as a method of energy transport is very

beneficial for micropumps based on bimetal membranes [104], proton pumps based on a microcantilever interfaced with bacteriorhodopsin film [105], or driving micromachines by adjusting a laser beam on a movable micro component for biotechnology [106].

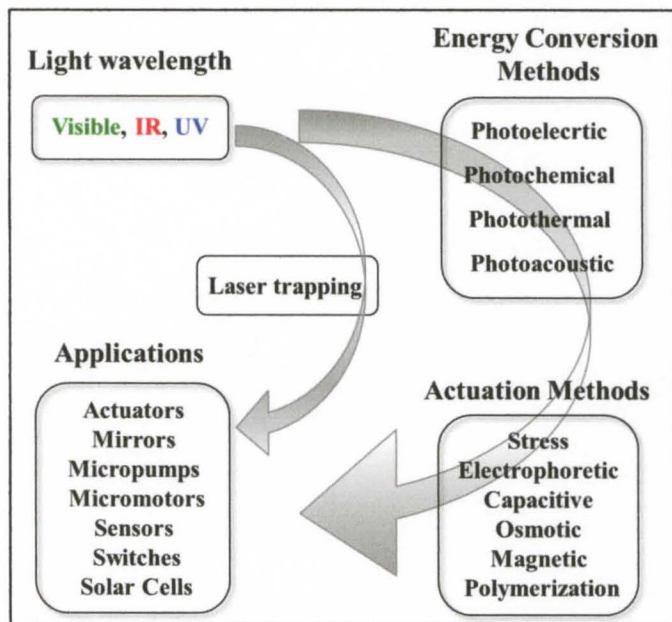


Figure 26. Diagram represents mechanisms of light energy conversion, actuation methods and applications for light-driven microstructures.

The photothermal effect is successfully used for fast, inexpensive and non-photolithographic creation of microfluidic microchannels for mixing fluids and moving cells by utilizing the shrinkage properties of pre-strained polystyrene sheets (also known as Shrinky Dinks<sup>®</sup>) [107]. Another property of Shrinky Dinks is useful to form self-assembled 3D shapes from a flat 2D patterns, by exposing them to infrared light. Under infrared light irradiation, printed black lines absorb more energy than the rest of the polystyrene sheet. It causes the plastic below the printed lines to contract and act like hinges that are activated by light [108]. All those mechanisms can cause the

photomechanical actuation, when exposure to light can triggers changes in the internal state of the structure (such as shape or volume), and lead to a mechanical response.

## **4.2 NANOMATERIALS PREPARATION METHODS**

In the previously mentioned systems, nanomaterials are often involved in the transduction of light energy into chemical, electrical, thermal or mechanical energy. Their high specific surface area provides plentiful sites for catalysis or injection of charge carriers, and effects unique to the nanoscale, such as resonant infrared absorprtion, are available to convert light into other forms of energy. There are different types of nanomaterials such as nanowires, nanotubes, and nanoparticles, which can be prepared through different methods. In general, there are three generic procedures to prepare nanostructures: wet chemical and physical and gas phase synthesis [109].

Wet chemical processes contain colloidal chemistry, phase transfer synthesis, hydrothermal methods, sonochemical methods, sol–gel, and other precipitation processes. These procedures offer the fabrication of a large assortment of compounds (organic, inorganic, and some metals) and the ability to control particle size with high monodispersity. Colloidal chemistry and phase transfer methods are generally employed to synthesize metallic Au/Ag nanoparticles with different shapes such as nanoparticles [110], [111], nanorods [112], nanowires [113], metallic core–shell nanoparticles [114], nanoplates [115], [116], nanoprisms, and semiconductor nanoparticles (CdSe, tungsten sulfide, and others) [117].

Physical techniques, such as grinding, milling, and mechanical alloying, are widely used for the synthesis of inorganic and metallic nanoparticles. Those techniques

are simple, require low cost equipment, and provide coarse powders. In the case of carbon nanotubes, physical techniques include vacuum deposition processes, chemical vapor deposition (CVD), and spray coating based on the catalytic decomposition of hydrocarbons.

Gas phase synthesis methods including pyrolysis [118], [119], laser ablation [120], [121] and plasma synthesis [122], [123] have been used for the synthesis of nanoparticles. Flame pyrolysis has been used for the fabrication of materials such as fumed silica particles [124], carbon black, and carbon nanotubes [125]. The presence of transition metal particles is essential for the formation of nanotubes in the pyrolysis process. Laser ablation techniques can be used to prepare almost any nanomaterials [126].

This work will focus on colloidal chemistry and phase transfer methods to synthesize gold nanoparticles, as well as chemical vapor deposition technique to synthesize carbon nanotubes, with the goal of integrating the nanomaterials with microelectromechanical structures.

### 4.3 DEPOSITION OF NANOSTRUCTURES BY CHEMICAL VAPOR

#### DEPOSITION

Chemical vapor deposition (CVD) is widely used technique to produce high quality, purity and performance solid materials. The process is frequently used in the semiconductor industry to produce thin films. Also, it has been successfully employed for growth of various nanostructures – carbon nanotubes [127] and nanofibers [128], nanowires [129], [130], graphene [131] and other carbon structures. The carbon CVD growth process involves heating a catalyst material to high temperature (500-1000°C) in a tube furnace, and flowing hydrocarbon gas through tube reactor over a period of time. The general nanotube CVD growth mechanism includes the dissociation of hydrocarbon molecules catalyzed by the transition metal (most commonly a transition metal, like nickel, cobalt, or iron), and dissolution and saturation of carbon atoms in the metal nanoparticle. The precipitation of carbon from the saturated metal particle leads to the formation of tubular carbon solids in a  $sp^2$  structure.

Bistable structures made from the metal/oxide bilayer (Ti/Pt/SiO<sub>2</sub> or Ti/NiTi/SiO<sub>2</sub>) were used as a substrate for CNT growth by CVD technique. Fabrication details are described in Chapter II, Section 2.5. The single wall CNTs were synthesized from methane (CH<sub>4</sub>) and iron-based catalyst solution [132]. Catalyst solution contains 3.3 mg of Fe(NO<sub>3</sub>)<sub>3</sub> (Sigma-Aldrich, St. Louis, MO, USA) dissolved in 20 ml of isopropanol. The substrate was immersed in catalyst solution for 10 seconds followed by dipping in n-hexane for the same time in order to improve catalyst particle adhesion to the MEMS device surface. The synthesis process used for the CNTs has two steps: reduction and reaction. The CVD reactor, shown in Figure 27, was heated up to 860°C

while a “carrier” gas, He/H<sub>2</sub> was introduced at flow rate of 100 sccm. The catalyst was oxidized by heating the dip-coated substrate in He/H<sub>2</sub> mixture at 500 °C, and then reduced in a flowing Ar/H<sub>2</sub> mixture (3% H<sub>2</sub>) during heating of the CVD chamber. The reduction step is essential for CNT synthesis; it reduces initially oxidized metal and facilitates surface mobility of metal atoms and clusters.

Once the temperature was stabilized at 860°C, the Ar/H<sub>2</sub> mixture was stopped and CH<sub>4</sub> was introduced at a flow rate of 450 sccm to initiate single walled carbon nanotubes (SWNT) growth. The reactor was left running for ~5 minutes at atmospheric pressure. Finally, methane gas was turned off and switched back to Ar/H<sub>2</sub> atmosphere at 100 sccm and the system was cooled down to room temperature.

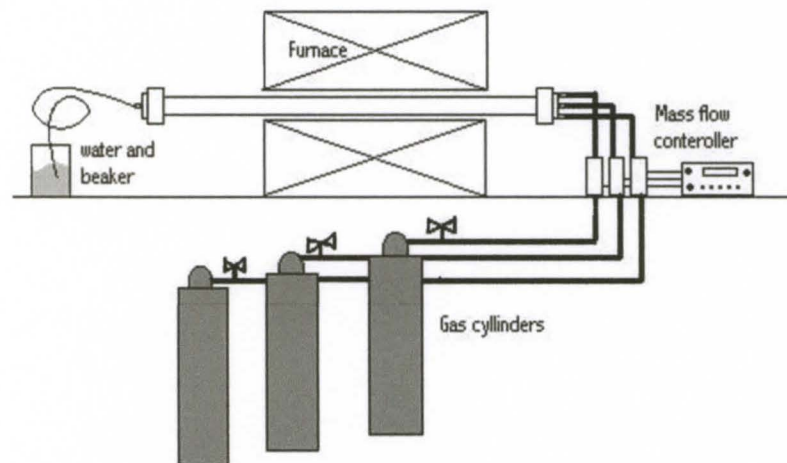


Figure 27. Schematic diagram of CVD reactor.

Figures 28-29 illustrate SEM images of the web-like network of single wall nanotubes covering the catalyst surface, both metal and oxide surfaces, of prior released MEMS devices. Similar results were obtained with both types of metal used in fabrication of MEMS bistable structures.

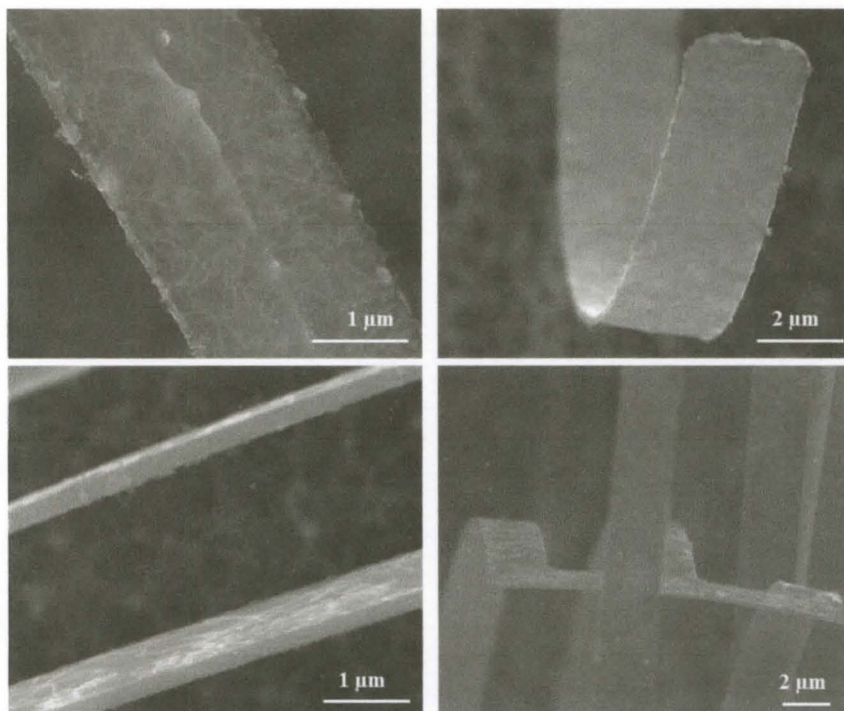


Figure 28. CVD-grown single-walled carbon nanotubes on Cr/Ni/Cr bilayer structure.

As seen in Figure 28 SWNTs are extending to, and lying on, the surface that supports the catalyst particles, as well as, in a few instances, growing away from the surfaces.

Raman spectra have been collected on synthesized nanostructures, and it confirms that grown carbon nanotubes are single-walled (Figure 30). A typical Raman spectrum of the SWNTs obtained using the 1064 nm excitation wavelength exhibits G - band at  $1597\text{ cm}^{-1}$  (tangential band). The position and the line shape of this band have been used extensively to determine the SWNT diameter distribution and semiconducting/metallic nature of SWNTs. Diameters of single walled CNTs are in range from 5 to 20 nm. The intensities of other Raman peaks like radial breathing mode, disorder induced D - band and the G' - band are small compared with background signal.



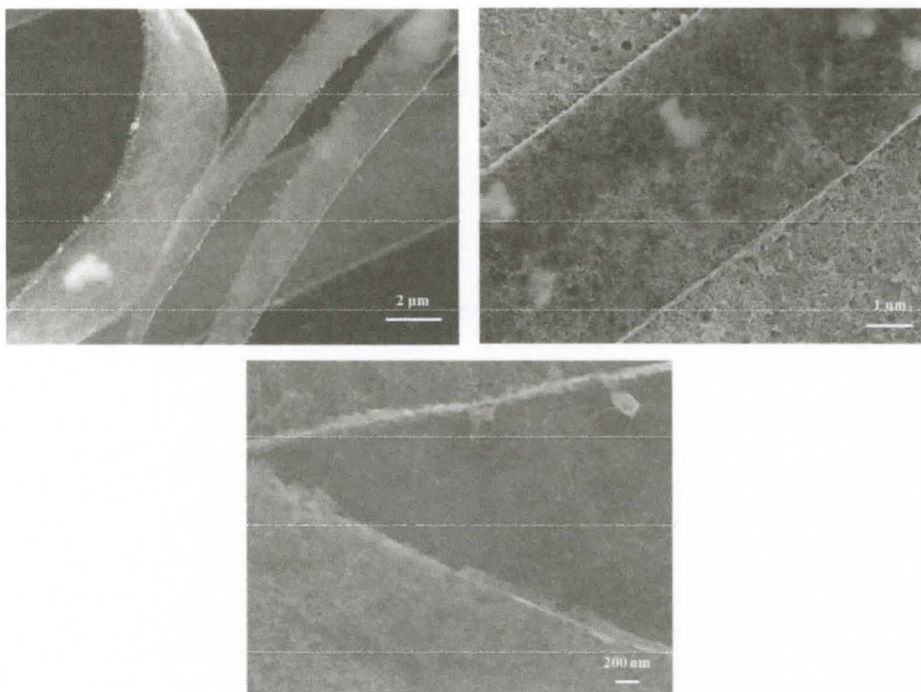


Figure 29. CVD-grown single-walled carbon nanotubes on Ti/Pt bistable structure.

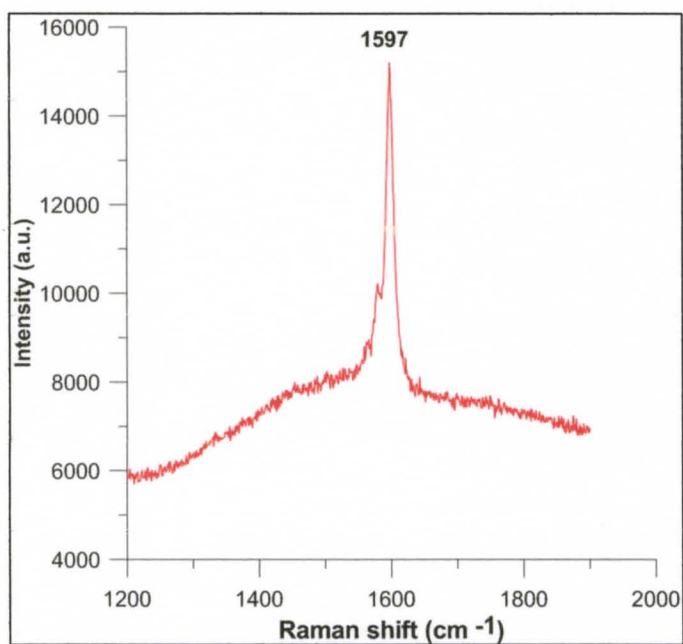


Figure 30. Raman spectra of synthesized SWCNTs.

The surface deposition method of nanomaterials on MEMS devices was achieved by the chemical vapor deposition technique presented above. The biocompatibility and unique optical, electrical, mechanical and thermal properties of carbon nanotubes offer a basis for applications in nanometer-scaled electronic devices. Fabricated MEMS devices with grown SWNTs can be used as extremely small sensors responsive to their chemical and mechanical environments. Also, they can be utilized to obtain tunable uniform elastic deformation of SWNTs, which may act as the model for the study about the effect of delocalized bending on the properties of SWNTs. Carbon nanotubes are also known for their tunable near-infrared emission that modulates in response to the adsorption of specific biomolecules [133].

## 4.4 DEPOSITION OF NANOSTRUCTURES BY DIMATIX INKJET

### PRINTER

The controlled deposition of functional materials such as proteins, cells, antibodies, polymers required for cell based biosensors, tissue engineering, or antimicrobial devices has recently gained attention as the demand for multifunctional biological devices has increased. Deposition methods, such as chemical vapor deposition and solid free-form fabrication, have effectively reproduced the nanometer scale deposition of semiconducting materials required for the rapid prototyping in industrial device manufacturing. On the other hand, their high temperature reaction environments and time consuming procedures are unsuitable for functional material deposition. The capability of piezoelectric inkjet printing as a rapid prototyping technique can be used for microscale deposition of functional composite materials.

The Dimatix DMP system (FujiFilm Dimatix) [134] is a piezoelectric inkjet printer with refillable cartridges used for printing user-defined materials. The cartridges are MEMS-based, with 16 nozzles (20  $\mu\text{m}$  in diameter) spaced at 254  $\mu\text{m}$ , each dispensing a droplet volume of 1–10  $\mu\text{L}$ . The printer has an ability to accurately dispense small volumes of material per drop with high resolution  $\pm 5 \mu\text{m}$  and feature sizes currently down to 25  $\mu\text{m}$ . Also, a waveform editor, heated theta platen and a drop-watch camera system allow to control of the electronic pulses to the piezojetting device for optimization of the drop characteristics as it is ejected from the nozzle.

The printer is suitable to print fluids containing proteins [135], [136], nucleic acids, like DNA [137], [138], nanoparticles [139], nanotubes [140], [141], conductive polymers [142], etc.

A few different biocompatible solutions that based on Pluronic® F-127 (PF-127) hydrogel and Polyvinylpyrrolidone (PVP) polymer have been printed. Pluronic® F-127 is a hydrophilic nonionic surfactant, known as poloxamer. It has been widely used in cosmetics, medicine and bioapplications. The ability of PF-127 hydrogel to solidify at the physiological temperature of 37°C, after jetting as a liquid at a lower temperature, helps enables enzymes, cells, physiological buffers and other biomaterials to be formulated in aqueous media for printing, and then become semisolid to protect the biomaterials and keep them concentrated at locations in the human body. PVP is a water soluble polymer with good wetting properties and easily forms films that make it good for coating applications.

Both Pluronic® F-127 and PVP were purchased from Sigma–Aldrich. Aqueous solutions were created using deionized distilled water. Solution A is a synthesized gold nanoparticles suspended in water; the details of synthesis process will be discussed in Appendix. Solution B includes synthesized gold nanoparticles that are suspended in water with 3% PVP solution. Solution C consists of 2% PF-127 hydrogel with 0.1 µl of gold nanoparticle suspension (Appendix).

Figure 31 and 32 show an interesting feature of a drying droplet of a nanoparticle colloidal solution is known as the “coffee stain” effect, when significant lateral flow from the center to the edge while the film dries. And after the droplet completely dries out, it leaves a dense ring-like stain of nanoparticles which decreases in concentration from the periphery inwards [143], [144]. Also agglomeration and the formation of larger particle clusters were observed for solution A (Figure 31).

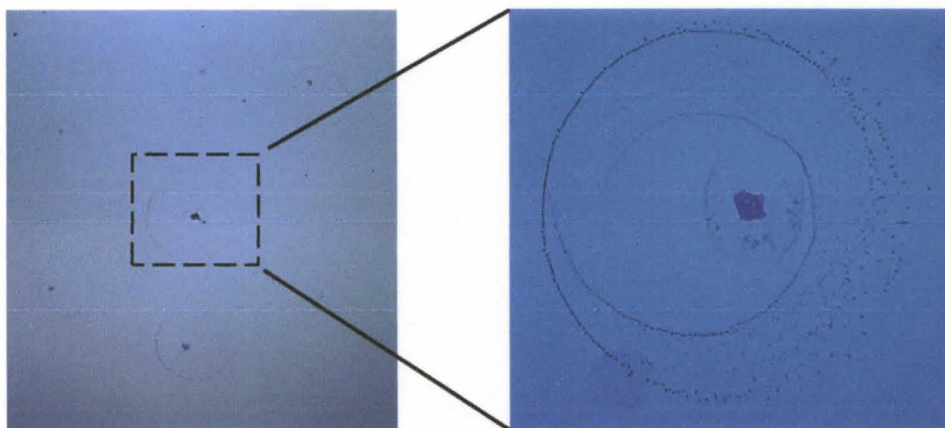


Figure 31. Optical image of ink jet-deposited nanoparticle (solution A) in a dot array pattern on the glass slide.

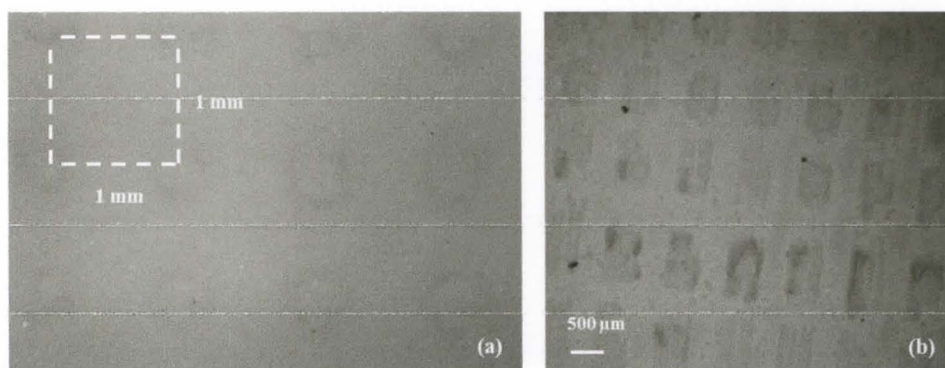


Figure 32. Optical image of printed array patterns using (a) solution B, (b) solution C on the glass slide.

The above method of deposition of nanostructures by the Dimatix inkjet printer has a lot of advantages: capability of jetting a wide range of fluids (water-based, solvent, acid or base) on substrates with thickness of 0.5 - 25 mm, allowing variable jetting resolution and substrate alignment. But this method also has a few restrictions: viscosity of the fluid should be between 10-12 cPs and surface tension of the fluid should be

between 28 and 33 dynes/cm<sup>2</sup>. Any particles in the fluid should be less than 0.2 μm in size, and the fluid should not be too volatile. Eventually, the particles in the all three solutions form agglomerates (within a few days) that will subsequently cause blocking of the printing head.

#### **4.5 DEPOSITION OF NANOSTRUCTURES BY MICROSTENCILING TECHNIQUE**

Stenciling is a versatile method that covers specific regions of a substrate for patterning different kind of materials. It is a widely used process in electronics industry for patterning of adhesives, insulators and conductive materials, that are utilized in a various applications, such as patterning of printed circuit board features, interconnect technologies, and advanced packaging technologies.

A growth in interest toward the development of nonsemiconductor based microsystems and MEMS devices motivates a development of the microstenciling technology that implements micron scale stenciled features on conventional microelectronics substrates (silicon, glass) as well as unconventional microelectronics substrates (various plastics, flexible materials). Microstenciling allows depositing much wider ranges of materials: metals, various chemically sensitive polymers, and biological materials (cells and proteins).

Using this technique enables patterning of vapor-deposited films and sputtered thin metal films onto materials (e.g. thermoplastics and metal oxides) without the need for conventional photolithography and wet etching of metals with minimum surface contamination by organic residues from the fabrication process [145], [146]. A laser

micromachining method can be used to pattern arrays of microchannels and microholes in Kapton® and PDMS films [147]. This method utilizes a silicon wafer, etched through the total thickness, as stencil. The etched pattern in the silicon microstencil defines the areas through which the desired thin film materials are to be deposited onto an underlying substrate. Also, a laser-machining approach was applied for the rapid fabrication of 50 µm PDMS elastomeric microstencils to control the placement of protein and cells for immediate use in cell culture experiments [148]. PDMS microstencils can be a good alternative to microcontact printing, when PDMS elastomeric stamps are used to transfer biological material to the substrates. But PDMS tends to shrink upon curing and swell when in contact with nonpolar solvents, and experiences pairing and sagging [149] of the stamp, evolving from the elastomeric properties of PDMS.

Parylene C (poly (monochloro-p-xylylene)) is a member of a unique family of thermoplastic, crystalline polymers. It is another material that has been used as stencil material [150], [151] It has found wide recognition as biocompatible polymer and brings about many interesting possibilities in MEMS [152], mostly in microfluidic and bioMEMS applications [153], and medical industries [154]. Parylene films are transparent, conformal, uniform, low defect density, chemically inert due to low temperature vapor deposition polymerization coating process, and allow multi-layer processing to produce complex structures and features [153]. Also, Parylene C provides good electrical insulation properties and shows high long-term stability in the physiological environment [154].

Defining small features in deposited Parylene C films is achieved by a combination of photolithography and dry etching techniques, such as plasma etching,

reactive ion etching (RIE), and deep reactive ion etching (DRIE) based methods. These techniques also have an ability to create the high aspect ratio structures that are desired for various MEMS applications.

To fabricate the flexible microstencil for nanoparticle patterning on the top of MEMS devices, Parylene C was used to vapor deposit a 3-8  $\mu\text{m}$  thick conformal film on a prefabricated planar MEMS (PDS 2010, Labcoater 2, Specialty Coating Systems). Then, photolithography was performed to define the stencil regions. Hexamethyldisilazane (HMDS) was spun at 4000 RPM for 10 seconds to achieve good adhesion between the Parylene C and the photoresist film. Right after, SPR - 220 positive photoresist was spun at 1500 RPM for 30 seconds, and a 6  $\mu\text{m}$  photoresist film was used as masking layer. Depending on the desired thickness of masking layer, the spinning parameter can be varied; if a thicker film is desired, 1000 RPM can achieve a 15  $\mu\text{m}$  film thickness. The wafers were soft baked on a hotplate at 115°C for 5 minutes. Photoresist was exposed with Karl Suss MA6 contact aligner for 30 seconds (or 60 seconds for thicker resist) and then, at least a 30 minute wait prior to performing the post exposure bake and developing. This “hold time” is crucial, as it allows the photo active compound to breakdown in the relatively thick resist. Resist was developed in a MF 319 developer solution for 2-4 minutes, duration of the development will vary depending on the density and the smallest feature size of the pattern.

After patterning the resist/mask, the uncovered Parylene C areas are etched away in March CS-1701 RIE plasma system at power of 250 W and pressure of 250 Torr in oxygen environment at 20 sccm for 10-20 min, depending on Parylene film thickness. Rinsing with acetone helps to dissolve the residual photoresist. This is followed by an



isopropyl alcohol and deionized water rinse, and finally the wafer is dried with nitrogen. After dicing the wafers, they are ready to be coated with various solutions and Parylene C stencil can be peeled off the surface to form the desired chemical pattern.

A deposited Parylene C layer has a hydrophobic surface, but O<sub>2</sub> plasma treatment for a minute or less turns the surface hydrophilic, and it stays hydrophilic for a few days. The hydrophobic Parylene C surface seals extremely well to other hydrophobic surfaces, moreover, the hydrophilic surface does not adhere well to other surfaces, a property that is important while using the Parylene C as a shadow mask.

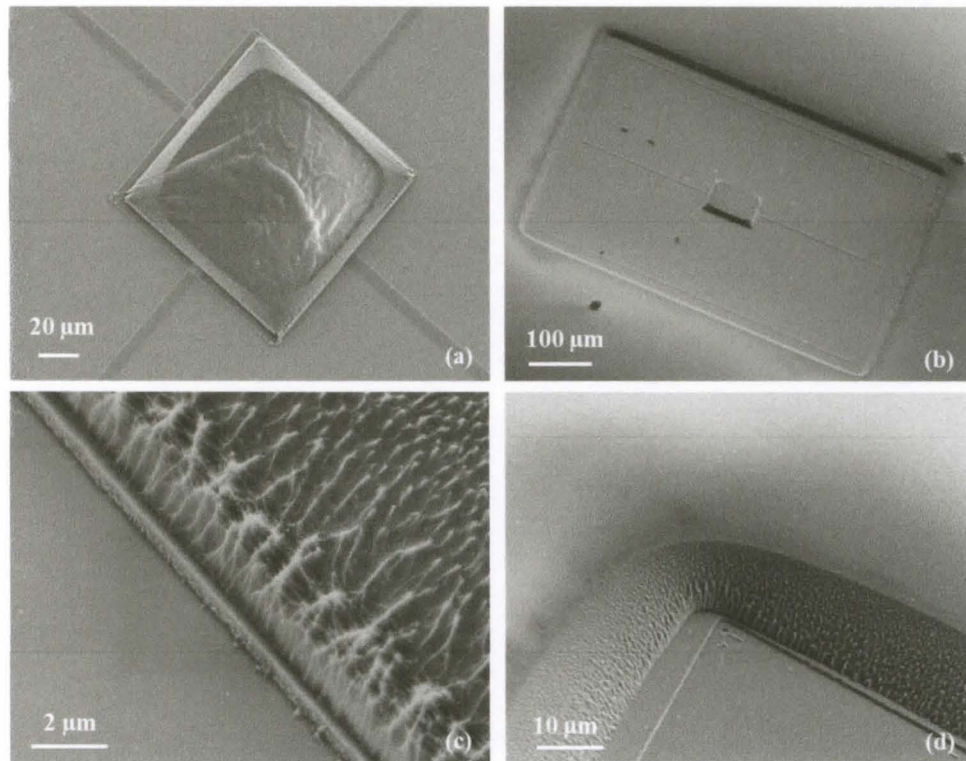


Figure 33. Scanning electron microscopy of microstencils.

Fabrication of the Parylene C microstencil mask with large feature dimensions more than 500 μm is achieved, but there is lateral etching observed during RIE processing (Figure 33 (d)). Anisotropic etching profile of sidewalls are nearly vertical

due to the fact that SPR-220 photoresist is used as masking layer and undergoes the etching too. That causes the increasing of stencil size by 2-3  $\mu\text{m}$  in each direction, but it does not have a negative effect for our application.

Figure 34 shows different fabricated microstencil before patterning. The dark contour defines the area of microstencil. Fabrication of stencils with fine features of 10  $\mu\text{m}$  and less (Figure 34 (d)) requires the most anisotropic etch and adjusting the size parameters.

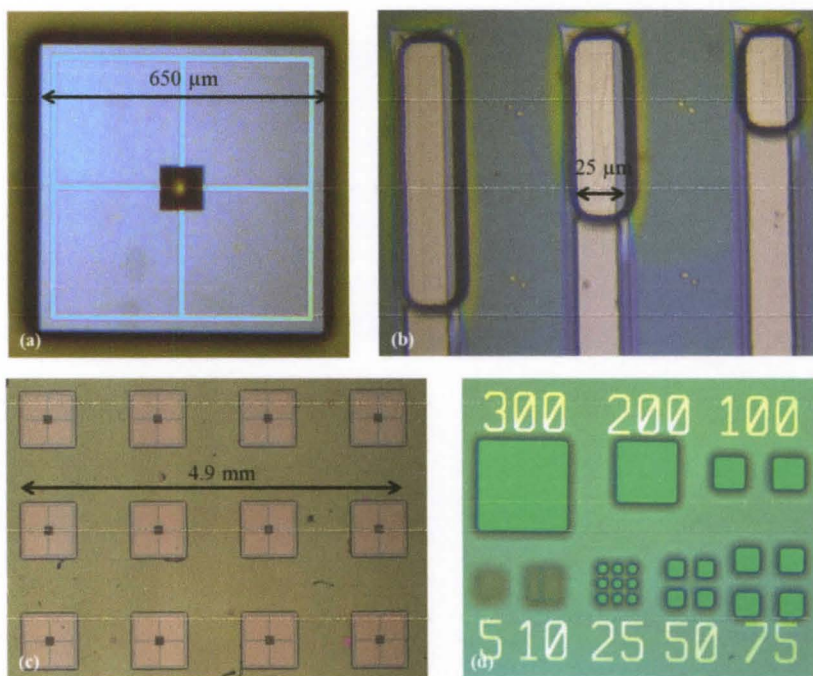


Figure 34. Optical images of (a) individual microstencil, (b) 25  $\mu\text{m}$  wide microstencil stripes, (c) array of microstencils, (d) set of microstencils from 5 to 300  $\mu\text{m}$ .

A Parylene C stencil was utilized to create patterns with varying dimensions (to give an estimate of pattern feature size flexibility) on a silicon surface. Different aqueous

biocompatible solutions were used to create micropatterns: polymer solutions based on PVP (Solution B) and Pluronic® F-127 (Solution C) and colloidal solution of gold nanoparticle covered with CM-chitosan (Solution D).

Figure 35 demonstrates a large scale 650  $\mu\text{m}$  stenciled feature as well as stenciled materials with minimum feature sizes of 25  $\mu\text{m}$  and less, generated using this technology. PVP and Solution B (Figure 35(a) and (b), respectively). Grown fractal patterns (referred to as fractal “trees”) with diameters ranging from 5 - 600  $\mu\text{m}$  for CM-chitosan based solution were obtained after patterning and drying on silicon wafers or glass slides (Figure 35(c), (d)).

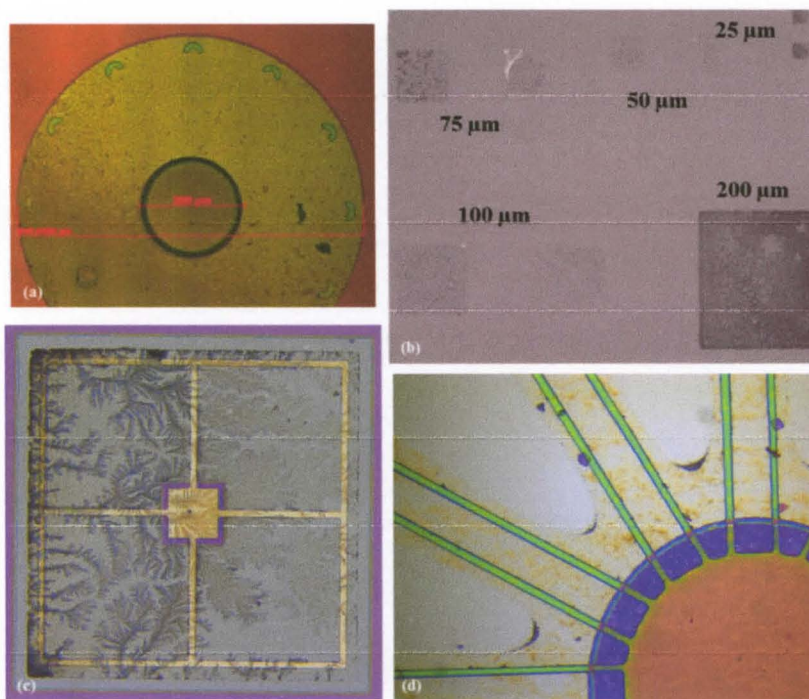


Figure 35. Small (b) and large (a), (c) and (d) scale features generated applying microstencil technique for different aqueous biocompatible solution.

Table 3 summarizes all main aspects of polymer that were used as matrix for nanoparticles solution for deposition by Dimatix inkjet printer and microstenceling technique.

Polymer	Jetable	Stencilable	Adhesion	Dispersion	Water Solubility
PVP	Yes	Yes	Yes	Yes	Yes
CMCS	Yes	Yes	Yes	Yes	Yes
CS	Yes	Yes	Yes	Yes	Yes, but poor solubility above pH 6.5
PMMA	No	Yes	Yes	No	No
Nylon 6	No	Yes	Yes	No	No
PF-127	Yes	Yes	Yes	Yes	Yes

Table 3. Summary of the polymer solutions and their properties.

## 4.6 GOLD NANOPARTICLES

### 4.6.1 PROPERTIES OF NANOPARTICLES

In recent years, metal nanoparticles have received wide attention due to interesting size dependent unique electronic, optical and catalytic properties. Figure 36 is a diagram representing the main properties of metal nanoparticles [53]. Metal nanoparticles have a unique interaction with light. The presence of light with wavelength much larger than the nanoparticle size can establish standing resonance conditions. Light in resonance with the surface plasmon oscillation causes the free electrons in the metal to start to oscillate. This phenomenon is called localized surface plasmon resonance (LSPR) oscillation [155].

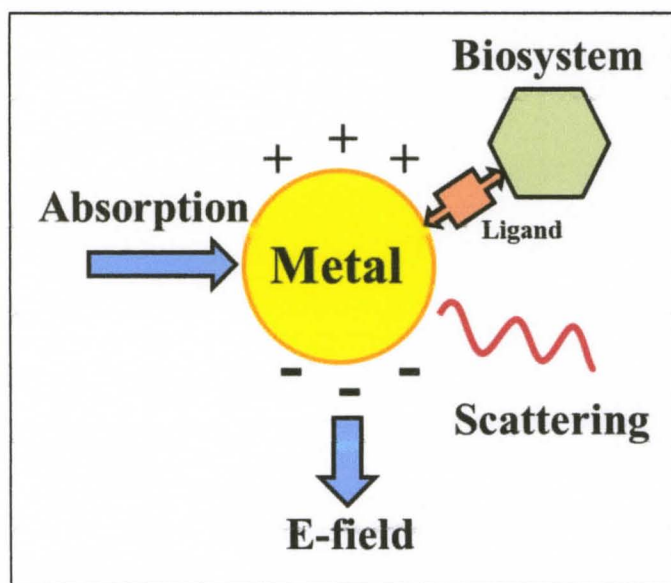


Figure 36. Diagram represents the key properties of gold nanoparticles [53].

Changes of shape or size of the nanoparticle make the surface geometry change, causing a shift in the electric field density on the surface. Modifying the particle shape and diameter becomes a mechanism to change the oscillation frequency of the electrons, generating different cross-sections for the optical properties including absorption and scattering. The surface plasmon oscillation might decay due to light scattering or through the conversion of absorbed light to heat.

Noble metal (gold and silver, in particular) nanoparticles are most attractive for optical applications because of their strongly enhanced surface plasmon at optical frequencies, which makes them exceptional scatterers and absorbers of visible light. Moreover, gold nanoparticles (GNPs) offer good biocompatibility, a simple synthesis process, and the ability to conjugate to a wide range of biomolecular ligands and antibodies. All this makes them suitable for use in biochemical sensing and detection, medical and bio diagnostics [156], and therapeutic applications [157], [50]. Deviation from a spherical nanoparticle shape enables enhanced and adjustable absorption in the NIR region, as well as an improved Raman scattering. Anisotropy of gold nanoparticles (nanotubes, nanocages, nanoshells, nanorods, and triangular nanoprisms) presents multiple absorption bands which correlate with their multiple axes, and they can support both propagating and localized surface plasmon resonances. The number of surface plasmon resonance peaks increases as the symmetry of nanoparticles decreases; spherical nanoparticles exhibit only one peak, gold nanorods have been shown to have two plasmon resonances, due to the transverse and longitudinal oscillation of the electrons, triangle-branched nanocrystals exhibit the plasmon resonance with three bands, corresponding to the two in-plane or longitudinal surface plasmon absorptions at longer

and shorter wavelengths and one out-of-plane or transverse plasmon absorption band [111].

#### **4.6.2 SYNTHESIS OF NANOPARTICLES**

Gold nanoparticles with controllable NIR absorption were synthesized by the reaction of chloroauric acid ( $\text{HAuCl}_4$ ) and sodium thiosulfate ( $\text{Na}_2\text{S}_2\text{O}_3$ ) in Dr. Andre Gobin's laboratory (Bioengineering Department, University of Louisville). The key factor that dominates the nanostructure formation and the stability of the GNPs is the  $\text{HAuCl}_4/\text{Na}_2\text{S}_2\text{O}_3$  reaction. NIR absorption of the gold nanostructures from this reaction is controlled and shows good reproducibility when the molar ratio of  $\text{HAuCl}_4/\text{Na}_2\text{S}_2\text{O}_3$  is in a suitable range. The instability of the GNPs is affected by the reaction conditions, resulting in the diversification of the nanostructures [158].

GNPs were prepared by mixing 1.71 mM  $\text{HAuCl}_4$  (Au 49.68%; Alfa Aesar) with 3 mM  $\text{Na}_2\text{S}_2\text{O}_3$  (99.999%; Sigma - Aldrich) solution. The  $\text{Na}_2\text{S}_2\text{O}_3$  solution is added into the  $\text{HAuCl}_4$  solution with the desired volume ratio and vortexed for 20 seconds for uniform mixing. All the water used in the experiments was purified by a Thermo Scientific Easypure II system with a resistivity of 18.2  $\text{M}\Omega$  cm. Gold nanoparticles were purified and separated by an Allegra® X-12 Series Centrifuge (Beckman Coulter Inc., Brea, CA, USA). Pellets were collected after as-synthesized GNP suspensions were centrifuged at  $1,000\times g$  for 20 minutes and then, were dispersed in deionized water for next characterization. The optical absorbance and intensity of synthesized nanoparticles were measured by a UV-visible-IR spectrophotometer (Cary - 50 Bio, Varian), and

transmission electron microscope (TEM) was used to determine the shape and size of the GNPs.

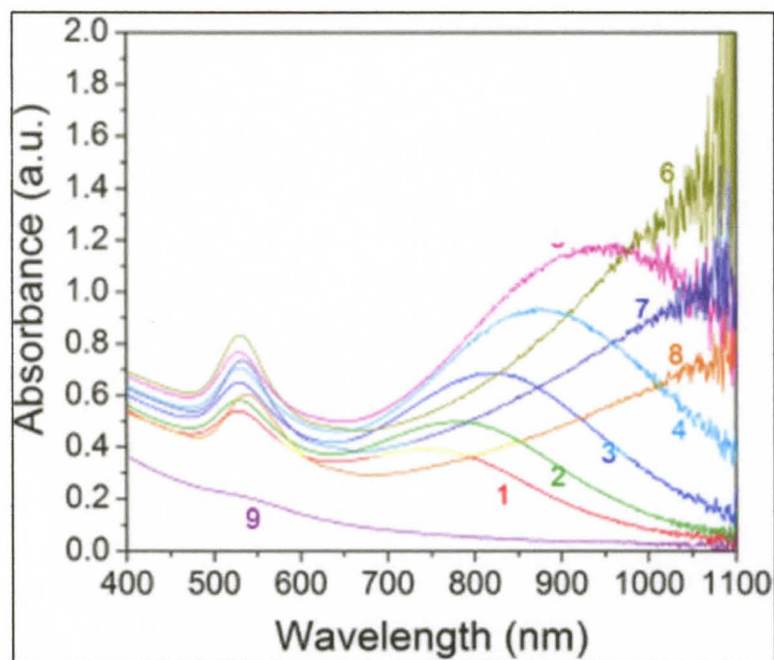


Figure 37. UV-vis-NIR spectra of the nine GNPs samples measured after mixing  $\text{Na}_2\text{S}_2\text{O}_3$  with  $\text{HAuCl}_4$  solution [158].

Figure 37 displays the optical spectra of the typical GNPs samples at 1hr reaction time. They were synthesized by mixing 2.2, 2.0, 1.8, 1.6, 1.4, 1.2, 1.0, 0.8, and 4.0 ml (samples 1 through 9 respectively) of 3.0 mM  $\text{Na}_2\text{S}_2\text{O}_3$  with 5 ml of 1.71 mM  $\text{HAuCl}_4$ . Samples 1-8 have two plasmon resonance peaks and they are clearly observed. The SPR peak around 530 nm is the characteristic SPR of the spherical gold structures, and the second peak SPR component at the higher NIR wavelength is an attribute of the dipole SPR band from the non-spherical gold nanostructures. Peak wavelength and intensity of the NIR bands increment with increasing of  $\text{HAuCl}_4/\text{Na}_2\text{S}_2\text{O}_3$  molar ratio. But sample 9 presents only one weak SPR peak at 530 nm that corresponds to low molar ratio of used



reactant solutions. The SPR of noble metal nanoparticles is dominated by their particle size [159] and shape [160].

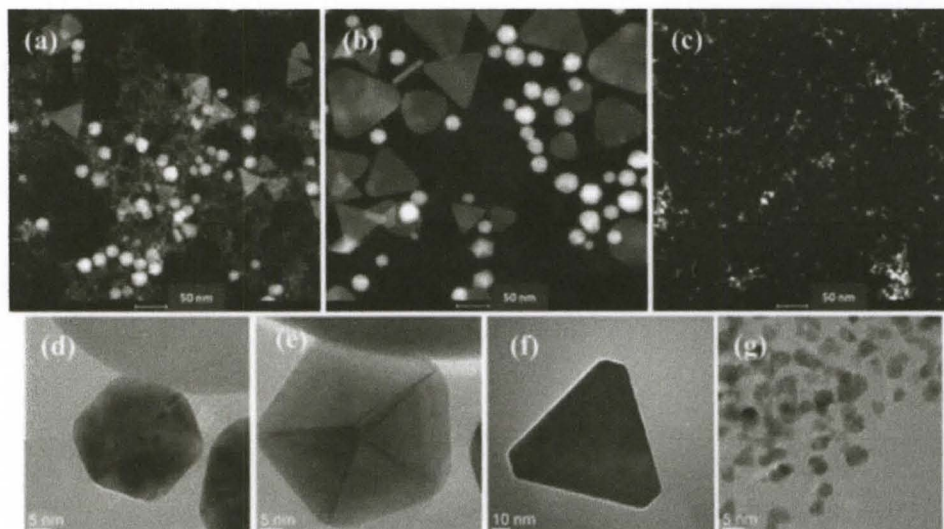


Figure 38. STEM and HRTEM images of gold nanoparticle of different shapes and properties [158].

Figure 38 shows the scanning transmission electron microscopy (STEM) Z - contrast images of typical samples from the synthesis reaction. Figure 38 (a) and (b) is the TEM images of samples with their second NIR SPR band at 750 and 950 nm, respectively. Derived mixtures contain gold particles with different shapes and sizes: the non-spherical gold crystals (including triangular and triangular-shaped plate structures, truncated octahedron, pentagons, etc. [161]) are intermixed among smaller colloidal GNPs of less than 5 nm. The pseudo-spherical crystals have diameters in the range of 15 to 45 nm, and the edges of the nanoplates are in the range of 40 to 95 nm, and thickness is about  $8.5 \pm 1.5$  nm. Figure 38 (c) is the image of sample containing only spherical colloid GNPs with an average size around 3 nm. Figure 38 (d) - (g) shows the high-resolution

TEM images of the typical species of GNPs mixture: cuboctahedrons, pentagons, truncated triangle plates, and colloidal gold particles, respectively.

The important quality of this synthesis method is that the optical properties of the GNPs vary with their size and the population of different non-spherical particles. It is straightforward to tune their NIR absorption wavelengths by adjusting reaction conditions and further size separation.

#### **4.7 THERMAL EFFICIENCY OF GOLD NANOPARTICLES**

The unique properties of gold nanoparticles (NPs), discussed earlier in Chapter I and Section 4.6 of this chapter, appeal a lot of interest and find variety of applications nowadays. One of those NP properties is the ability to generate heat due to absorption of light illumination (incident photons) and conversion of photon energy into heat energy, as well as heat transfer from the nanoparticles to the surrounding medium. As the result of the larger number of free electrons in metals, the photothermal effect is particularly strong for metal nanoparticles that allow creating light activated “nanoheaters”. The effect substantially enhances under collective action of plasmon resonance of electrons in the presence of light [162]. Temperature change is the key parameter for numerous applications of heated nanoparticles [53], [50], [163], but there is not a straightforward method to measure the temperature increase at the surface of the NPs. A few interesting approaches have been applied to estimate the surface temperature of gold NPs in addition to the most commonly used fluorescence method. Gold nanoparticles were imbedded into ice [164] and polymer matrixes [165] and then optically excited. Observation of the melting process of the surrounding material allowed researchers to determine the local

temperature on the surface of the gold NP. The same group has performed a set of experiments on photoheating in a water droplet containing gold nanoparticles using photocalorimetric methods to determine efficiency of light-to-heat conversion [166].

#### 4.7.1 THERMAL EFFICIENCY MEASUREMENT SETUP

The group offered a different method to measure the thermal properties of gold nanoparticles with controllable NIR absorption, which was described in details in the previous Section 4.6.2. The thin-film platinum resistor works as a resistive temperature sensor to measure the thermal properties of nanoparticles under near IR stimulation. Platinum, as the metal surface, was chosen because of its biocompatibility and functionality in high-displacement MEMS actuators, and its large resistive temperature coefficient.

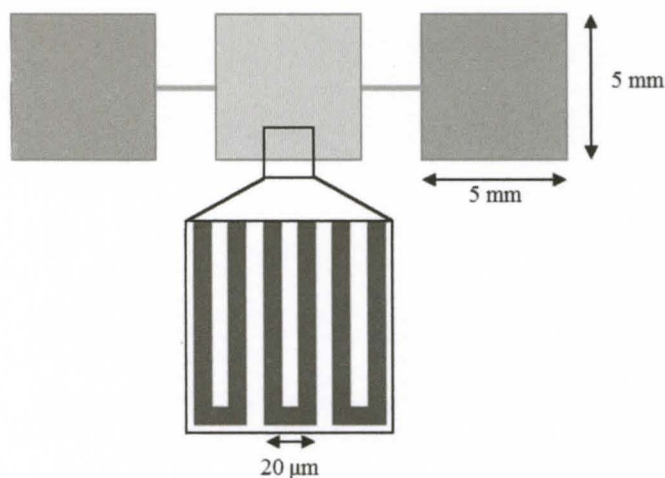


Figure 39. Schematic of the thin-film resistor used to characterize the absorbance of deposited gold nanoparticles.

The planar resistors were fabricated with a single mask cleanroom fabrication sequence. Photoresist was deposited and patterned to define the metal features on the surface of a 500  $\mu\text{m}$  thick borosilicate float glass wafer. Borosilicate float glass is preferred to silicon due to the greater optical transmission and thermal insulation capability of glass. A 200 nm layer of platinum was deposited by sputtering after a brief deposition of titanium to aid adhesion. The proposed metal serpentine geometry was defined via liftoff of the photoresist in acetone bath. After cleaning and drying, the planar resistor is complete; wire connections are made on the left and right bonding pads, across the serpentine platinum trace. Line width and spacing of metal traces are 20  $\mu\text{m}$ ; length of the resistor is about 60 centimeter (Figure 39).

Gold nanoparticles with precisely controlled near infrared absorption were synthesized by one-step reaction of chloroauric acid and sodium thiosulfate in large scale (more details about synthesis in Appendix). The nanoparticles produced from this reaction include small spherical colloidal gold particles with resonance at 530 nm and anisotropic gold nanostructures with NIR resonance (around 800-830 nm) [158].

Figure 40 represents an optical spectrum of the synthesized GNPs with absorption peak used for these experiments. The absorption peaks of each type of gold nanoparticle are clearly seen, and the TEM image of those particles shows two main types of shape in the synthesized mixture, spherical and plate-like.

The NIR resonant GNPs are evenly dispersed onto the planar resistor (center square on Figure 39) by spin-on deposition at 4000 RPM. However, if the particles were suspended in a water medium, the adhesion with the device surface was not sufficient,

and particles also showed a tendency to coagulate. Therefore a polymer matrix was used to disperse the gold nanoparticles and to solve the adhesion issue at the same time.

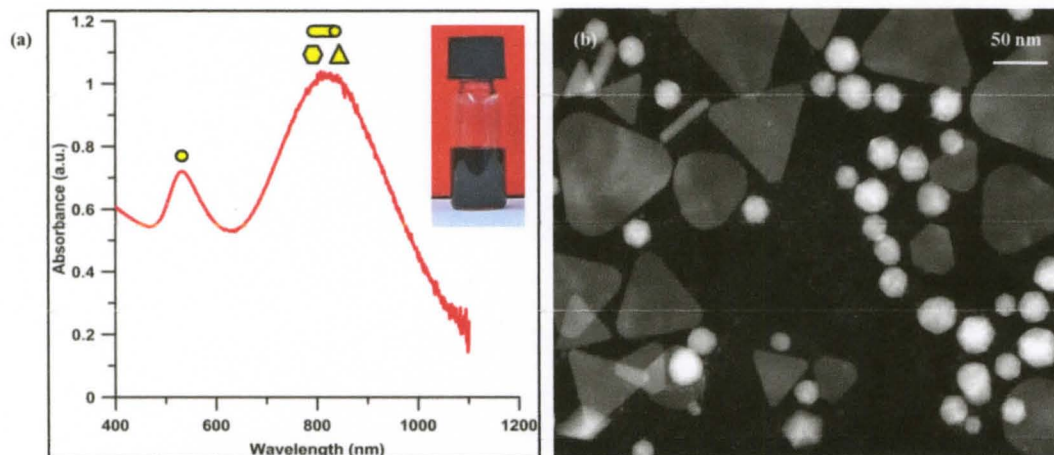


Figure 40. (a) Optical absorption spectrum of synthesized gold nanoparticles, (b) TEM image of synthesized nanoparticles.

PVP, a water-soluble polymer, is been reported as an effective medium for particle dispersion [167]. It adsorbs on the metal surface and protects the ultrafine particles from coagulation by electric or steric repulsion between the absorption layers. PVP polymer was included in the liquid GNPs medium at 8% concentration to achieve well-defined dispersion on device surfaces (Solution E, Appendix).

Chitosan is a natural polymer with attractive properties including excellent film-forming and adhesion ability, biocompatibility, nontoxicity, physiological inertness and pH-dependent solubility. For these reasons it is a promising matrix for gold nanoparticle dispersion and adhesion. Chitosan with gold nanoparticles creates a homogeneous and stable composite sensing film that was demonstrated in an electrochemical glucose sensor

[168] and other biosensors [169]. The gold nanoparticle colloid solution above was mixed with 0.1-1.0% concentrated chitosan mixture (Solution F, Appendix).

Other polymers like Poly(methyl methacrylate) (PMMA) and Nylon-6 were tested for creating nanoparticle-polymer composite, but were not successful (details in Appendix).

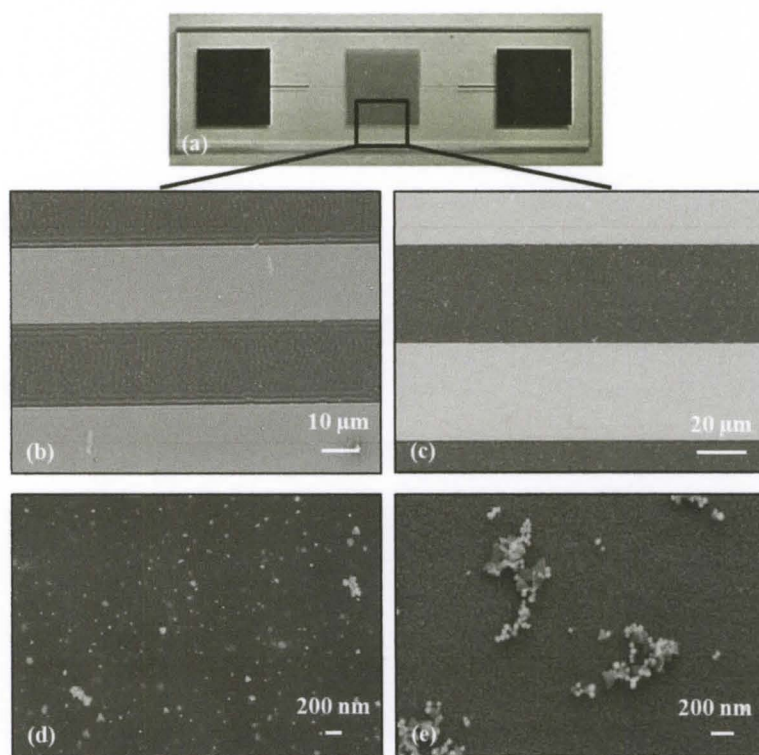


Figure 41. (a) Optical image of fabricated resistive temperature sensor, (b) and (d) SEM images of gold NPs in PVP polymer matrix, (c) and (e) gold NPs in chitosan matrix after spin-coating on the platinum test surface.

Views of the resistor and particle distribution on the platinum surface can be seen in Figure 41. The nanoparticle-PVP composite film offers more uniform particle distribution than chitosan (Figure 41 (b), (d)). Spacing between the particles is within sub wavelength, meaning most infrared interacting with the surface will interact with a

particle. Different optical densities (OD) were tested, but 100 OD solutions show better coverage and consistent results. The average polymer-nanoparticle film thickness is around 200 nm.

Experimental setup for collecting the thermal data and characterizing the gold nanoparticles consist of a laser source, amplifying circuit, and LabVIEW interface (Figure 42). The LabVIEW console operates the laser (5 W diode laser, 808 nm) and collects the output signal from the amplifier circuit with a USB-6009 data acquisition unit. The laser beam focusing head is suspended in 15 cm above the sample.

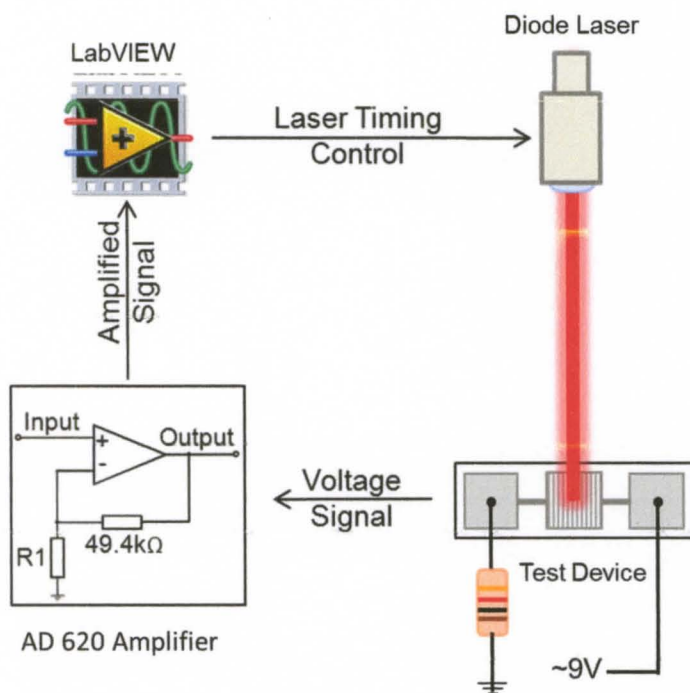


Figure 42. Thermal efficiency measurement setup: a LabVIEW console operates the 808 nm laser, and resistance-induced temperature changes are calculated from voltages measured by an amplifier circuit.

The voltage across the fabricated thin-film resistor is pulling out from a voltage divider setup and is conditioned by an AD 620 amplifier with adjustable gain. The amplified output is read by a National Instruments USB-6009 data acquisition unit and collected by LabVIEW software. The expected analog value being read by the software is estimated by Equation 12.

$$V_0 = GV_s \left( \frac{R_1}{R + R_1} \right) \quad (12)$$

The expected voltage output ( $V_0$ ) is a function of the amplifier gain ( $G$ ), the source voltage  $V_s = 9\text{ V}$ , the fixed resistor  $R_1 = 1000\ \Omega$  and the sample resistance ( $R$ ). The temperature is detected by measuring the electrical resistance of the metal trace, which satisfies the Equation 13.

$$\Delta R = R_0(\alpha\Delta T) \quad (13)$$

The resistance change ( $\Delta R$ ) is defined by the initial value ( $R_0$ ) and change in temperature ( $\Delta T$ ). The thermal coefficient of resistance ( $\alpha$ ) is a material constant that symbolizes the resistance change factor per degree of temperature change. The thermal coefficient of resistance of Pt (bulk value) is  $0.0039\text{ C}^{-1}$ , but it is less for the thin-film Pt and equals to  $\alpha \approx 0.0013\text{ C}^{-1}$ . The coefficient was determined by the relation shown in Equation 13 and the calculated value come to an agreement with earlier studies examining sputtered thin-film platinum [170], [171].

The LabVIEW software manages the laser operation: number of trials and run time. Standard run time for this experiment is four minutes total – the laser is activated for two minutes, then two minutes of cooldown. Figure 43 illustrates the distribution of



maximum temperatures reached by bare and particle coated samples during the run time. The temperature data shows that a platinum surface coated with functionalized gold NPs will absorb more incoming IR light than a bare surface. The observed temperature difference between the of PVP polymer film and bare surface is in average  $\sim 15^{\circ}\text{C}$ , but only  $\sim 3.5^{\circ}\text{C}$  in case of chitosan-nanoparticle matrix. The wide-ranging data is a result of unsteadiness in the dispersion process of the nanoparticles. The analysis of variance (ANOVA) model was applied to the data to show that particle presence on the substrate surface is a substantial factor in the max sample temperature with 95% confidence ( $R^2=0.87$ ).

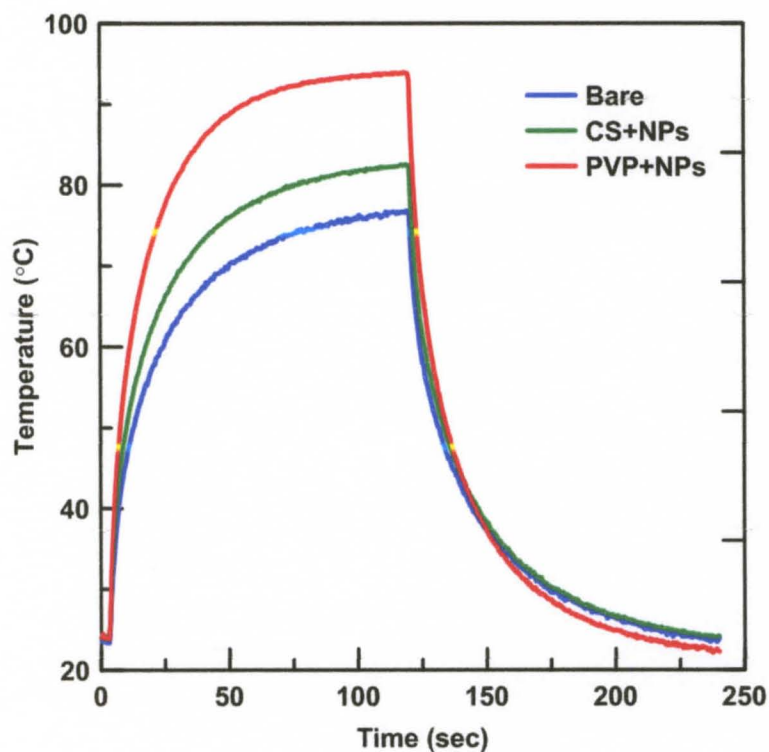


Figure 43. Distribution of maximum temperatures for bare and nanoparticle coated samples.

Figure 44 shows statistical distribution: average value and spread data for bare and both type of coated resistive devices. PVP polymer and chitosan films without gold NPs was shown to have the same thermal behavior as a bare surface.

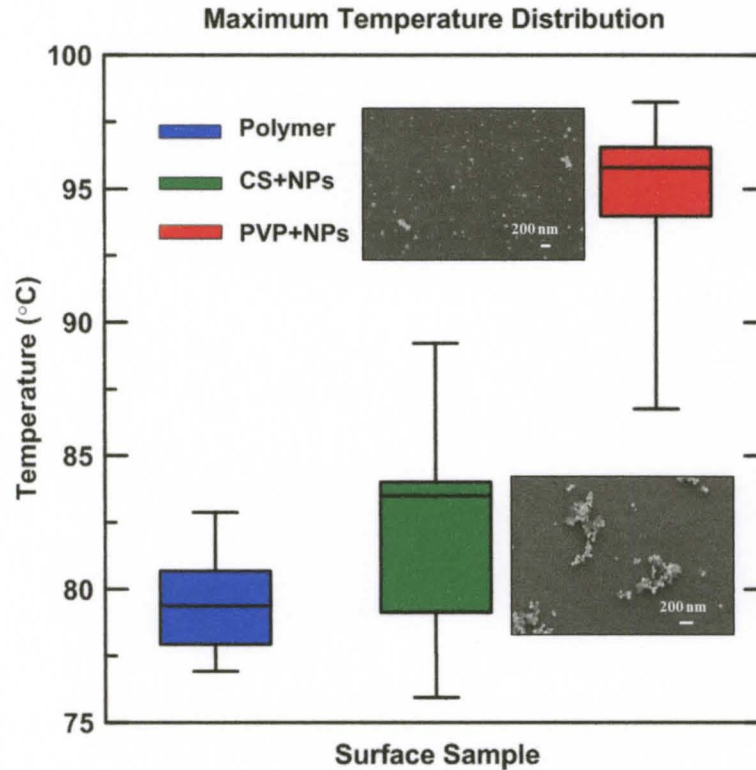


Figure 44. The box plot of the data demonstrates the difference in optical absorption when nanoparticles are applied to the surface.

#### 4.7.2 THERMAL EFFICIENCY ANALYSIS

An estimation of the thermal efficiency ( $\eta$ ), a dimensionless performance measure of a device that converts light to thermal energy, can be derived from basic thermodynamics theory and known material and geometric properties of the samples (Equation 14):

$$\eta = \frac{dQ/dt}{IA} \quad (14)$$

where  $dQ/dt$  is the rate of change of thermal energy due to heating by the laser,  $I$  is the laser intensity and  $A$  is the illuminated area.

Thermal energy ( $Q$ ) in a bulk material at temperature  $T_0$  is given by Equation 14, where  $c_v$  is the volumetric heat capacity of the glass substrate.

$$Q = \iiint (T(x, y, z) - T_0)c_v(x, y, z)dV \quad (15)$$

By differentiating Equation 15, rate of change of thermal energy can be found

$$\frac{dQ}{dt} = \iiint \frac{dT(x, y, z)}{dt} c_v(x, y, z)dV \quad (16)$$

At steady state, total  $dQ/dt$  is equal to 0, because the same amount energy as put in as being removed through conduction, convection and radiative losses. The temperature reaches a plateau (Figure 43).

The thermal efficiency can be figured out experimentally by measuring the surface temperature  $T_{surf}(t)$  after switching off the laser, and fitting it to a decaying exponential.

$$T_{surf}(t) = (T_{max} - T_{min})e^{-\frac{t}{\tau}} + T_{min} \quad (17)$$

where  $T_{max}$  is the plateau temperature that reaches when laser on,  $T_{min}$  is the final temperature after turning the laser off, and  $\tau$  is time constant of temperature decay. Now

$\frac{dT_{surf}}{dt}$  can be found from this:

$$\frac{dT_{surf}}{dt} = \left( \frac{T_{max} - T_{min}}{\tau} \right) e^{-\frac{t}{\tau}} \quad (18)$$

But  $T_{surf}$  is only the surface temperature, but temperature as a function of  $x$ ,  $y$ , and  $z$ . A basic 1-dimensional model of the system, assuming it has  $T_{surf}$  temperature on the top, constant  $T_{min}$  temperature on the back, and the glass does not absorb any infrared light, only metal and nanoparticles on the surface. It means temperature only be a linear function of the depth  $z$ , and not depend on  $x$  and  $y$  planar coordinates.

$$T(x, y, z) = \left( \frac{d - z}{z} \right) (T_{surf} - T_{min}) + T_{min} \quad (19)$$

where  $d$  is the wafer thickness and  $z$  starts at 0 at the surface, and goes to  $d$  at the back of the glass device.

Plugging Equation (19) in Equation (16) and working out the details allows to calculate  $dQ/dt$ . Following substitution in Equation (14) gives an equation for thermal efficiency:

$$\eta = \frac{T_{max} - T_{min}}{\tau l} \int_{z=0}^{z=d} \left( 1 - \frac{z}{d} \right) c_v(z) dz \quad (20)$$

Since it was assumed the substrate is a single material,  $c_v$ , volumetric heat capacity of the glass, is a constant.

The thermal efficiency is calculated in Equation 21 as follows:

$$\eta = \frac{(T_{max} - T_{min})c_v d}{2\tau l} \quad (21)$$

A system with a fast time constant  $\tau$  is losing heat to its environment more quickly than a system with slow time constant, and it has a greater thermal efficiency.

The time constant of temperature decay  $\tau$  and  $T_{max}$  were measured during the trials; thermal efficiency is calculated for the bare and coated substrates and summarized in Table 4. The particle coated surface shows about 143% for chitosan based matrix and 174% for PVP based film greater thermal efficiency compared to the bare platinum. Applying the polymer-nanoparticle composite film increases the thermal efficiency of the device from 6.85% to 9.78% in average in case of chitosan polymer, and from 6.85% to 11.92% in average for PVP polymer matrix.

Factor	Efficiency Factors		
	Bare	Chitosan+NPs	PVP+NPs
Time Constant ( $\tau$ )	24.474	22.401	18.477
Max Temp ( $^{\circ}\text{C}$ )	79.44	82.70	94.57
Efficiency ( $\eta$ )	0.0685	0.0978	0.1192

Table 4. Calculated thermal factors for the bare and coated devices.

#### 4.7.3 DISCUSSION AND POSSIBLE APPLICATION

A simple method based on the thin-film platinum resistive temperature sensor has been developed to measure the thermal properties of nanoparticles under near IR stimulation. The experimental results show that presence of gold nanoparticles with

controllable NIR absorption can generate thermal gradients created from a single light source (808 nm diode laser) and lead to an increase in temperature.

Embedded in a polymer matrix, gold nanoparticles could be used to fabricate MEMS based IR sensors and IR switches, or is part of MEMS-based uncooled IR bolometer arrays. As another example application, Professor Michael D. Dickey and his group from North Carolina State University demonstrate a novel and simple approach for self-folding of thin sheets of polymer using unfocused light [108]. High IR absorbance material (black ink) patterned on the substrate with low IR absorbance properties (polymer sheet) provides localized absorption of IR light which heats the underlying polymer and causes its bending by the hinges. A similar idea can be applied in light-actuated MEMS devices where a gold nanoparticle–polymer composite film is used as a high IR absorbance material deposited on low IR absorbance metal or polymer bilayer structures, and optically induced temperature gradient from printable nanoparticle coatings would provide versatile method of wireless and non-invasive thermal actuation.

Using gold nanoparticles to control local IR absorbance suggests another possible application in bolometer filter arrays that are used in infrared imaging devices. Bolometers are thermal infrared sensors that absorb the incident radiation and cause a thermally isolated membrane to increase its temperature; and temperature is measured by a change of the electrical resistance of the bolometer thermistor [172]. The ability of gold nanoparticles to be tuned to different wavelengths during the synthesis might be used to create interlaced grids analogous to color filters sensitive to red, green, and blue light, but instead sensitive to different regions of the infrared spectrum for a “color” infrared camera. The photosensitive grid can be fabricated as an array of MEMS structures

(cantilevers or diaphragms) with nanoparticles of distinct wavelength sensitivity determined near of the process, instead of setting a fixed wavelength at the beginning by a monolithic dielectric stack absorber as is typically done.

#### **4.8 HYBRID NANOPARTICLE-MEMS ACTUATOR**

Coating photoresponsive nanomaterials such as gold nanoparticles onto MEMS structures offers the ability to create laser-driven bistable MEMS actuators for bioapplications such as studying the effect of mechanical forces on cells, and remotely triggered cardiac muscle stimulators. Infrared-resonant gold nanoparticles that were discussed in a previous Section 4.6.2 can be used as a light-absorbent material to trigger fast movements in thermal MEMS actuators depicted in Chapters II and III.

Figure 45 shows potential applications of these light-triggered actuators for cardiac muscle studies by biomedical researchers, and the creation of novel stimulus-responsive structures for drug delivery or micro pumping. Other applications are possible in IR sensors, light-actuated switches, and other mechanical structures.

Cyclic mechanical forces or strains are commonly used to culture cells in a simulated in-vivo environment by growing them as 2D monolayers on silicone substrates that can be expanded in a controlled manner using a vacuum or solid actuator. A range of responses of vascular smooth muscle cells (VSMC) to those manipulations have been observed, including altered cell proliferation, alignment, and protein expression. It is known that these mechanical forces play an important role in governing cell function and phenotype mechanical stimulation can drive the constructs to a more mature cardiac muscle structure [173], [174].

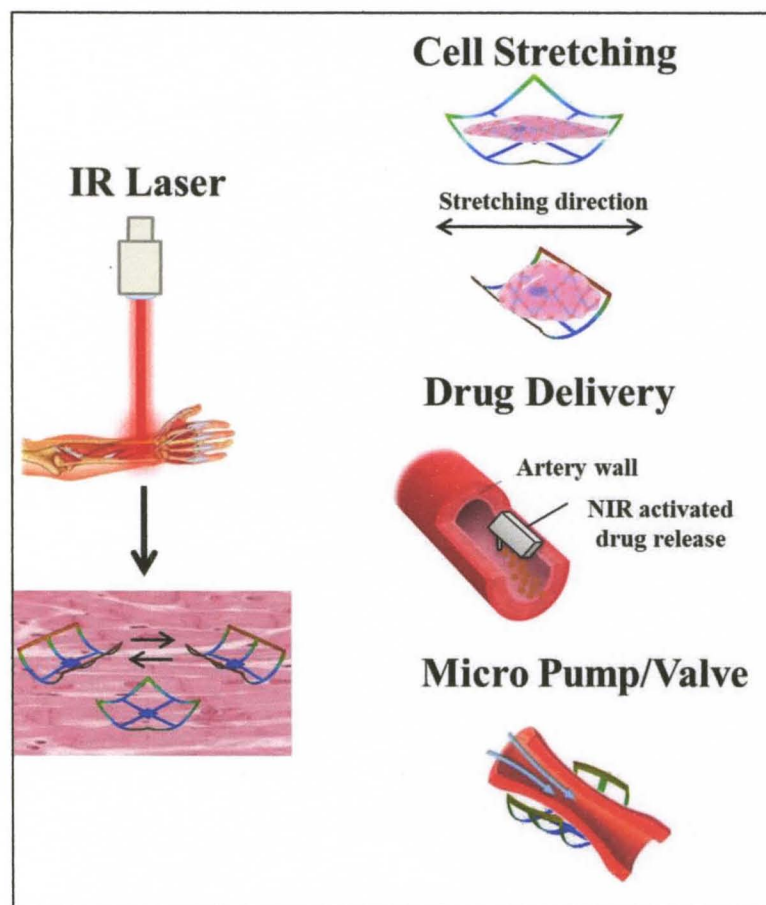


Figure 45. Diagram of light-powered actuators for potential applications for bioresearch.

Stimulus-responsive structures for drug encapsulation and delivery, made on a principle similar to the bilayer devices described in this work, are driven by differential stress due to thermal expansion, surface tension, or polymer swelling, and have a force and feature scale that is relevant to the tissues and cells to which they are applied [175].



#### 4.8.1 FABRICATION AND PRINCIPLE OF OPERATION

The fabrication process sequence for hybrid actuators is presented in Figure 46. A metal/oxide bimorph skeleton is created using a conventional photolithography. A silicon wafer is thermally oxidized at 1000°C to create a 400 nm oxide layer. The first photomask is used to pattern metal to form the desired bistable structure as follows: HMDS adhesion promoter followed by Shipley 1827 (MicroChem) positive photoresist is applied by spinning at 4000 RPM for 10 seconds, soft baking on a hot plate at 115°C for 90 seconds to partially evaporate photoresist solvents, UV light exposure in a Karl Suss contact aligner (SUSS MicroTec) through a photomask, developing of the wafer in Microposit MF319 developer (MicroChem) for one minute to clean any exposed areas followed by rinsing and drying.

A platinum/titanium metal bilayer was deposited onto the wafer by sputtering using a PVD 75 sputtering system (Kurt J. Lesker) followed by lift-off (Figure 46 (a)-(e)). A second mask was used to pattern the SiO<sub>2</sub> layer around the metal bistable skeleton. The nanoparticles are not easily patterned using conventional photolithography techniques or etching through patterned mask of another material. Hence, the microstenciling technique we describe in Section 4.4 is applied to deposit nanoparticles in alignment with structures on the substrate in order to selectively actuate parts of the MEMS structure. Nanoparticles are distributed on the MEMS substrates with the microstencil by spinning or just simple dropping of nanoparticle suspension in polymer, which promotes adhesion (Figure 46 (g) - (i)). The last step in fabrication is the XeF<sub>2</sub> dry etch for releasing the bilayer metal film from the Si substrate (Figure 46 (j)). Finishing this step creates freestanding MEMS bistable actuators for three-dimensional distribution

throughout a tissue sample. Figure 47 shows a SEM image of a fabricated MEMS bistable hybrid coated with nanoparticles and images of zoomed in areas.

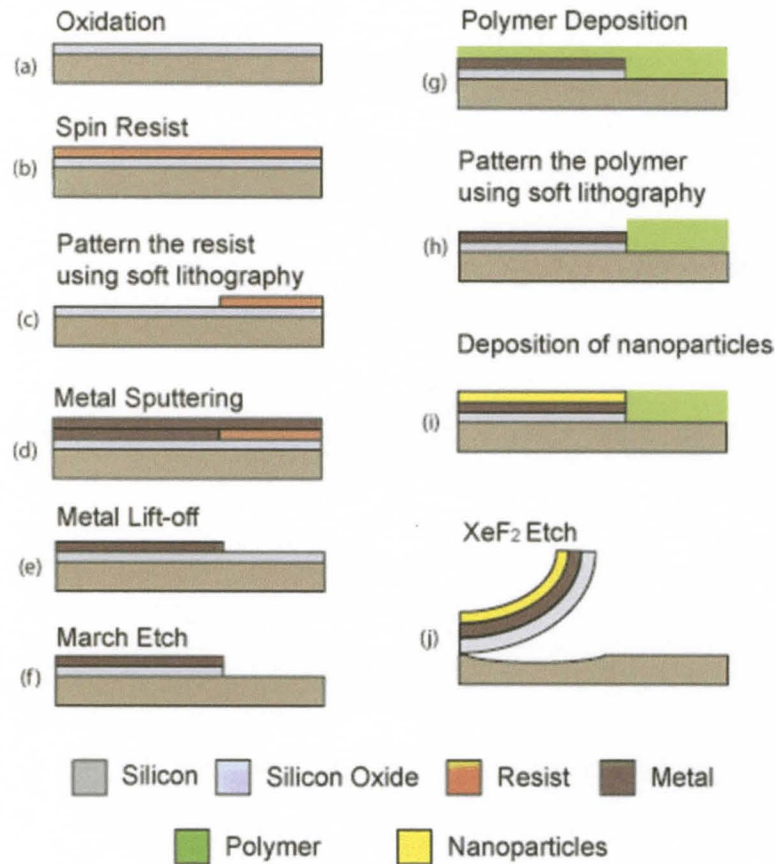


Figure 46. Fabrication process flow for hybrid actuator: (a) Silicon wafer with 400–500 nm thermal oxide, (b) - (e) A 200–300 nm thick metal pattern is applied using photoresist liftoff, (f) The metal acts as an etch mask to pattern the oxide in a  $CF_4/H_2$  plasma etch, (g) Vapor deposition of Parylene C conformal film, (h) Patterning of polymer film using soft lithography and plasma etching, (i) Deposition on nanoparticle, (j) The metal-oxide bimorph is released by etching the silicon in  $XeF_2$  gas.

Fabricated hybrid structures operate at temperatures  $\sim 80\text{-}100^\circ\text{C}$  (which is above the physiological temperature for living cells) and laser illumination up to two minutes at IR wavelengths ( $\sim 808\text{ nm}$ ) that can permeate through tissue without damaging. Spacing between the particles is within sub wavelength, meaning most infrared interacting with the surface will interact with a particle. Preliminary results for nanoparticle-coated MEMS devices are showing increased temperature when IR laser light is illuminated, and this causes their actuation. Although the actuation speed is not too fast – it takes about five seconds to bring the released MEMS actuators to the flat position when the laser is on--and the same time is required to come back to initial state as the laser goes off, a bistable mechanism can trigger fast actuation when the device crosses a threshold angle. MEMS hybrid actuators, released from the substrate but still attached to it, suffer conductive heat loss to the silicon substrate which is suspected to be the cause of slow actuation; fabrication on a low thermal conductivity substrate like glass or a thin membrane can help investigate the heat-loss effect. Fabricated devices show good durability after laser actuation for a few hours.

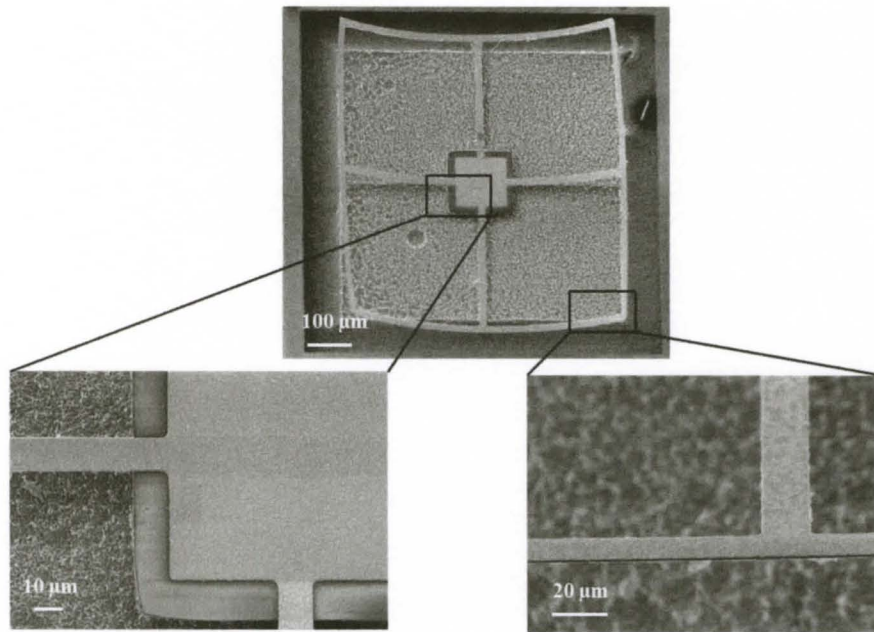


Figure 47. SEM images of fabricated light-powered hybrid with patterned gold nanoparticles.

According to numerical simulations (Chapter III) the bistable actuators have two states of equilibrium, and near the "tipping point" a fairly small temperature change might push the devices past the threshold for a fast mechanical impulse. But in the performed experiments only one stable state was observed. This is expected because, unlike in the serpentine actuator arrays discussed in Chapter III, there is only one direction the laser can actuate the structure: down to the substrate. Differential light absorption on different parts of the structure is required for bidirectional actuation using light. Figure 48 shows the optical images of hybrid device when the laser is on (a) and off (b).

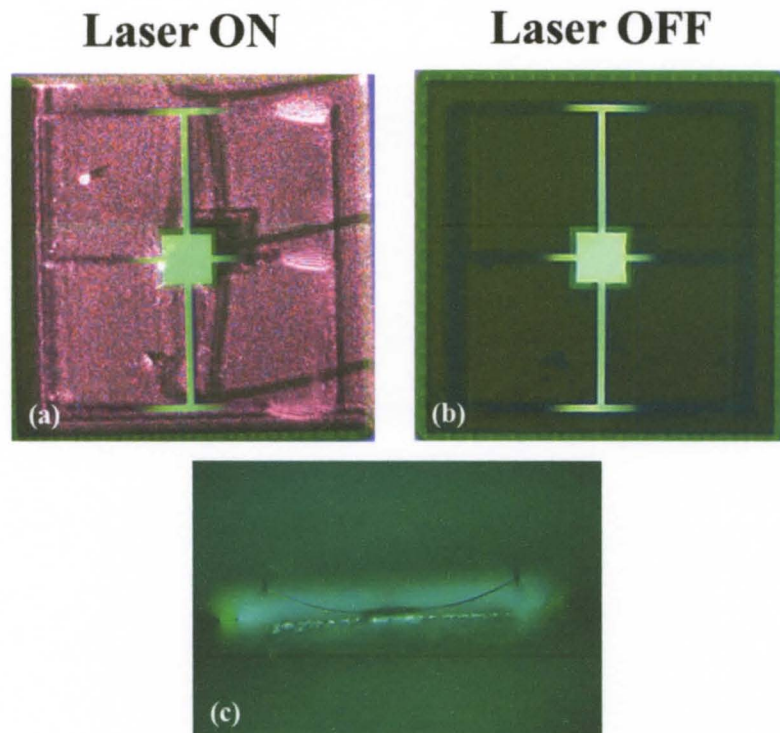


Figure 48. An optical image of light-powered actuator when (a) laser is ON, (b) laser is OFF (c) side view of hybrid actuator.

## **CHAPTER V**

### **CONCLUSION**

This dissertation provides a study of the fabrication, simulation and testing of thermally-driven MEMS-nanoparticle hybrid actuators. The impact of the materials and structures used to create the hybrid micro-nano devices was presented. The key contributions of this study include:

- a) A demonstrated ability to integrate and align photothermal nanomaterials with a MEMS device in a way that does not affect the MEMS fabrication process or the thermal functionality of the nanomaterials.
- b) A review of origami fabrication techniques that is suitable for design and manufacture of MEMS actuators.
- c) An investigation of the bistability of fabricated MEMS devices that produce sudden motion driven by the gradual process of thermal expansion.
- d) A study of the thermal efficiency and an evaluation of the performance of gold nanoparticle-polymer composite coatings on MEMS substrates.

At this stage of the nanoparticle-MEMS hybrid project there are several promising research directions. Bistability needs to be investigated in the context of differential light absorption on different parts of the structure. Ultimately, two different wavelength absorbing coatings could replicate the distinct control of two different actuators that was achieved by direct current in the serpentine devices. However, before

this challenging objective is met, arrays of one-way bistable structures could be designed purely to evaluate the actuation speed with a single, patterned light-absorbent coating.

Even with bistability, the current actuation speed is not fast enough for rapid cycling of device states because of heat loss through conduction to the silicon substrate, but this can be addressed by moving to low thermal conductivity substrates, or alternately by increasing the photothermal absorption of the device through improved coatings. Coatings also need increased water resistance for bio applications, but the existing polymers that have been used as matrixes to disperse gold nanoparticles are water-soluble. Parylene has shown some initial success here.

Experiments that vary the light intensity, device geometry, and construction materials are needed to ensure the devices are suitable for use in biological systems or other fields. Hybrid actuators might be applied as photo- or electrically-actuated valves to drive flow by pressurization and depressurization of fluidic channels within soft actuators which currently use miniature electropermanent magnet valves [176]. Such light-driven valves could effectively drive soft fluidic actuators utilizing rapid pulses of light energy to switch actuation states.

Future fundamental and application-driven work in the biomedical field is expected to use light-powered microactuators for *in situ* studies of cells' response to mechanical stimuli. Such devices could apply forces at the cellular scale, offering potential therapies for heart disease and osteoporosis, and would increase the fundamental understanding of tissue response to everyday mechanical stresses at the molecular level.

## REFERENCES

- [1] J. W. Judy, "Microelectromechanical systems (MEMS): fabrication, design and applications," *Smart Materials and Structures*, vol. 10, pp. 1115-34, 2001.
- [2] P. O. Vaccaro, K. Kubota and T. Aida, "Strain-driven self-positioning of micromachined structures," *Applied Physics Letters*, vol. 78, pp. 2852-4, 2001.
- [3] J. M. Zanardi Ocampo, P. O. Vaccaro, T. Fleischmann, T. S. Wang, K. Kubota and T. Aida, "Optical actuation of micromirrors fabricated by the micro-origami technique," *Applied Physics Letters*, vol. 83, pp. 3647-3649, 2003.
- [4] F. Hu, Y. Tang and Y. Qian, "Design of a MEMS micromirror actuated by electrostatic repulsive force," *Optik*, vol. 123, p. 387– 390, 2012.
- [5] P. O. Vaccaro, K. Kubota, T. Fleischmann, S. Saravanan and T. Aida, "Valley-fold and mountain-fold in the micro-origami technique," *Microelectronics Journal*, vol. 34, pp. 447-449, 2003.
- [6] C. Lee, Y. J. Lai, C. Y. Wu, J. A. Yeh and R. S. Huang, "Feasibility study of self-assembly mechanism for variable optical attenuator," *Journal of Micromechanics and Microengineering*, vol. 15, pp. 55-62, 2005.
- [7] A. Varob'ev, P. Vaccaro, K. Kubota, S. Saravanan and T. Aida, "Array of micromachined components fabricated using 'micro-origami' method," *Japanese Journal of Applied Physics*, vol. 1, pp. 4024-4026, 2003.
- [8] J. T. H. Tsai, K. B. K. Teo and W. I. Milne, "Approach for a self-assembled thin film edge field emitter," *Journal of Vacuum Science and Technology B*, vol. 20, pp.



1-4, 2002.

- [9] O. G. Schmidt and N. Y. Jin-Phillipp, "Free-standing SiGe-based nanopipelines on Si (0 0 1) substrates," *Applied Physics Letters*, vol. 78, pp. 3310-3312, 2001.
- [10] J. W. L. Zhou, H. Y. Chan, T. K. H. To, K. W. C. Lai and W. Li, "Polymer MEMS actuators for underwater micromanipulation," *IEEE/ASME Transactions on Mechatronics*, vol. 9, pp. 334-342, 2004.
- [11] K. Luo, J. H. He, Y. Q. Fu, A. J. Flewitt, S. Spearing, N. Fleck and W. Milne, "Fabrication and characterization of diamond-like carbon/Ni bimorph normally closed microcages," *Journal of Micromechanics and Microengineering*, vol. 15, pp. 1406-1413, 2005.
- [12] T. G. Leong, C. L. Randall, B. R. Benson, N. Bassik, G. M. Stern and D. H. Gracias, "Tetherless thermobiochemically actuated microgrippers," *Proceedings of the National Academy of Sciences U.S.A.*, vol. 106, pp. 703-708, 2009.
- [13] J. W. Suh, R. B. Darling, K. F. Bohringer, B. R. Donald, H. Baltes and G. Kovacs, "CMOS integrated ciliary actuator array as a general-purpose micromanipulation tool for small objects," *Journal of Microelectromechanical Systems*, vol. 8, p. 483, 199.
- [14] C. Chang, C. F. Chiang, C. H. Liu and C. H. Liu, "A lobstersniffing - inspired method for micro-objects manipulation using electrostatic micro-actuators," *Journal of Micromechanics and Microengineering*, vol. 15, pp. 812-821, 2005.
- [15] R. W. Johnstone, D. Sameoto and M. Parameswaran, "Non-uniform residual stresses for parallel assembly of out-of-plane surface micromachined structures," *Journal of Micromechanics and Microengineering*, vol. 16, pp. N17-22, 2006.
- [16] O. Raccurt, F. Tardif, F. Arnaud d'Avitaya and T. Vareine, "Influence of liquid surface tension on stiction of SOI MEMS," *Journal of Micromechanics and*

- Microengineering*, vol. 14, p. 1083–1090, 2004.
- [17] C. Py, P. Reverdy, L. Doppler, J. Bico, B. Roman and C. N. Baroud, "Capillary Origami: Spontaneous Wrapping of a Droplet with an Elastic Sheet," *Physical Review Letters*, vol. 98, p. 156103, 2007.
- [18] M. Boncheva, S. A. Andreev, L. Mahadevan, A. Winklem, D. R. Reichman, M. G. Prentiss, S. Whitesides and G. M. Whitesides, "Magnetic self-assembly of three-dimensional surfaces from planar sheets," *Proceedings of the National Academy of Sciences USA*, vol. 11, p. 3924–3929, 2005.
- [19] R. Syms, E. M. Yeatman, V. M. Bright and G. M. Whitesides, "Surface Tension-Powered Self-Assembly of Microstructures—The State-of-the-Art," *Journal of Microelectromechanical Systems*, vol. 12, no. 4, pp. 387-417, 2003.
- [20] W. Choi, M. Akbarian, V. Rubtsov and C.-J. Kim, "Microhand With Internal Visual System," *IEEE Transactions on Industrial Electronics*, vol. 56, no. 4, pp. 1005-1011, 2009.
- [21] J. Guan, H. He, D. J. Hansford and L. J. Lee, "Self-Folding of Three-Dimensional Hydrogel Microstructures," *The Journal of Physical Chemistry B*, vol. 109, no. 49, pp. 23134-23137, 2005.
- [22] J. Ryu, M. D'Amato, X. Cui, K. N. Long, H. J. Qi and M. L. Dunn, "Photo-origami—Bending and folding polymers with light," *Applied Physics Letters*, vol. 100, p. 161908, 2012.
- [23] T. G. Leong, B. R. Benson, E. K. Call and D. H. Gracias, "Thin Film Stress Driven Self-Folding of Microstructured Containers," *Small*, vol. 4, no. 10, p. 1605–1609, 2008.
- [24] O. G. Schmidt and K. Eberl, "Nanotechnology—thin solid films roll up into nanotubes," *Nature*, vol. 410, p. 168, 2001.

- [25] E. Moiseeva, Y. M. Senousy, S. McNamara and C. K. Harnett, "Single-mask microfabrication of three-dimensional objects from strained bimorphs," *Journal of Micromechanics and Microengineering*, vol. 17, p. N63–N68, 2007.
- [26] S. Takeuchi and I. Shimoyama, "A Three-Dimensional Shape Memory Alloy Microelectrode with Clipping Structure for Insect Neural Recording," *Journal of Microelectromechanical Systems*, vol. 9, no. 1, pp. 24-31, 2000.
- [27] H. Kahn, M. A. Huff and A. H. Heuer, "The TiNi shape-memory alloy and its applications for MEMS," *Journal of Micromechanics and Microengineering*, vol. 8, p. 213–221, 1998.
- [28] A. W. Feinberg, A. Feigel, S. S. Shevkoplyas, S. Sheehy, G. M. Whitesides and K. K. Parker, "Muscular Thin Films for Building Actuators and Powering Devices," *Science*, vol. 317, p. 1366, 2007.
- [29] A. Dittmar and G. Delhomme, "Living tissue mechanisms and concepts as models for biomedical microsystems and devices," in *1 Annual International IEEE-EMBS Special Topic Conference on Microtechnologies in Medicine & Biology*, Lyon, France, 2000.
- [30] V. Y. Prinz, V. A. Seleznev, A. K. Gutakovskiy, A. Chehovskiy, V. Preobrazhenskii and M. A. Putyato, "Free-standing and overgrown InGaAs/GaAs nanotubes, nanohelices and their arrays," *Physica E*, vol. 6, pp. 828-831, 2000.
- [31] M. N. Huang, L. Boone, M. Roberts, D. E. Savage, M. G. Lagally, N. Shaji, H. Qiu, R. Blick, J. A. Nairn and F. Liu, "Nanomechanical architecture of strained bilayer thin films: from design principles to experimental fabrication," *Advanced Materials*, vol. 17, pp. 2860-2864, 2005.
- [32] O. Schumacher, S. Mendach, H. Welsch, A. Schramm, C. Heyn and W. Hansen, "Lithographically defined metal-semiconductor-hybrid nanoscrolls," *Applied Physics Letters*, vol. 86, p. 143109, 2005.

- [33] D. J. Bell, T. J. Lu, N. A. Fleck and S. M. Spearing, "MEMS actuators and sensors: observations on their performance and selection for purpose," *Journal of Micromechanics and Microengineering*, vol. 15, p. S153–S164, 2005.
- [34] J. Grade, H. Jerman and T. W. Kenny, "Design of Large Deflection Electrostatic Actuators," *Journal of Microelectromechanical Systems*, vol. 12, no. 3, pp. 335-343, 2003.
- [35] K. Takahashi, E. Bulgan, Y. Kanamori and K. Hane, "Submicrometer Comb-Drive Actuators Fabricated on Thin Single Crystalline Silicon Layer," *IEEE Transactions on Industrial Electronics*, vol. 56, no. 4, pp. 991-995, 2009.
- [36] Y.-S. Yang, Y. H. Lin, Y. C. Hu and C. H. Liu, "A large-displacement thermal actuator designed for MEMS pitch-tunable grating," *Journal of Micromechanical Microengineering*, no. 19, p. 015001 (12pp), 2009.
- [37] S. Lu and B. Panchapakesan, "Optically driven nanotube actuators," *Nanotechnology*, no. 16, p. 2548–2554, 2005.
- [38] M. S. Dresselhaus, G. Dresselhaus, J. C. Charlier and E. Hernández, "Electronic, thermal and mechanical properties of carbon nanotubes," *Philosophical Transactions of Royal Society, A*, vol. 362, pp. 2065-2098, 2004.
- [39] Z. Wang, R. P. Gao, P. Poncharal, W. A. de Heer, Z. R. Dai and Z. W. Pan, "Mechanical and electrostatic properties of carbon nanotubes and nanowires," *Materials Science and Engineering: C*, vol. 16, no. 1-2, pp. 3-10, 2001.
- [40] Q. Cao, H. S. Kim, N. Pimparkar, J. P. Kulkarni, C. Wang, M. Shim, K. Roy, M. A. Alam and J. A. Rogers, "Medium-scale carbon nanotube thin-film integrated circuits on flexible plastic substrates," *Nature*, vol. 454, pp. 495-500, 2008.
- [41] K. Keren, R. S. Berman, E. Buchstab, U. Sivan and E. Braun, "DNA-Templated Carbon Nanotube Field-Effect Transistor," *Science*, vol. 302, pp. 1380-1382, 2003.

- [42] Z. Xu, X. Chen, X. Qu, J. Jia and S. Dong, "Single-wall carbon nanotube-based voltammetric sensor and biosensor," *Biosensors and Bioelectronics*, vol. 20, p. 579–584, 2004.
- [43] X. Tang, S. Bansaruntip, N. Nakayama, E. Yenilmez, Y.-I. Chang and Q. Wang, "Carbon Nanotube DNA Sensor and Sensing Mechanism," *Nano Letters*, vol. 6, no. 8, pp. 1632-1636, 2006.
- [44] J. C. Riboh, A. J. Haes, A. D. McFarland, C. Ranjit and R. P. Van Duyne, "Gold and Silver Nanoparticles in Sensing and Imaging: Sensitivity of Plasmon Response to Size, Shape, and Metal Composition," *Journal of Physical Chemistry B*, vol. 107, pp. 1772-1780, 2003.
- [45] K. Kostarelos, A. Bianco and M. Prato, "Promises, facts and challenges for carbon nanotubes in imaging and therapeutics," *Nature Nanotechnology*, vol. 4, pp. 627-633, 2009.
- [46] N. L. Rosi and C. A. Mirkin, "Nanostructures in Biodiagnostics," *Chemical Reviews*, vol. 105, p. 1547–1562, 2005.
- [47] A. H. Faraj and P. Wipf, "Nanoparticles in cellular drug delivery," *Bioorganic & Medicinal Chemistry*, vol. 17, p. 2950–2962, 2009.
- [48] K. Kamei, Y. Mukai, H. Kojima, T. Yoshikawa, M. Yoshikawa, G. Kiyohara, T. A. Yamamoto, Y. Yoshioka, N. Okada, S. Seino and S. Nakagawa, "Direct cell entry of gold/iron-oxide magnetic nanoparticles in adenovirus mediated gene delivery," *Biomaterials*, vol. 30, no. 9, p. 1809–1814, 2009.
- [49] S. K. Lai, Y.-Y. Wang and J. Hanes, "Mucus-penetrating nanoparticles for drug and gene delivery to mucosal tissues," *Advanced Drug Delivery Reviews*, vol. 61, no. 2, p. 158–171, 2009.
- [50] A. M. Gobin, E. M. Watkins, E. Quevedo, V. L. Colvin and J. L. West, "Near-infrared-resonant gold/gold sulfide nanoparticles as a photothermal cancer

- therapeutic agent," *Small*, vol. 6, no. 6, p. 745–752, 2010.
- [51] G. A. Somorjai, H. Frei and J. Y. Park, "Advancing the Frontiers in Nanocatalysis, Biointerfaces, and Renewable Energy Conversion by Innovations of Surface Techniques," *Journal of the American Chemical Society*, vol. 131, no. 46, p. 16589–16605, 2009.
- [52] P. M. Tiwari, K. Vig, V. A. Dennis and S. R. Singh, "Functionalized Gold Nanoparticles and Their Biomedical Applications," *Nanomaterials*, no. 1, pp. 31-63, 2011.
- [53] P. K. Jain, X. Huang, I. H. El-Sayed and M. A. El-Sayed, "Noble metals on the nanoscale: optical and photothermal properties and some applications in imaging, sensing, biology, and medicine," *Accounts of Chemical Research*, vol. 41, no. 12, pp. 1578-1586, 2008.
- [54] G. Baffou and R. Quidant, "Thermo-plasmonics using metallic nanostructures as nano-sources of heat," *Laser & Photonics Reviews*, vol. DOI: 10.1002/lpor.201200003., pp. 1-17, 2012.
- [55] A. Pique, S. Mathews, A. Birnbaum and N. Charipar, "Microfabricating 3D structures by laser origami," SPIE Newsroom, 2011.
- [56] H. In, A. Nichol, W. Arora, H. Smith and G. Barbastathis, "Alignment Techniques for the Nanostructured Origami™ 3D Fabrication and Assembly Process," MEMS@MIT Research Abstracts, 2005.
- [57] P. O. Vaccaro, K. Kubota and T. Aida, "Strain-driven self-positioning of micromachined structures," *Appl. Phys. Lett.*, vol. 78, pp. 2852-4, 2001.
- [58] T. Tokuda, Y. Sakano, D. Mori, J. Ohta, M. Nunoshita, P. O. Vaccaro, A. Vorob'ev, K. Kubota and N. Saito, "Fabrication and current-drive of SiGe/Si 'Micro-origami' epitaxial MEMS device on SOI substrate," *Electronics Letters*,

vol. 40, no. 12, 2004.

- [59] W. J. Arora, H. I. Smith and G. Barbastathis, "Membrane folding by ion implantation induced stress to fabricate three-dimensional nanostructures," *Microelectronic Engineering*, vol. 84, p. 1454–1458, 2007.
- [60] J. H. Cho, T. James and D. H. Gracias, "Curving Nanostructures Using Extrinsic Stress," *Advanced Materials*, vol. 22, p. 2320–2324, 2010.
- [61] S. W. Lee, D. Sameoto, A. Mahanfar and M. Parameswaran, "Lithographic stress control for the self-assembly of polymer MEMS structures," *Journal of Micromechanics and Microengineering*, vol. 18, p. 085004 (8pp), 2008.
- [62] P. W. K. Rothmund, "Folding DNA to create nanoscale shapes and patterns," *Nature*, vol. 440, pp. 297-302, 2006.
- [63] H. Dietz, S. M. Douglas and W. M. Shih, "Folding DNA into Twisted and Curved Nanoscale Shapes," *Science*, vol. 325, pp. 725-730, 2009.
- [64] K. Kuribayashi, K. Tsuchiya, Z. You, D. Tomus, M. Umemoto, T. Ito and M. Sasaki, "Self-deployable origami stent grafts as a biomedical application of Ni-rich TiNi shape memory alloy foil," *Materials Science and Engineering A*, vol. 419, p. 131–137, 2006.
- [65] K. Kuribayashi-Shigetomi, H. Onoe and S. Takeuchi, "Self-Folding Cell Origami:Batch Process of Self-Folding 3D Cell-Laden Microstructures Actuated by Cell Traction Force," in *MEMS*, Paris, FranceE, 2012.
- [66] S. Timoshenko, "Analysis of bi-metal thermostats," *Journal of the Optical Society of America*, vol. 11, pp. 233-255, 1925.
- [67] P. Krulevitch and G. C. Johnson, "Curvature of a cantilever beam subjected to an equi-biaxial bending moment," in *Materials Research Society Spring Conference*, San Francisco, 1998.

- [68] J. Thornton and D. W. Hoffman, "Stress-related effects in thin films," *Thin Solid Films*, vol. 171, no. 1, p. 5–31, 1989.
- [69] M. Gad-el-Hak, *The MEMS Handbook*, CRC Press, 2002.
- [70] M. Zecchino and T. Cunningham, "Thin Film Stress Measurement Using Dektak Stylus Profilers," <http://www.bruker-axs.com/>, 2010.
- [71] R. J. Jaccodine and W. A. Schlegel, "Measurements of Strains at Si-SiO Interface," *Journal of Applied Physics*, vol. 37, p. 2429–2434, 1966.
- [72] R. W. Hoffman, "Mechanical Properties of Non-Metallic Thin Films," in *Physics of Nonmetallic Thin Films (NATO Advanced Study Institutes Series: Series B, Physics)*, New York, Plenum Press, 1976, p. 273–353.
- [73] R. C. Weast, *Handbook of Chemistry and Physics 51st edn* (Cleveland, OH: CRC Press), 1971.
- [74] W. Riethmuller and W. Benelke, "Thermally excited silicon microactuators," *IEEE Trans Electron Devices*, vol. 35, pp. 758-763, 1998.
- [75] K. Luo, R. Huang, J. H. He, Y. Q. Fu, A. Flewitt, S. Spearing, N. A. Fleck and W. Milne, "Modelling and fabrication of low operation temperature microcages with a polymer/metal/DLC trilayer structure," *Sensors Actuators A*, vol. 132, pp. 346-53, 2006.
- [76] T. Namazu and S. Inoue, "Characterization of single crystal silicon and electroplated Ni films by uniaxial tensile test with in-situ x-ray diffraction measurement," *Fatigue and Fracture of Engineering Materials and Structures*, vol. 30, p. 13–20, 2007.
- [77] J.-H. Zhao, T. Ryan, P. S. Ho, A. J. McKerrow and W. Shih, "Measurement of elastic modulus, Poisson ratio, and coefficient of thermal expansion of on-wafer submicron films," *Journal of Applied Physics*, vol. 85, p. 6421–6424, 1999.



- [78] J. Lintmyer, N. Martin, J.-M. Chappe, J. Takadoum and P. Delobelle, "Modeling of Young's modulus, hardness, and stiffness of chromium zigzag multilayers sputter deposited," *Thin Solid Films*, vol. 53, p. 177–189, 2006.
- [79] T. Tsuchiya, M. Hirata and N. Chiba, "Young's modulus, fracture strain, and tensile strength of sputtered titanium thin films," *Thin Solid Films*, vol. 484, p. 245–250, 2005.
- [80] Y. Q. Fu, W. M. Huang, H. J. Du, X. Huang, J. P. Tan and X. Y. Gao, "Characterization of TiNi shape memory alloy thin films for MEMS applications," *Surface and Coatings Technology*, vol. 145, p. 107–112, 2001.
- [81] Y. Q. Fu, S. Zhang, M. J. Wu, W. M. Huang, H. J. Du, J. K. Luo, A. J. Flewitt and W. I. Milne, "On the lower thickness boundary of sputtered TiNi films for shape memory application," *Thin Solid Films*, vol. 515, p. 80–86, 2006.
- [82] H. H. Moroi, K. Okimoto, R. Moroi and Y. Terada, "Numeric approach to the biomechanical analysis of thermal effects in coated implants," *The International Journal of Prosthodontics*, vol. 6, p. 564–572, 1993.
- [83] C. K. Harnett, T. M. Lucas, E. V. Moiseeva, B. Casper and L. Wilson, "Microscopic containers for sample archiving in environmental and biomedical sensors," in *IEEE International Instrumentation and Measurement Technology Conference (I2MTC)*, 2010.
- [84] R. I. Leine, "The historical development of classical stability concepts: Lagrange, Poisson and Lyapunov stability," *Nonlinear Dynamics*, vol. 59, p. 173–182, 2010.
- [85] P. G. Opdahl, B. D. Jensen and L. L. Howell, "An Investigation Into Compliant Bistable Mechanism," in *ASME Design Engineering Technical Conferences*, Atlanta, GA, 1998.
- [86] B. Goessling, T. M. Lucas, E. V. Moiseeva, J. W. Aebbersold and C. K. Harnett, "Bistable out-of-plane stress-mismatched thermally actuated bilayer devices with

- large deflection," *Journal of Micromechanics and Microengineering*, vol. 21, p. 065030 (7pp), 2011.
- [87] B. Ando, S. Baglio, C. Trigona, N. Dumas, L. Latorre and P. Nouet, "Nonlinear mechanism in MEMS devices for energy harvesting applications," *Journal of Micromechanics and Microengineering*, vol. 20, p. 125020 (12pp), 2010.
- [88] U. Gowrishetty, K. M. Walsh and T. A. Berfield, "Fabrication of polyimide bistable diaphragms using oxide compressive stresses for the field of 'Buckle MEMS'," *Journal of Micromechanics and Microengineering*, vol. 20, p. 075013 (6pp), 2010.
- [89] Y. Wu, C. Zhang, H. Wang and G. Ding, "Torsion/cantilever-based MEMS bistable mechanisms with different support configurations: structure design and comparison," *Journal of Micromechanics and Microengineering*, vol. 21, p. 045007 (14pp), 2011.
- [90] R. Hill, *The Mathematical Theory of Plasticity*, Oxford University Press, 1998.
- [91] L. Yang, H. Zhou, S. C. Price and W. You, "Parallel-like Bulk Heterojunction Polymer Solar Cells," *Journal of the American Chemical Society*, vol. 134, p. 5432–5435, 2012.
- [92] L. Heng, X. Wang, N. Yang, J. Zhai, M. Wan and L. Jiang, "P–n-Junction-Based Flexible Dye-Sensitized Solar Cells," *Advanced Functional Materials*, vol. 20, p. 266–271, 2010.
- [93] M. Green, K. Emery, Y. Hishikawa, W. Warta and E. D. Dunlop, "Solar cell efficiency tables (version 39)," *Progress in Photovoltaics: Research and Applications*, vol. 20, no. 1, pp. 12-20, 2012.
- [94] B. Haji-saeed, J. Khoury, K. Vaccaro, C. L. Woods, J. Kierstead, B. Krejca, A. Davis, W. 2, and William D. Goodhue<sup>3</sup> and W. D. Goodhue, "All Optically-Driven MEMS Deformable Device via an array of Photodetectors," in *Proceedings of the*

*SPIE*, Orlando, FL , 2009.

- [95] A. Kholkin, V. K. Yarmarkin, B. M. Goltsman and J. L. Baptisa, "Photoelectric evaluation of polarization and internal field in PZT thin films," *Integrated Ferroelectrics*, vol. 35, no. 1-4, pp. 261-268, 2001.
- [96] K. Esaklul, B. G. Koepke and W. W. Gerberich, "Photomechanical effects in PZT," *Ferroelectrics*, vol. 48, pp. 281-286, 1983.
- [97] P. Beard, F. Perennes, E. Draguioiti and T. N. Mills, "Optical fiber photoacoustic-photothermal probe," *Optics Letters*, vol. 23, no. 15, pp. 1235-1237, 1998.
- [98] E. Holthoff, J. Bender, P. Pellegrino and A. Fisher, "Quantum Cascade Laser-Based Photoacoustic Spectroscopy for Trace Vapor Detection and Molecular Discrimination," *Sensors*, vol. 10, pp. 1986-2002, 2010.
- [99] K. Lee and T. J. White, "Photochemical Mechanism and Photothermal Considerations in the Mechanical Response of Monodomain, Azobenzene-Functionalized Liquid Crystal Polymer Networks," *Macromolecules*, vol. 45, p. 7163-7170, 2012.
- [100] M. Yamada, M. Kondo, J. Mamiya, Y. Yu, M. Kinoshita, C. J. Barrett and T. Ikeda, "Photomobile Polymer Materials: Towards Light-Driven Plastic Motors," *Angewandte Chemie International Edition*, vol. 47, p. 4986-4988, 2008.
- [101] A. Athanassiou, K. Lakiotaki, M. Kalyva, S. Georgiou and C. Fotakis, "Photoswitches operating upon ns pulsed laser irradiation," *Applied Surface Science*, vol. 248, p. 56-61, 2005.
- [102] A. Ashkin, "Optical trapping and manipulation of neutral particles," *PNAS*, vol. 94, p. 4853-4860, 1997.
- [103] J. Shaevitz, *A Practical Guide to Optical Trapping*, University of Washington, 2006.

- [104] H. Mizoguchi, M. Ando, T. Mizuno, T. Takagi and N. Nakajima, "Design and Fabrication of Light Driven Micropump," in *Micro Electro Mechanical Systems*, Travemunde (Germany), 1992.
- [105] Q. Ren, Y.-P. Zhao, L. Han and H.-B. Zhao, "A nanomechanical device based on light-driven proton pumps," *Nanotechnology*, vol. 17, p. 1778–1785, 2006.
- [106] S. Maruo, K. Ikuta and H. Korogi, "Force-Controllable, Optically Driven Micromachines Fabricated by Single-Step Two-Photon Microstereolithography," *Journal of Microelectromechanical Systems*, vol. 12, no. 5, pp. 533-539, 2003.
- [107] A. Grimes, D. N. Breslaue, M. Long, J. Pegan, L. P. Lee and M. Khine, "Shrinky-Dink microfluidics: rapid generation of deep and rounded patterns," *Lab on a Chip*, vol. 8, pp. 170-172, 2008.
- [108] Y. Liu, J. K. Boyles, J. Genzer and M. D. Dick, "Self-folding of polymer sheets using local light absorption," *Soft Matter*, vol. 8, pp. 1764-1769, 2012.
- [109] P. Pandey, M. Datta and B. D. Malhotra, "Prospects of nanomaterials in biosensors," *Analytical Letters*, vol. 41, pp. 159-209, 2008.
- [110] Y. Sun and Y. Xia, "Shape-controlled synthesis of gold and silver nanoparticles," *Science*, vol. 298, p. 2176–2179, 2002.
- [111] M. Tréguer-Delapierre, J. Majimel, S. Mornet, E. Duguet and S. Ravaine, "Synthesis of nonspherical gold nanoparticles," *Gold Bulletin*, vol. 41, pp. 195-207, 2008.
- [112] C. Rao, A. Muller and A. K. Cheetham, *The chemistry of nanomaterials*, Weinheim: Wiley-VCH, 2004.
- [113] K. K. Caswell, C. M. Bender and C. J. Murphy, "Seedless, surfactantless wet chemical synthesis of silver nanowires," *Nano Letters*, vol. 3, no. 5, pp. 667-669, 2003.

- [114] L. R. Hirsch, A. M. Gobin, A. R. Lowery, F. Tam, R. A. Drezek, N. J. Halas and J. L. West, "Metal Nanoshells," *Annals of Biomedical Engineering*, vol. 34, no. 1, p. 15–22, 2006.
- [115] X. Jiang, Q. Zeng and A. Yu, "A self-seeding coreduction method for shape control of silver nanoplates," *Nanotechnology*, vol. 17, p. 4929–4935, 2006.
- [116] H. Chu, C. H. Kuo and M. H. Huang, "Thermal aqueous solution approach for the synthesis of triangular and hexagonal gold nanoplates with three different size ranges," *Inorganic Chemistry*, vol. 45, p. 808–813, 2006.
- [117] C. Murray, D. J. Naris and M. G. Bawendi, "Synthesis and characterization of nearly monodisperse CdE (E =  $\frac{1}{4}$  sulphur, selenium, tellurium) semiconductor nanocrystallites," *Journal of the American Chemical Society*, vol. 115, p. 8706–8715, 1993.
- [118] S. C. Tsai, Y. L. Song, C. S. Tsai, C. C. Yang, W. Y. Chiu and H. M. Lin, "Ultrasonic spray pyrolysis for nanoparticles synthesis," *Journal of Materials Science*, vol. 39, p. 3647 – 3657, 2004.
- [119] F. Kruijs, H. Fissan and A. Peled, "Synthesis of nanoparticles in the gas phase for electronic, optical and magnetic applications—a review," *Journal of Aerosol Science*, vol. 29, no. 5/6, pp. 511-535, 1998.
- [120] N. G. Semaltianos, "Nanoparticles by laser ablation," *Critical Reviews in Solid State and Materials Sciences*, vol. 35, pp. 105-124, 2010.
- [121] S. Besner, A. V. Kabashin, F. M. Winnik and M. Meunier, "Ultrafast laser based "green" synthesis of non-toxic nanoparticles in aqueous solutions," *Applied Physics A*, vol. 93, p. 955–959, 2008.
- [122] D. Vollath, "Plasma synthesis of nanoparticles," *KONA*, vol. 25, pp. 29-54, 2007.
- [123] J. Phillips, C. C. Luhrs and M. Richard, "Review: Engineering particles using the

- aerosol-through-plasma method," *IEEE transactions on plasma science*, vol. 37, no. 6, pp. 726-739, 2009.
- [124] R. Mueller, L. Madler and S. E. Pratsinis, "Nanoparticle synthesis at high production rates by flame spray pyrolysis," *Chemical Engineering Science*, vol. 58, p. 1969 – 1976, 2003.
- [125] B. Hall, C. Zhuo, Y. A. Levendis and H. Richter, "Influence of the fuel structure on the flame synthesis of carbon nanomaterials," *Carbon*, vol. 49, pp. 3412-3423, 2011.
- [126] P. Liu, H. Cui, C. X. Wang and G. W. Yang, "From nanocrystal synthesis to functional nanostructure fabrication: Laser ablation in liquid," *Physical Chemistry Chemical Physics*, vol. 16, no. 16, pp. 3942-3952, 2010.
- [127] M. Kumar and Y. Ando, "Chemical vapor deposition of carbon nanotubes: A review on growth mechanism and mass production," *Journal of Nanoscience and Nanotechnology*, vol. 10, p. 3739–3758, 2010.
- [128] Y. Yoon and H. K. Baik, "Catalytic growth mechanism of carbon nanofibers through chemical vapor deposition," *Diamond and Related Materials*, vol. 10, pp. 1214-1217, 2001.
- [129] V. Schmidt, J. V. Wittemann and U. Gosele, "Growth, thermodynamics, and electrical properties of silicon nanowires," *Chemical Reviews*, vol. 110, p. 361–388, 2010.
- [130] J. Shi and X. Wang, "Functional semiconductor nanowires via vapor deposition," *Journal of Vacuum Science & Technology B*, vol. 29, pp. 060801-1-21, 2011.
- [131] C. Miao, C. Zheng, O. Liang and Y.-H. Xie, "Chemical vapor deposition of graphene," in *Physics and Applications of Graphene - Experiments*, InTech, 2011, pp. 37-54.

- [132] S. Desai, "Surface modifications of one-dimensional nanostructures and their effect on adsorption/desorption properties (chemical sensors," Thesis (Ph.D.) University of Louisville, 2009.
- [133] P. W. Barone, S. Baik, D. A. Heller and M. S. Strano, "Near-infrared optical sensors based on single-walled carbon nanotubes," *Nature Materials* , vol. 4, pp. 86-92, 2005.
- [134] L. F. Deravi, A. E. Gerdon, D. E. Cliffler, D. W. Wright and J. L. Sumerel, "Output analysis of materials inkjet printer," *Applied Physics Letter*, vol. 91, p. 113114, 2007.
- [135] A. Zarowna, E. Gu, E. O. McKenna, M. D. Dawson, A. Pitt, J. M. Cooper and H. B. Yin, "Generation of protein micropattern by piezoelectric printing," *European Cells and Materials*, vol. 18, no. 2, p. 115, 2009.
- [136] Doraiswamy, A.; Dinu, C.Z.; Sumerel, J.; Chrisey, D.B.; Narayan, R. J., "Microstructured bioactive interfaces using piezoelectric ink jet technology," in *MRS Proceedings*, 2006.
- [137] S. Su, M. M. Ali, C. M. Filipe, Y. Li and R. Pelton, "Microgel-based inks for paper-supported biosensing applications," *Biomacromolecules*, vol. 9, p. 935–941, 2008.
- [138] J. Sumerel, J. Lewis, A. Doraiswamy, L. F. Deravi, S. L. Sewell, A. E. Gerdon, D. W. Wright and R. J. Narayan, "Piezoelectric ink jet processing of materials for medical and biological applications," *Biotechnology Journal*, vol. 1, p. 976–987, 2006.
- [139] V. Sanchez-Romaguera, M.-B. Madec and S. G. Yeates, "Inkjet printing of 3D metal–insulator–metal crossovers," *Reactive & Functional Polymers* , vol. 68, p. 1052–1058, 2008.

- [140] T. Mustonen, J. Maklin, K. Kordas, N. Halonen, G. Toth, S. Saukko, J. Vahakangas, H. Jantunen, S. Kar, P. M. Ajayan, R. Vajtai, P. Helisto, H. Seppa and H. Moilanen, "Controlled Ohmic and nonlinear electrical transport in inkjet-printed single-wall carbon nanotube films," *Physical Review B*, vol. 77, p. 125430, 2008.
- [141] A. Denneulin, J. Bras, A. Blayo, B. Khelifi, F. Roussel-Dherbey and C. Neuman, "The influence of carbon nanotubes in inkjet printing of conductive polymer suspensions," *Nanotechnology*, vol. 20, no. 38, p. 385701, 2009.
- [142] W. Small, F. Masdarolomoor, G. Wallace and M. in het Panhuis, "Inkjet deposition and characterization of transparent conducting electroactive polyaniline composite films with a high carbon nanotube loading fraction," *Journal of Materials Chemistry*, vol. 17, p. 4359–4361, 2007.
- [143] R. D. Deegan, O. Bakajin, T. F. Dupont, G. Huber, S. R. Nagel and T. A. Witten, "Capillary flow as the cause of ring stains from dried liquid drops," *Nature*, vol. 389, pp. 827-829, 1997.
- [144] A. Konig, E. Bourgeat-Lami, V. Mellon, K. von der Ehe, A. F. Routh and D. Johannsmann, "Dilational Lateral Stress in Drying Latex Films," *Langmuir*, vol. 26, no. 6, p. 3815–3820, 2010.
- [145] A. Han, M. Graff, O. Wang, S. K. Mohanty, K.-H. Han and A. B. Frazier, "A multi-layer plastic/glass technology for microfluidic systems with integrated functionality," in *TRANSDUCERS, Solid-State Sensors, Actuators and Microsystems, 12th International Conference on*, 2003.
- [146] M. Graff, S. K. Mohanty, E. Moss and A. B. Frazier, "Microstenciling: A generic technology for microscale patterning of vapor deposited materials," *Journal of Microelectromechanical Systems*, vol. 13, no. 6, pp. 956-962, 2004.
- [147] W. Longsine and A. Han, "Laser stenciling for polymer microfluidic devices," in *14th International Conference on Miniaturized Systems for Chemistry and Life*



*Sciences*, Groningen, The Netherlands, 2010.

- [148] K. Ellison, D. B. Chrisey and D. M. Thompson, "Laser-machining of elastomeric microstencils," *Journal of Optoelectronics and Advanced Materials*, vol. 12, pp. 659 - 662, 2010.
- [149] Y. Xia and G. M. Whitesides, "Soft lithography," *Angewandte Chemie International Edition*, vol. 37, pp. 550 -575, 1998.
- [150] E. Meng and Y.-C. Tai, "Parylene etching techniques for microfluidics and bioMEMS," in *Micro Electro Mechanical Systems, MEMS, 18th IEEE International Conference on*, 2005.
- [151] B. Ilic and H. G. Craighead, "Topographical patterning of chemically sensitive biological materials using a polymer-based dry lift off," *Biomedical Microdevices*, vol. 2, no. 4, pp. 317-322, 2000.
- [152] T. Yao, X. Yang and Y. C. Tai, "BrF<sub>3</sub> dry release technology for large freestanding parylene microstructures and electrostatic actuators," *Sensors and Actuators A: Physical*, Vols. 97-98, pp. 771-775, 2002.
- [153] W. Lee, W. Fon, B. W. Axelrod and M. L. Rourke, "High-sensitivity microfluidic calorimeters for biological and chemical applications," *Proceedings of the National Academy of Sciences of the United States of America*, vol. 106, no. 36, p. 15225–15230, 2009.
- [154] J. M. Hsu, L. Rieth, R. A. Normann, P. Tathireddy and F. Solzbacher, "Encapsulation of an integrated neural interface," *IEEE Transactions on Biomedical Engineering*, vol. 56, no. 1, pp. 23-29, 2009.
- [155] S. Eustis and M. A. El-Sayed, "Why gold nanoparticles are more precious than pretty gold: Noble metal surface plasmon resonance and its enhancement of the radiative and nonradiative properties of nanocrystals of different shapes," *Chemical*

*Society Reviews*, vol. 35, p. 209–217, 2006.

- [156] N. L. Rosi and C. A. Mirkin, "Nanostructures in biodiagnostics," *Chemical Reviews*, vol. 105, no. 4, p. 1547–1562, 2005.
- [157] C. Alric, J. Taleb, G. Le Duc, C. Mandon, C. Billotey, A. Le Meur-Herland, T. Brochard, F. Vocanson, M. Janier, P. Perriat, S. Roux and O. Tillement, "Gadolinium chelate coated gold nanoparticles as contrast agents for both X-ray computed tomography and magnetic resonance imaging," *Journal of the American Chemical Society*, vol. 130, p. 5908–5915., 2008.
- [158] G. Zhang, J. B. Jasinski, J. L. Howell, D. Patel, D. P. Stephens and A. M. Gobin, "Tunability and stability of gold nanoparticles obtained from chloroauric acid and sodium thiosulfate reaction," *Nanoscale Research Letters*, vol. 7, p. 337, 2012.
- [159] K. Kelly, E. Coronado, L. L. Zhao and G. C. Schatz, "The Optical Properties of Metal Nanoparticles: The Influence of Size, Shape, and Dielectric Environment," *Journal of Physical Chemistry B*, vol. 107, pp. 668-677, 2003.
- [160] S. Link and M. A. El-Sayed, "Size and temperature dependence of the plasmon absorption of colloidal gold nanoparticles," *Journal of Physical Chemistry B*, vol. 103, p. 4212–4217, 1999.
- [161] B. Teo and H. Zhang, "Magic Numbers in Clusters: Nucleation and Growth Sequences Bonding, Principles, and Packing Patterns," in *Metal Nanoparticles: Synthesis, Characterization, and Applications*, New York, Marcel Dekker, Inc., 2002, pp. 55-88.
- [162] A. Govorov and H. H. Richardson, "Generating heat with metal nanoparticles," *Nano Today*, vol. 2, no. 1, pp. 30-38, 2007.
- [163] A. M. Gobin, M. H. Lee, N. J. Halas, W. D. James, R. A. Drezek and J. L. West, "Near-Infrared Resonant Nanoshells for Combined Optical Imaging and

- Photothermal Cancer Therapy," *Nano Letters*, vol. 7, no. 7, pp. 1929-1934, 2007.
- [164] H. H. Richardson, Z. N. Hickman, A. O. Govorov, A. C. Thomas, W. Zhang and M. E. Kordesch, "Thermo-optical Properties of Gold Nanoparticles Embedded in Ice: Characterization of Heat Generation and Melting," *Nano Letters*, vol. 6, no. 4, pp. 783-788, 2006.
- [165] J. Lee, A. O. Govorov and N. A. Kotov, "Nanoparticle Assemblies with Molecular Springs: A Nanoscale Thermometer," *Angewandte Chemie International Edition*, vol. 44, pp. 7439-7442, 2005.
- [166] H. H. Richardson, M. T. Carlson, P. J. Tandler, P. Hernandez and A. O. Govorov, "Experimental and Theoretical Studies of Light-to-Heat Conversion and Collective Heating Effects in Metal Nanoparticle Solutions," *Nano Letters*, vol. 9, no. 3, pp. 1139-1146, 2009.
- [167] M. Zheng, M. Gu, Y. Jin and G. Jin, "Optical properties of silver-dispersed PVP thin film," *Materials Research Bulletin*, vol. 36, p. 853-859, 2001.
- [168] D. Feng, F. Wang and Z. Chen, "Electrochemical glucose sensor based on one-step construction of gold nanoparticle-chitosan composite film," *Sensors and Actuators B*, vol. 138, p. 539-544, 2009.
- [169] J. M. Pingarron, P. Yanez-Sedeno and A. Gonzalez-Cortes, "Gold nanoparticle-based electrochemical biosensors," *Electrochimica Acta*, vol. 53, p. 5848-5866, 2008.
- [170] F. W. Reynolds, "Some Effects of Gas upon the Resistance and Resistance-Temperature Coefficient of Sputtered Platinum Films," *Physical Review*, vol. 24, pp. 523-531, 1924.
- [171] L. R. Koller, "Physical Properties of Thin Metallic Films. III. Some Factors Affecting the Resistance of Sputtered Platinum Films," *Physical Review*, vol. 18,

pp. 221-235, 1921.

- [172] F. Niklaus, C. Vieider and H. Jakobsen, "MEMS-Based Uncooled Infrared Bolometer Arrays – A Review," in *MEMS/MOEMS Technologies and Applications III*, Beijing, China, 2007.
- [173] J. P. Stegemann, H. Hong and R. M. Nerem, "Mechanical, biochemical, and extracellular matrix effects on vascular smoothmuscle cell phenotype," *Journal of Applied Physiology*, vol. 98, p. 2321–2327, 2005.
- [174] J. M. Meunier, S. Ramalingam, S. F. Lin and A. R. Patwardhan, "Capture of activation during ventricular arrhythmia using distributed stimulation," *Journal of Interventional Cardiac Electrophysiology*, vol. 18, p. 207–215, 2007.
- [175] R. Fernandes and D. H. Gracias, "Self-folding polymeric containers for encapsulation and delivery of drugs," *Advanced Drug Delivery Reviews*, vol. 64, no. 14, pp. 1579-1589, 2012.
- [176] A. D. Marchese, C. D. Onal and D. Rus, "Soft robot actuators using energy-efficient valves controlled by electropermanent magnets," in *IEEE/RSJ International Conference on Intelligent Robots and Systems (IROS)*, San Francisco, CA, 2011.

## APPENDIX

Gold nanoparticles and polymer solutions were prepared by Dr. Guandong Zhang in Dr. Andre Gobin's laboratory (Bioengineering Department, University of Louisville) as a part of work supported by Kentucky Science and Engineering Foundation grant KSEF-2546-RDE-014, "Light-Powered Hybrid Microactuators for Biotechnology."

### PREPARATION OF GOLD NANOPARTICLES IN LARGE SCALE

**Solution A:** Gold NPs with absorption around 800 - 830 nm were obtained by mixing of 60 ml 3 mM sodium thiosulfate ( $\text{Na}_2\text{S}_2\text{O}_3 \cdot 5\text{H}_2\text{O}$ , Aldrich, 99.999%) solution with 150 ml 1.71 mM chloroauric acid ( $\text{HAuCl}_4 \cdot 3\text{H}_2\text{O}$ , Alfa Aesar, Au 49.68%) solution at room temperature, and vortexed for 20 seconds for uniform mixing. After ageing for six hours, the particles were concentrated by a centrifugation at  $1000\times g$  for 20 minutes the pellets were carefully collected. This concentration process was repeated three times which generates a pellet with extremely high concentration (in the range 300 - 400 OD) that can be diluted to the desired OD. Water used in the solutions was purified by a Thermo Scientific Easypure II system and has resistivity of 18.2 M $\Omega$  cm.

### POLYMER SELECTION AND MODIFICATION

Polymer-nanoparticle composites may possess the unique property superior to that of either the polymer or nanoparticles. Metal nanoparticles with polymer coatings or

dispersed in polymeric matrices display the increased stability, improved processability, recyclability and solubility in a variety of solvents. Several polymer materials were selected and tested for applying in hybrid-nanoparticle MEMS devices, including biocompatible polymers chitosan (CS) and O-carboxymethyl chitosan (CMCS), Polyvinylpyrrolidone (PVP), and other polymers like Poly(methyl methacrylate) (PMMA) and Nylon-6.

## **CONDITIONS FOR NANOPARTICLES/POLYMER FILM**

### **PREPARATION**

Gold/polymer solutions with desired GNP concentration were prepared by dispersing the GNP pellet into pre-made polymer solution. Concentration of the gold NP (in optical unit, OD) is determined by the following equation:

$$C_1 \times V_1 = C_2 \times V_2 \quad (a)$$

where  $C_1$  is the concentration of the GNP pellet,  $V_1$  is the volume of the pellet,  $C_2$  is the concentration of the gold NP in the final polymer solution;  $V_2$  is the volume of the final polymer solution.

The concentration of the polymer component in the final solution (in weight percentage) was determined by the following equation:

$$C_{polymer} = W/V_2 \quad (b)$$

where  $C_{polymer}$  is the concentration of the polymer component in weight,  $V_2$  is the volume of the final polymer solution.

**Solution B and Solution E:** In case of commercial available polymers such as PVP, Nylon-6 and PMMA, the polymer solution was directly diluted to the desired concentration by using the compatible solvent. 3% and 8% Polyvinylpyrrolidone polymer solutions were prepared by dissolving PVP40 powder (average mol. wt. 40,000) in DI water. Gold nanoparticle suspension was added to PVP polymer matrix, using Equation (a)-(b), and then sonicated for 20 minutes to achieve a homogeneous dispersal.

### **PREPARATION OF CARBOXYMETHYLATED CHITOSAN**

O-carboxymethyl chitosan (CMCS) was synthesized using low molecule weight chitosan (Sigma-Aldrich, MW 50-190K). First, 15 grams of sodium hydroxide (NaOH) was dissolved in a 20:80 mixture of DI water and 100 mL of isopropanol in a 500 mL flask. Then 10 grams of chitosan was added to swell and alkalize at 50°C for one hour. Finally, 15 grams of monochloroacetic acid ( $\text{ClCH}_2\text{CO}_2\text{H}$ , 99%, Acros Organics) was dissolved in 20 mL of isopropanol, and added into the reaction mixture by dropping in 30 min and reacted under vigorous agitation for four hours at 55-60°C. To stop the reaction 200 mL of 80% ethyl alcohol was added, followed by filtration and repeated rinsing by 80% ethyl alcohol, to desalt and dewater, until the pH value of the washing solution was less than 8.0. As a final point, the product was vacuum dried for one day at 40°C.

**Solution D and Solution F:** Base solution of chitosan was prepared by dispersing 1 gram of chitosan in 100 mL of 0.7% acetic acid solution. CMCS solution was prepared by directly dissolving 1 gram of CMCS in 100 mL of DI water. CS and CMCS solutions were purified by centrifuge at 1000 RPM for 10 minutes, to remove the little amount of

insoluble residuals, and then put for two days of dialyze (Spectrum Dialysis Membranes, MWCO 3 KDa). Then gold nanoparticles were introduced in prepared chitosan based polymer matrix at desired concentration and sonicated for 20 minutes for uniform dispersion. Table 5 shows detail conditions of the polymer solution prepared and tested for the study.



<b>No.</b>	<b>Polymer and solvent</b>	<b>Polymer Concentration (wt.%)</b>	<b>Au NP Concentration (OD)</b>	<b>Note</b>
1	PVP 40k, IPA	2	50	Bare Au
2	PVP 40k, IPA	2	50	Bare Au
3	PVP 40k, water	3	100	Bare Au
4	PVP 40k, water	3	75	Bare Au
5	PVP 40k, water	3	50	Bare Au
6	PVP 40k, water	3	25	Bare Au
7	PVP 40k, water	3	25	Bare Au
8	PVP 40k, IPA	3	25	Bare Au
9	PVP 10k, water	8	50	Bare Au
10	PVP 40k, water	8	100	Bare Au
11	PVP 40k, water	8	100	Bare Au
12	PVP 40k, water	8	100	Bare Au
13	PVP 40k, water	8	50	Bare Au
14	PVP 40k, water	8	50	Bare Au
15	PVP 40k, water	8	50	Bare Au
16	PVP 40k, water	8	100	Bare Au
17	PVP 40k, IPA	8	100	Bare Au
18	PVP 40k, water	8	150	Bare Au
19	PVP 40k, water	12	100	Bare Au
20	CS, water, (dialyzed 10 day)	1.2	100	Bare Au
21	CS, water, (dialyzed 1 day)	1.5	100	Bare Au
22	CS, water	0.8-0.9	100	Bare Au

23	CS, water	0.8-0.9	100	Bare Au
24	CS, water	0.8	100	Bare Au
25	CS, water	0.8	75	Bare Au
26	CS, water	0.8	50	Bare Au
28	CS, water	0.8	25	Bare Au
29	CS, water	0.8-0.9	100	Dialyzed Au
30	CS, water	0.8-0.9	100	Dialyzed Au
31	CMCS, water	1	50	Bare Au
32	CMSC, water	1	25	Bare Au
33	Nylon-6, formic acid	8	100	Bare Au
34	Nylon-6, formic acid	8	100	Au/CS
35	PMMA, PR950, anisole	4	25	Au modified by Hexadecanethiol
36	PMMA, PR950, acetone	1	25	Bare Au
37	PMMA, PR950, acetone	3	18	Bare Au
38	PMMA, PR950, acetone	1	33	Bare Au

Table 5. Conditions of the polymer solution prepared and tested for the study.

## CURRICULUM VITAE

NAME: Evgeniya V. Moiseeva

ADDRESS: Electrical and Computer Engineering  
Shumaker Research Building,  
2210 South Brook Street  
University of Louisville  
Louisville, KY 40292

DOB: Perm, Russia – November 23, 1980

### EDUCATION

& TRAINING: B.S., Physics  
Perm State University, Perm, Russia  
1997-2001

M.S., Physics  
Perm State University, Perm, Russia  
2001-2003

M.S., Physics  
University of Louisville, Louisville, KY  
2004-2006

### PUBLICATIONS:

1. E. V. Moiseeva, A. A. Fletcher, C. K. Harnett, Thin-film electrode based droplet detection for microfluidic systems, *Sensors & Actuators: B. Chemical*. 155 (2011) 408–414

2. B. A. Goessling, T. M. Lucas, E. V. Moiseeva, J. W. Aebersold, and C. K. Harnett, Bistable Out-of-Plane Stress Mismatched Thermally Actuated Bilayer Devices with Large Deflection, *J. Micromech. Microeng.* 21 (2011) 065030 (7pp)
3. T. Liu, E. V. Moiseeva, and C. K. Harnett, Chips and Tips: Integrated reservoirs for PDMS microfluidic chips, *Lab on a Chip: Chips and Tips*, (2008)
4. E. Moiseeva, Y. M. Senousy, S. McNamara, and C. K. Harnett, Single-mask microfabrication of three-dimensional objects from strained bimorphs, *J. Micromech. Microeng.* 17 (2007) N63–N6

#### NATIONAL MEETING PRESENTATIONS

1. E. Moiseeva, T. Lucas, G. Zhang, A. Gobin, and C. Harnett, Development of MEMS Bistable Actuator Incorporated with Nanoparticles, 17th Annual KY EPSCoR Statewide Conference, Lexington, KY, (2012) May 17
2. E. Moiseeva, T. Lucas, G. Zhang, A. Gobin, and C. Harnett, Light-powered nanoparticle – MEMS hybrid, American Physical Society Meeting (APS), Boston, MA, (2012) February 27- March 2
3. E. Moiseeva, T. Lucas, and C. Harnett, Light-powered nanoparticle-MEMS hybrid, 16th Annual KY EPSCoR Statewide Conference and 7th KY Innovation and Entrepreneurship (KIEC), Louisville, KY, (2011) May 26
4. E. Moiseeva, A. Fletcher, and C. Harnett, Electrode-based detection technique for microfluidic devices, 15th Annual KY EPSCoR Statewide Conference, Lexington, KY, (2010) May 24
5. C. K. Harnett, T. M. Lucas, E. V. Moiseeva, B. Casper, and L. Wilson, Microscopic containers for sample archiving in environmental and biomedical sensors, IEEE International Instrumentation and Measurement Technology Conference (I2MTC), Austin, TX, (2010) May 3-5

6. E. V. Moiseeva, A. A. Fletcher, and C. K. Harnett, Electrode-based detection technique for microfluidic devices, American Physical Society Meeting (APS), Portland, OR, (2010) March 15-19
7. J. W. Aebersold, B. Goessling, E.V. Moiseeva, and C. K.Harnett, Bi-stable thermal actuators, American Physical Society Meeting (APS), Portland, OR, (2010), March 15-19
8. E. V. Moiseeva, and C. K. Harnett, Shear-Based Droplet Production for Biomaterial Printing, NIP25/Digital Fabrication, Louisville, KY, (2009) September 21-25
9. E. V. Moiseeva, and C. K. Harnett, High-temperature microreactors for in-situ nanomaterial deposition, University Government Industry Micro/Nano Symposium (UGIM), Louisville, KY, (2008) July 13-16
10. E.V. Moiseeva, Y. M. Senousy, and C. K. Harnett, Strain-based self-assembly of nanostructures for non-destructive large-scale integration, American Physical Society Meeting (APS), Denver, CO, (2007) March 2-5
11. E. Moiseeva, K. Shay, G. Sumanasekera, "Synthesis of hollow carbon nanotubes and filled carbon nanotubes using CVD Technique", American Physics Society Meeting (APS), Baltimore, MD, (2006) March 13-17